DE-FG02-97ER41022

FLORIDA STATE UNIVERSITY

HIGH ENERGY PHYSICS LABORATORY, Tallahassee, Florida 32306-4350

Search for First Generation Scalar Leptoquarks in Proton-Antiproton Collisions at a Center of Mass Energy of 1.8 TeV with the DØ Detector

by
Guoliang Wang

A dissertation submitted to the Department of Physics in partial fulfillment of the requirements for the degree of Doctor of Philosophy

November 1997

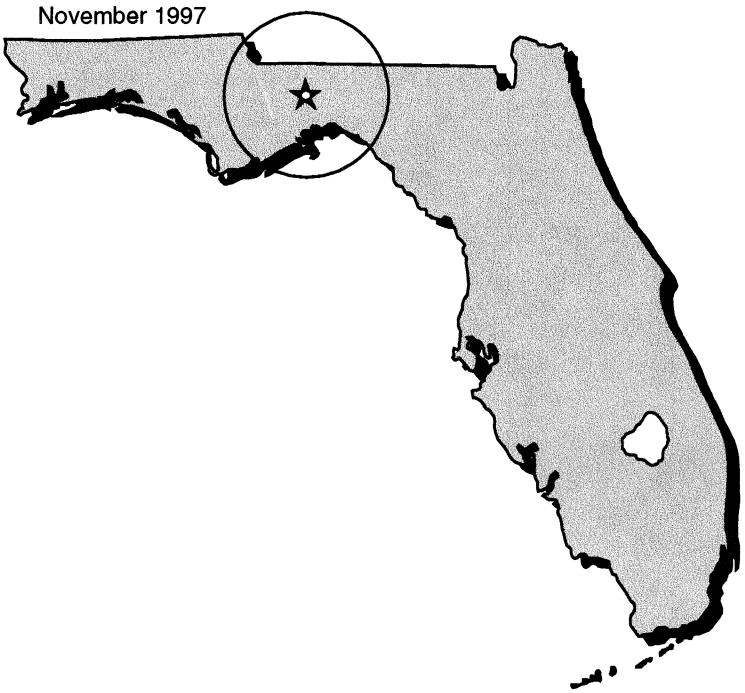

SEARCH FOR FIRST GENERATION SCALAR LEPTOQUARKS IN PROTON-ANTIPROTON COLLISIONS AT A CENTER OF MASS ENERGY OF 1.8 TEV WITH THE DØ DETECTOR

Name: GUOLIANG WANG

Department: Department of Physics

Major Professors: Sharon Hagopian, Susan Blessing

Degree: Doctor of Philosophy

Term Degree Awarded: Fall, 1997

This dissertation describes the searches for first generation scalar leptoquarks in the $eejj$ and $e\nu jj$ channels in $p\bar{p}$ collisions at a center of mass energy of 1.8 TeV using the DØ detector at the Fermi National Accelerator Laboratory. Data corresponding to an integrated luminosity of about 100 pb^{-1} were studied. The number of candidate events in both channels is consistent with the expected yield from Standard Model processes. First generation scalar leptoquarks with mass less than 204 (168) GeV/c^2 are excluded for the branching fraction of leptoquarks decaying into electron and quark $\beta = 1.0$ (0.5) at the 95% confidence level.

SEARCH FOR FIRST GENERATION SCALAR LEPTOQUARKS IN PROTON-ANTIPROTON COLLISIONS AT A CENTER OF MASS ENERGY OF 1.8 TEV WITH THE DØ DETECTOR

Guoliang Wang, Ph.D.
Florida State University, 1997
Major Professors: Sharon Hagopian, Ph.D. and Susan Blessing, Ph.D.

This dissertation describes the searches for first generation scalar leptoquarks in the $eejj$ and $e\nu jj$ channels in $p\bar{p}$ collisions at a center of mass energy of 1.8 TeV using the DØ detector at the Fermi National Accelerator Laboratory. Data corresponding to an integrated luminosity of about 100 pb^{-1} were studied. The number of candidate events in both channels is consistent with the expected yield from Standard Model processes. First generation scalar leptoquarks with mass less than 204 (168) GeV/c^2 are excluded for the branching fraction of leptoquarks decaying into electron and quark $\beta = 1.0$ (0.5) at the 95% confidence level.

THE FLORIDA STATE UNIVERSITY
COLLEGE OF ARTS AND SCIENCES

SEARCH FOR FIRST GENERATION SCALAR LEPTOQUARKS IN PROTON-ANTIPROTON COLLISIONS AT A CENTER OF MASS ENERGY OF 1.8 TEV WITH THE DØ DETECTOR

By

GUOLIANG WANG

A dissertation submitted to the
Department of Physics
in partial fulfillment of the
requirements for the degree of
Doctor of Philosophy

Degree Awarded:
Fall Semester, 1997

The members of the Committee approve the dissertation of Guoliang Wang defended on Nov. 3, 1997.

Sharon Hagopian
Professor Co-Directing dissertation

Susan Blessing
Professor Co-Directing dissertation

Ted Baker
Outside Committee Member

Howard A. Baer
Committee Member

Mark Riley
Committee Member

I dedicate this dissertation

to my parents, Dingguo Wang and Weiyu Chen, who encouraged my pursuit of my Ph.D.;

to my wife, Dan Xiao, and daughter, Jing Wang, who saw me through it.

I love you all.

ACKNOWLEDGEMENTS

First of all, I want to thank my advisors, Sharon Hagopian and Susan Blessing who, over these many years, have taught me much more than just physics. Without Sharon's tireless guidance, this work could not have been finished. Many thanks are also due to the entire High Energy Physics Group at Florida State University. Their support has been invaluable to me. I want to thank Vasken Hagopian and Howard Baer, who introduced me to New Phenomena physics. I want to thank Horst Wahl and Jeff Owens, who taught me High Energy Physics. Also, I would like to thank Terry Heuring and Horst Wahl for their help and encourage. I would like to thank Lupe Howell. Without her help processing the Monte Carlo events, this research could not have finished so quickly. I also want to thank Harrison Prosper for his comments and discussions. I am grateful to Kathy Mork and Sherry Beasley for handling all of the administrative stuff for us far away graduate students.

It is a great pleasure and wonderful experience to work with the DØ collaboration. At DØ, I met numerous excellent physicists and friends. Many thanks are due to Terry Heuring, Robert Madden, Ssumin Chang, Marc Paterno, John Hobbs, Jim Cochran, Doug Norman, Amber Boehnlein, Adam Lyon, Pushpa Bhat, Bob Hirosky, Mark Goforth, Christopher Shaffer, Haowei Xu, and Erich Varnes. Their invaluable help made it much easier for me to become familiar with DØ and start with my research. I must also thank Jan Guida, who taught me much about the DØ detecter when I took shifts. Also I learned from her what hard-working means!

I would like to thank Paul Grannis, Hugh Montgomery, Harry Weerts, Dave Cutts, Wyatt Merritt, John Hobbs, and Sarah Eno for their inspiring leadership and for their support. I would like to thank my editorial board members: Jan Hoftun, Wyatt Merritt, Vladimir Sirotenko, Sharon Hagopian, and Susan Blessing for their comments and suggestions.

I am especially grateful to Sharon Hagopian, Susan Blessing, Howard Baer, Mark Riley and Ted Baker for serving on my dissertation committee.

I would like to thank my fellow graduate students at FSU: Bob Madden, Chris Shaffer, Feng Wen, Dan Karmgard and Jeff McDonald who made sure the FSU office was never boring.

Finally, I would like to thank my wife, Dan Xiao, for her love and support. Her encouragement and understanding, and my daughter Jing's loveliness have always been my source of joy. I can never thank them enough.

CONTENTS

LIST OF TABLES xi

LIST OF FIGURES xiv

1 Introduction 1

1.1 The Standard Model 2

1.2 Beyond the Standard Model 8

1.2.1 Supersymmetry (SUSY) 9

1.2.2 Grand Unified Theories (GUT) 9

1.3 Summary 10

2 Phenomenology of Leptoquarks 11

2.1 Leptoquark Couplings 13

2.2 Pair Production at Hadron Colliders (Leading Order) 15

2.2.1 gg Fusion Production 15

2.2.2 $q\bar{q}$ Annihilation 15

2.2.3 Total Cross Section 16

2.3 Next-to-Leading Order Calculations 21

2.4 Signatures for this Search 21

2.5 Existing Limits 23

3 The Apparatus 26

3.1 The Tevatron 26

3.2 The DØ Detector 28

3.2.1 Central Detectors 30
3.2.2 Calorimeters 36
3.2.3 Muon Detector 41
3.3 Trigger and Data Acquisition System 44
3.3.1 Level 0 Trigger 44
3.3.2 Level 1 and 1.5 Trigger 44
3.3.3 Data Acquisition and Level 2 Trigger 47

4 Event Reconstruction and Particle Identification 49
4.1 Vertex Determination 49
4.1.1 Beam x-y Position 49
4.1.2 Interaction z Position 50
4.2 Electron Reconstruction and Identification 50
4.2.1 Electromagnetic Energy Fraction 52
4.2.2 Cluster Isolation 52
4.2.3 Covariance Matrix X^2 53
4.2.4 Cluster Track Match 54
4.2.5 Track Ionization 54
4.2.6 Electron Likelihood Identification 55
4.3 Jet Reconstruction 56
4.4 Missing E_T ($\not\!\!E_T$) Measurement 58
4.5 Energy Scale Correction 58

5 Analysis 63
5.1 $eejj$ Channel 63
5.1.1 Signal Simulation 64
5.1.2 Backgrounds 64

5.1.3 Distributions of Physics Variables for MC Signal and MC Backgrounds . . . 68
5.1.4 Offline Events Selection Criteria . . . 69
5.1.5 Data Selection . . . 74
5.1.6 Background Estimation . . . 81
5.1.7 Signal Efficiency . . . 92
5.1.8 Signal Cross Section Upper Limit Calculation . . . 99
5.1.9 Outline of Signal Cross Section Upper Limit Calculation . . . 101
5.1.10 Results . . . 103
5.2 $e\nu jj$ Channel . . . 105
5.2.1 Signal Simulation . . . 105
5.2.2 Backgrounds . . . 105
5.2.3 Distributions of Physics Variables for MC Signal and MC Backgrounds . . . 107
5.2.4 Offline Events Selection Criterion . . . 108
5.2.5 Data Selection . . . 108
5.2.6 Background Estimation . . . 125
5.2.7 Signal Efficiency . . . 128
5.2.8 Results . . . 130
5.3 The Combined Result from the $eejj$ and $e\nu jj$ Channels . . . 132
5.3.1 The 95% Cross Section Upper Limit Calculation . . . 132
5.3.2 Results . . . 134
5.4 Summary . . . 135

6 Conclusions **140**

BIBLIOGRAPHY **142**

BIOGRAPHICAL SKETCH 147

LIST OF TABLES

1.1 Quarks and leptons of the SM. 3

1.2 The Fundamental Forces. 5

4.1 Jet Resolution 57

5.1 The status of the leptoquark pair production MC events. 65

5.2 Summary of the physics backgrounds MC events. 66

5.3 s/b and $s/\mathrm{sqrt(b)}$ for different offline selections. 75

5.4 Selection of the Z boson mass window cuts. 77

5.5 Triggers used in the $eejj$ channel. 78

5.6 The number of events passing the offline cuts in $eejj$ channel 81

5.7 Detailed information on candidates in the $eejj$ channel before the δM cut. 82

5.8 The number of events of Run I data and backgrounds inside and outside the Z boson mass range 76 – 106 GeV/c^2 with looser cuts. . . 85

5.9 The number of events from Run I data and expected backgrounds inside and outside the Z boson mass range 76–106 GeV/c^2 with the offline cuts. 86

5.10 The probability for jets to be misidentified as electrons. 90

5.11 The total backgrounds resulting from the $eejj$ LQ search. 91

5.12 Efficiencies of the electron ID cuts. 97

5.13 Two-electron ID cut efficiencies. 97

5.14 Offline cuts acceptance for the leptoquark MC events at different mass points in $eejj$ channel. 99

5.15 The signal efficiency from the $eejj$ LQ search. 100
5.16 The status of the leptoquark pair production MC events in $e\nu jj$ channel. 106
5.17 The status of the physics backgrounds MC events in $e\nu jj$ channel. . . 107
5.18 Detailed information for the remaining candidate event. 120
5.19 The number of data and expected background events after each cuts. 125
5.20 Normalization of $W + 2$ jets MC events to collider data. 126
5.21 Summary of the yields of backgrounds for integrated luminosity of 103.7 pb^{-1} and the observed number of events. 128
5.22 Total background resulting from the $e\nu jj$ LQ search. 129
5.23 The signal acceptance and total efficiency from the $e\nu jj$ LQ search. . 131

LIST OF FIGURES

2.1 Feynman diagrams for leptoquark pair production via gluon-gluon fusion 16

2.2 Feynman diagrams for leptoquark pair production via $q\bar{q}$ scattering . 18

2.3 The different contributions for scalar leptoquark pair production . . . 19

2.4 Integrated cross sections for scalar leptoquark pair production 20

2.5 The gluon–quark sub-processes. 22

2.6 The LO and NLO calculation for different renormalization scales. . . 24

3.1 The schematic view of the Tevatron. 27

3.2 A cutaway view of the DØ detector. 29

3.3 A schematic picture of the central detector. 30

3.4 The VTX chambers. 31

3.5 Cross sectional view of the TRD. 32

3.6 The CDC chambers. 34

3.7 The FDC package. 35

3.8 The layout of the calorimeter. 37

3.9 The side views of one quarter of the full calorimeter and the central detectors. 38

3.10 The elevation view of the DØ detector. 42

3.11 The interaction length of the detector. 43

3.12 The DØ data acquisition system. 45

4.1 The comparison of four-variables likelihood distribution for electron and non-electron objects. 56

4.2 The cumulative energy correction for jets. 62

5.1 The invariant mass distribution for the Drell-Yan MC sample. 67

5.2 The E_T distribution of the leading two electrons and leading two jets of the MC signal and major background events. 70

5.3 The one electron and one jet invariant mass distribution of the MC signal and major background events. 71

5.4 The invariant mass distribution of the dielectron from the MC signal and major background events. 72

5.5 The Distributions of δM for signal and background for four different LQ masses. 76

5.6 The characteristics of the Run Ib data. 80

5.7 Invariant mass distribution for electron pairs requiring two electrons with $E_T > 25$ GeV and two jets with $E_T > 15$ GeV. 83

5.8 Invariant mass distribution for electron pairs requiring two electrons with $E_T > 25$ GeV and two jets with $E_T > 30$ GeV. 83

5.9 The DØ measured Z boson p_T distribution. 87

5.10 Invariant mass distribution for electron pairs with unbiased electron in the CC. 95

5.11 Invariant mass distribution for electron pairs with unbiased electron in the EC. 95

5.12 The 95% CL cross section upper limits for $\beta = 1.0$. 104

5.13 Kinematic distributions for the MC signal and background events. . . 109

5.14 The invariant mass distribution (of an electron and one jet) and transverse mass distribution (of missing E_T and one jet). 110

5.15 M_{ej1} vs. $M_T(\not{E}_T j2)$. 112

5.16 $M_{e,j2}$ vs. $M_T(\not{E}_T j1)$. 113

5.17 The number of jets with $E_T > 25$ GeV and $|\eta| < 2.5$. 115

5.18 The H_T distribution. 116
5.19 The electron and neutrino transverse mass distribution for the collider data and total background events after the basic offline cuts have been applied. 119
5.20 The electron and neutrino transverse mass distribution for the collider data and total background events after the offline cuts (except transverse mass and LQ mass window cuts) have been applied. 119
5.21 The transverse mass distribution of the electron and neutrino. 121
5.22 Distributions for δM for signal and background for four different LQ masses. 123
5.23 Signficance distributions for the four masses shown above. 124
5.24 The 95% CL cross section upper limit from the $e\nu jj$ channel. 133
5.25 The 95% CL cross section limits from the combination. 137
5.26 The 95% CL cross section limits from the combination. 138
5.27 Excluded contour of scalar leptoquark branching fraction β vs. mass from the combination. 139

ABSTRACT

This dissertation describes the searches for first generation scalar leptoquarks in the $eejj$ and $e\nu jj$ channels in $p\bar{p}$ collisions at a center of mass energy of 1.8 TeV using the DØ detector at the Fermi National Accelerator Laboratory. Data corresponding to an integrated luminosity of about 100 pb^{-1} were studied. The number of candidate events in both channels is consistent with the expected yield from Standard Model processes. First generation scalar leptoquarks with mass less than 204 (168) GeV/c^2 are excluded for the branching fraction of leptoquarks decaying into electron and quark $\beta = 1.0$ (0.5) at the 95% confidence level.

CHAPTER 1

INTRODUCTION

One of the characteristics of human nature is that we attempt to understand the world around us. One way to understand nature is to understand the elementary constituents of the universe and the laws which govern their interactions.

The earlier answers to the question "what is the world made of?" included the solution provided by Anaximenes of Miletus: all forms of matter are obtained by the condensing of air. Later, people learned from chemistry that the world is made of molecules and the molecule is made of atoms. In the early 1900's, Rutherford proposed as an explanation of his famous scattering experiment that an atom is made of a nucleus and electrons surrounding the nucleus. With the discovery of protons and neutrons, people learned that the nucleus is made up of neutrons and protons. In the last 20 years we have learned that neutrons and protons are not elementary particles, but are made up of *quarks*. Electrons are considered to belong to the family of *leptons*. Quarks and leptons are spin-$\frac{1}{2}$ particles and are considered to be fundamental.

How do the building blocks make up the universe we live in and ourselves? The answer is that besides the elementary constituents (today's elementary constituents may not be the basic building blocks of matter), there are four kinds of forces: gravitational, weak, electromagnetic and strong forces. The gravitational force is important for the celestial mass and distance, such as apples dropping to the earth. For tiny objects like quarks and leptons, the gravitational force is so small that we can ignore its existence. The electromagnetic force is an infinite range force and exists between any charged objects. It attracts electrons to atomic nuclei to

form atoms. The strong interaction is a strong, short range force that exists between colored particles like quarks and gluons and binds quarks into protons and neutrons. The weak interaction is a weaker, very short range force that exists between any leptons such as electrons and neutrinos and also quarks. The weak interaction is responsible for the radioactive β–decay of nuclei.

High energy physics is so called because high energies are needed to probe these interactions and to localize and create fundamental particles. A common method to understand the properties of the elementary particles and the forces between them is to accelerate particles (such as protons and electrons) to very high energy and let them collide. The resulting particles are detected after the collision. The purpose of measuring the final particles is to see if there are any new particles or any unusual physical processes occurring.

The Tevatron is a superconducting accelerator at Fermilab. The DØ detector is one of two large general-purpose detectors at the Tevatron. The subject of this dissertation is the search for one such new particle, namely first generation scalar leptoquark, using the DØ detector.

1.1 The Standard Model

To understand nature, physicists have developed a model to explain the building blocks and the forces between them. This model, called the Standard Model (SM) is a widely accepted model and the most successful economical model so far to describe our physical world.

In the framework of the SM [1], the world is made of the elementary, structureless, point-like particles which have spin-$\frac{1}{2}$ and thus obey Fermi-Dirac statistics. They are called fermions. The fermions are further divided into quarks and leptons. As listed in Table 1.1, there are six quarks: up (u), down (d), charm (c), strange (s), top (t), and bottom (b); and six leptons: electron (e), electron neutrino (ν_e), muon (μ),

Table 1.1: Quarks and leptons of the SM.

Fermion	Quarks		Leptons	
Charges	$\frac{2}{3}$	$-\frac{1}{3}$	0	-1
1st Gen.	u	d	ν_e	e
2nd Gen.	c	s	ν_μ	μ
3rd Gen.	t	b	ν_τ	τ

muon neutrino (ν_μ), tau (τ) and tau neutrino (ν_τ). Quarks have fractional charge: $+\frac{2}{3}e$ or $-\frac{1}{3}e$ where $-e$ is the charge of the electron. Leptons have integral charges: $-e$ or 0. The fermions interact with each other by exchange of fundamental bosons (field quanta): *photons* (γ), *gluons (g)*, $W^{\pm}$ bosons, and Z^0 bosons. Bosons have integral spin and obey Bose–Einstein statistics and are listed in Table 1.2.

The charged leptons have electromagnetic and weak interactions, while the neutrinos are distinguished by having only weak interactions with other particles. Quarks, in addition to weak and electromagnetic interactions, are subject to strong interactions.

Mathematically, the SM is a gauge field theory based on the group $SU(3)_c \times SU(2)_L \times U(1)_Y$, where c refers to color, L refers to weak isospin and Y is weak hypercharge.

The $U(1)$ symmetry corresponds to Quantum Electrodynamics (QED), which was proposed by P. A. M. Dirac in 1928. In QED, the free electron is described by four-component wavefunctions, each corresponding to two spin substates, $J_z = \pm\frac{1}{2}\hbar$, with positive and negative energy. The negative energy states are interpreted as antiparticles, the positrons. Every elementary particle in the SM has a corresponding antiparticle, which has the opposite charge. One very important property of QED is *renormalizability*. Because a single electron can emit and reabsorb virtual photons,

the theoretical calculations of electron "bare" mass m_0 or charge e_0 become infinite. Divergent terms of this type are present in all QED calculations. However, it is possible to absorb all the divergences into m_0 or e_0, and then redefine the mass and charge, replacing them by their physical values m, e. This process is called renormalization. The result is that QED calculations, if expressed in terms of the physical quantities e and m, always give finite values for cross-sections, decay rates, and so forth. The generator of the $U(1)$ group is the weak hypercharge Y.

The generators of the $SU(2)$ group are the three components of the weak isospin (I). In the fundamental representation, the three generators are denoted as Pauli matrices $I_i \equiv \frac{1}{2}\sigma_i$ where

$$\sigma_1 = \begin{pmatrix} 0 & 1 \\ 1 & 0 \end{pmatrix} ; \ \sigma_2 = \begin{pmatrix} 0 & -i \\ i & 0 \end{pmatrix} ; \ \sigma_3 = \begin{pmatrix} 1 & 0 \\ 0 & -1 \end{pmatrix} . \tag{1.1}$$

Although the weak and electromagnetic forces appear to be quite different at a low energy scale, i.e. $q^2 \ll M_W^2$, where q is momentum transfer and M_W is about 100 GeV/c^2, they are unified with the same intrinsic coupling strength at a higher energy scale, i.e. $q^2 \sim M_W^2$, based on the Weinberg-Salam $SU(2) \times U(1)$ model – the electroweak interactions model. The fundamental vector bosons are massless isovector triplets $\mathbf{W}_\mu = W_\mu^{(i)}$ (i=1,2,3) for $SU(2)$ and a massless isosinglet B_μ for $U(1)$. The Spontaneous Symmetry Breaking (SSB) mechanism is brought in to give the gauge bosons mass, without spoiling the renormalizability. This is achieved with the help of an isospin doublet of scalar mesons called Higgs scalars, which generate mass as a result of self-interaction. Because of spontaneous symmetry breaking, three bosons (W_μ^+, W_μ^-, and Z_μ^0) acquire mass, and one (A_μ, the photon) remains massless.

The interaction (Lagrangian density $\mathcal{L}$) of fermions with the fields $\mathbf{W}_\mu$ and B_μ is the product of the fermion currents with the fields:

$$\mathcal{L} \ = \ g\mathbf{J}_\mu \cdot \mathbf{W}_\mu + g' J_\mu^Y B_\mu \tag{1.2}$$

Table 1.2: The Fundamental Forces.

Interaction	Relative Strength	Field Quanta	Mass (GeV/c^2)	Range
Strong	~ 1	8 g	0	$\sim 10^{-15}$ m
Electromagnetic	$\sim 1/137$	γ	0	infinite
Weak	$\sim 10^{-5}$	$W^{\pm}$ Z^0	80.22 91.17	$\sim 10^{-18}$ m
Gravitational	$\sim 10^{-38}$	G	0	infinite

where $\mathbf{J}_\mu$ and J_μ^Y represent the isospin and hypercharge currents of the fermions (leptons or quarks) respectively, and g and g' are their couplings to $\mathbf{W}_\mu$ and B_μ. The relationship between e, g and g' is:

$$e = g\sin\theta_W = g'\cos\theta_W \tag{1.3}$$

where θ_W is called the weak mixing angle (or Weinberg angle).

We know that the weak charged-current interaction is parity-violating, and connects, for example, the left-handed states of neutrino and electron. On the other hand, the electromagnetic interaction is parity-conserving and involves both left-handed and right-handed states of the electron. Hence, the lepton states are assigned to a left-handed doublet and a right-handed singlet:

$$\begin{aligned} \psi_L &= \frac{(1+\gamma_5)}{2}\begin{pmatrix} \nu_e \\ e^- \end{pmatrix}; \text{ with } T = \frac{1}{2},\ Y = -1 \\ \psi_R &= \frac{(1-\gamma_5)}{2}(e^-); \text{ with } T = 0,\ Y = -2. \end{aligned} \tag{1.4}$$

For quarks,

$$\psi_L = \frac{(1+\gamma_5)}{2}\begin{pmatrix} u \\ d \end{pmatrix}; \ \psi_R = u_R \text{ or } d_R. \tag{1.5}$$

where T and Y are the generators of the $SU(2)_L$ and $U(1)_Y$ groups of gauge transformations, respectively. In the limit of low energy scale, i.e. $q^2 \ll M_W^2$, the physical boson mass can be written as:

$$\begin{aligned} M_{W^\pm} &= \left(\frac{g^2\sqrt{2}}{8G}\right)^{1/2} \\ &= \left(\frac{e^2\sqrt{2}}{8G\sin^2\theta_W}\right)^{1/2} \\ M_{Z^0} &= \frac{M_W^2}{\rho\cos^2\theta_W} \\ M_\gamma &= 0 \end{aligned} \tag{1.6}$$

where ρ is a factor which is observed to be 1 by all experiments to date, G is Fermi constant and $M_\gamma = 0$ is from the empirical fact.

The strong force and its interaction with quarks may be mathematically represented by a local gauge invariant $SU(3)_c$ color symmetry. Quarks come in three colors: *red*, *green*, and *blue*, denoted symbolically by R, G, and B, respectively. The antiquarks are assigned the complementary colors: cyan ($\overline{R}$), magenta ($\overline{G}$), and yellow ($\overline{B}$). All particles observed in nature are "colorless" or "white" (or, to be more precise, unchanged by rotations in R, G, B space). *Baryons* are bound states of three quarks with different color. *Mesons* are bound states of quark and antiquark with color and complementary color respectively. All physical states of the baryons and mesons are therefore colorless.

The generators of the $SU(3)_c$ group may be taken to be any $3 \times 3 - 1 = 8$ linearly independent traceless hermitian 3×3 matrices. The fundamental representation of $SU(3)_c$ is a triplet. The three color charges of a quark, R, G, and B, form the fundamental representation of the $SU(3)$ symmetry group. In this representation, the generators are traditionally denoted λ_i, i=1,2,...,8, known as the Gell-Mann

matrices and the diagonal matrices are taken to be

$$\lambda_3 = \begin{pmatrix} 1 & & \\ & -1 & \\ & & 0 \end{pmatrix}, \ \lambda_8 = \sqrt{\frac{1}{3}} \begin{pmatrix} 1 & & \\ & 1 & \\ & & -2 \end{pmatrix} \tag{1.7}$$

with simultaneous eigenvectors

$$R = \begin{pmatrix} 1 \\ 0 \\ 0 \end{pmatrix}, \ G = \begin{pmatrix} 0 \\ 1 \\ 0 \end{pmatrix}, \ B = \begin{pmatrix} 0 \\ 0 \\ 1 \end{pmatrix}. \tag{1.8}$$

In the field theory of quark-quark interactions, *quantum chromodynamics* (QCD), the strong color field is mediated by massless vector gluons, which come in eight different color combinations:

$$R\overline{G}, R\overline{B}, G\overline{R}, G\overline{B}, B\overline{R}, B\overline{G}, \sqrt{\frac{1}{2}}(R\overline{R} - G\overline{G}), \sqrt{\frac{1}{6}}(R\overline{R} + G\overline{G} - 2B\overline{B}). \tag{1.9}$$

The remaining combination, the $SU(3)$ color singlet,

$$\sqrt{\frac{1}{3}}(R\overline{R} + G\overline{G} + B\overline{B}) \tag{1.10}$$

does not carry color and cannot mediate interaction between color charges.

For violent collisions of very high q^2 (momentum transferred), the *strong coupling* $\alpha_s < 1$. The theory is thus renormalizable (i.e. calculable) for short-distance interactions. Hence, the theory is called "asymptotically free." At low q^2 (or equivalently, larger distances), the coupling α_s becomes large and the theory is non-perturbative but can do lattice gauge calculations. This large-distance behavior is presumably linked to the confinement of quarks and gluons inside hadrons.

1.2 Beyond the Standard Model

Although the Standard Model of particle physics has been tested in detail and is consistent with all current experimental data within the theoretical and experimental uncertainties, there are several reasons to believe that the Standard Model is an incomplete description of nature. Some of the reasons are (1) apart from the gauge coupling constants, the SM needs on the order of twenty parameters to adjust masses and mixing angles; (2) the SM has an ad hoc choice of the gauge group and particle multiplets; (3) the SM lacks an explanation for the number of quark and lepton generations, an the reason for the "Xerox copies" of quark and lepton flavors; (4) the SM needs scalar particles (Higgs bosons) to induce spontaneous breaking of gauge symmetry and allow Yukawa coupling to the fermions which lead to generation of masses after the breakdown of the gauge symmetry. However, the mass of scalar particles such as the Higgs particle is subject to quadratic divergence in perturbation theory. In lowest order of perturbation theory

$$m_H{}^2 = m_0{}^2 + \delta m_H{}^2 \approx m_0{}^2 - g^2\Lambda^2 \tag{1.11}$$

where m_H is the scalar Higgs boson mass, m_0 is the bare Higgs boson mass parameter, g is a dimensionless coupling constant, and Λ is the energy scale. The mass of the Higgs boson, m_H, is predicted to be comparable to the empirically measured electroweak scale ($\approx$ 250 GeV/c^2). So if $g^2 \approx 1$ and Λ is as large as $M_{\rm GUT}$ (10^{16} GeV/c^2) or $M_{\rm Plank}$ (10^{19} GeV/c^2), m_0^2 must be precisely adjusted so that the two terms in Eq. 1.11, each of which is the order of 10^{30} (GeV/c^2)^2, cancel leaving m_H of $\approx$ 250 GeV/c^2 [3]. While this is not impossible, the requirement of such a precise adjustment of the values of input parameters is unnatural. Today, there are many theories going beyond the SM. A few popular models are introduced in the following.

1.2.1 Supersymmetry (SUSY)

SUSY [3, 4] is a symmetry which relates fermions and bosons. It introduces a supersymmetric partner (*sparticle*) for every particle of the SM, with spin differing by $\frac{1}{2}$ unit but with the same other internal quantum numbers. For the the SM quarks (leptons), there are the corresponding spin 0 superpartner *squarks (sleptons)*. The superpartner of the SM gluons are spin $\frac{1}{2}$ *gluinos*. The superpartners of the SM charged Higgs and weak bosons are charginos and the superpartners of the SM photon, Z^0 and neutral Higgs bosons are neutralinos. The simplest supersymmetric extension of the SM is the *Minimal Supersymmetric Standard Model* (MSSM) which introduces the fewest new particles. In the MSSM, the (mass)^2 of the scalar bosons is no longer quadratically divergent. For each scalar particle loop, there is a fermionic partner loop. The two loops cancel each other in perturbative calculations and lead to a finite result.

The gauge symmetry of the MSSM lagrangian allows the definition of a new multiplicative quantum number R, which is $+1$ for SM particles and -1 for the superpartners. R can be written as:

$$R = (-1)^{3B+L+2S} \tag{1.12}$$

where S is the spin of the particle in units of $\hbar$, and B and L are baryon and lepton numbers respectively. In the MSSM model, R-parity is conserved which implies sparticles are produced in pairs, and that the Lightest Supersymmetric Particle (LSP) must be absolutely stable and have neutral charge. The LSP interacts only weakly or gravitationally.

1.2.2 Grand Unified Theories (GUT)

The so-called *Grand Unified Theories* (GUTs) [2] postulate a single interaction to describe electromagnetic, weak and strong processes with a unique intrinsic coupling at the unification energy ($\approx 10^{15}$ GeV), and appeal to further symmetry-breaking

processes to account for their different apparent strengths in the energy domain well below the unification scale. There are many ways in which the $SU(2)$, $U(1)$ and $SU(3)$ symmetries could be incorporated into a more larger gauge symmetry. The simplest grand unifying symmetry is that of the group $SU(5)$. This incorporates the known fermions (leptons and quarks) in multiplets, inside of which quarks can transform to leptons, and quarks to antiquarks, via the mediation of very massive ($\approx 10^{15}$ GeV/c^2) bosons Y and X, with electric charges $-\frac{1}{3}$ and $-\frac{4}{3}$. In this theory, a gluon mediates the color force between quarks, the $W^{\pm}$ bosons mediate the charged weak current, and an X "leptoquark" boson transforms a quark to a lepton. Quarks have fractional charges ($\frac{1}{3}$ and $\frac{2}{3}$) because the quarks come in three colors, while leptons are colorless. The strong similarity between the weak lepton and quark doublet patterns, for example, $(\nu_e, e)_L$ and $(u, d_c)_L$, and the fact that $Q(\nu) - Q(e) = Q(u) - Q(d)$, occur as natural consequences of GUT unification.

1.3 Summary

This dissertation describes a search for one such new particle, leptoquark, which will be described in detail in Chapter 2.

CHAPTER 2

PHENOMENOLOGY OF LEPTOQUARKS

The observed symmetry in the generation structure of quark and lepton families, which leads to two kinds of fermions (quarks and leptons), is a mysterious occurrence within the SM and suggests that quarks and leptons may be related at a more fundamental level. Almost all models beyond the SM which deal with the connection of leptons and quarks predict the existence of leptoquarks. In all of these models, leptoquarks are particles which carry both baryon and lepton number, couple to both leptons and quarks, and are color triplets under $SU(3)_c$. In models where baryon and lepton numbers are separately conserved, leptoquarks can be light (the order of the electroweak scale) and still avoid conflict with rapid proton decay. Depending on the structure of each specific model, leptoquarks can have spin 0, 1 or 2; fractional electrical charge $-\frac{4}{3}$, $-\frac{1}{3}$, $\frac{2}{3}$ or $\frac{5}{3}$; isospin 0, $\frac{1}{2}$ or 1; baryon number $\pm\frac{1}{3}$; and lepton number ± 1. Several models are described briefly below.

Leptoquarks exist as a bound state of quarks and leptons in the strong-coupling, confining version of the standard $SU(2)_L \times U(1)_Y$ electroweak model [5, 6]. In this model, the conventional $SU(2)_L \times U(1)_Y$ lagrangian with the usual particle content and quantum number assignments is used. Only two additional assumptions are made. One is that the $SU(2)_L$ coupling constant becomes large at a mass Λ which sets the scale for the weak interactions (Λ is roughly of order 250 GeV). The other assumption is that no appreciable scalar vacuum expectation value exists. The particle spectrum, and charged and neutral current weak interactions are matched perfectly with those of the standard, weak-coupling model. However, at energies near or above the weak interaction mass scale, the two models are clearly

distinguishable with the strong-coupling model exhibiting bound states of quarks and leptons.

In GUT models [2], as described in Section 1.2.2, a "leptoquark" is induced to transform a quark into a lepton. As a result, the strong similarity between the weak lepton and quark doublet patterns occurs as a natural consequences of lepton-quark unification.

Leptoquarks can be found in the $SU(4)$ Pati-Salam unification [7] model, where quarks are assumed to carry four "colors": three of these are the conventional "color" quantum numbers, and the fourth represents the lepton number L. The unification of baryonic and leptonic matter arises by extending the gauge symmetry $SU(3)$ of the three colors to $SU(4)$ for the four colors. As the result, leptoquarks are found as exotic gauge mesons carrying both baryonic as well as leptonic quantum numbers, particularly in semileptonic processes. Since leptoquarks in this model give rise to the highly suppressed decays such as $K_L^0 \to \mu e$, $K^+ \to \pi^+ \mu e$, $B_s^0 \to \mu e$, and $B_d^0 \to \mu e$, etc., either their mass must be at least 10 TeV/c^2 which is far beyond the range of energies accessible directly at present accelerators[1], or their couplings must be proportional to quark and lepton masses and hence highly suppressed.

In the technicolor model [9], the problems of the Standard Model (SM) such as the arbitrary choice of the scalar sector, the unknown decay modes of the scalars, the ambiguity of the elementary scalar solution, the lack of experimental information about the number of $SU(2)_L$ weak-isospin doublets, of the electroweak interaction are investigated through the technicolor approach. Leptoquarks are color-triplet technipions with baryon number $\frac{1}{3}$ and lepton number -1, which can decay into quarks and leptons.

[1]The CDF Collaboration at Fermilab has conducted an indirect leptoquark search via $B_s^0 \to \mu e$ and $B_d^0 \to \mu e$, setting preliminary mass limits for Pati-Salam type leptoquarks at 12.1 TeV/c^2 from B_s^0 decays, and 18.3 TeV/c^2 from B_d^0 decays [8].

An alternative type of leptoquark occurs in $SU(5)$ unified theories. If the $SU(5)$ symmetry is a remnant of an E_6 invariance where particles are grouped in 27-dimensional representations suggested by superstring model[10, 11], leptoquarks occur only in 5 and 5^* representations. The standard $SU(5)$ model leptoquarks must be very heavy, $M_{LQ} \sim (10^{10} - 10^{15})$ GeV/c^2, to avoid too-rapid proton decay. This is because the leptoquarks also couple to quark pairs, required by $SU(5)$ invariance. If the leptoquark is relatively light with mass $M_{LQ} \sim \mathcal{O}(M_W)$, which requires that leptoquarks can only couple to quarks and leptons, and that the couplings to quark pairs must be vanished. This leptoquark model violates $SU(5)$ invariance.

Generally, the introduction of leptoquarks leads to additional contributions to proton decay and other rare decays. Leptoquarks which have baryon or lepton number violating couplings must be very heavy to avoid rapid proton decay or large Majorana neutrino masses. However, they can be as light as several hundred GeV/c^2 and still avoid conflicts with rapid proton decay as described above and the non-observation of flavor-changing neutral currents (FCNC's)[10, 12]. Any bounds obtained from FCNC's are generally very model dependent and can be avoided by the assumption of diagonal couplings. Leptoquark couplings are discussed below in detail.

2.1 Leptoquark Couplings

The most general form of the scalar leptoquark-lepton-quark coupling is given by the interaction:

$$\mathcal{L} = \bar{l}^i(\lambda_1^{ij} + \lambda_2^{ij}\gamma_5)q^j S + H.C. \tag{2.1}$$

where i, j are generation indices and $|\lambda_1^{ij}|^2 + |\lambda_2^{ij}|^2 = (\lambda^{ij})^2$, the strength of the leptoquark coupling. l and q are the lepton and quark doublets respectively. $H.C.$

is the hermetion conjugate of the first part. The coupling can be scaled to the electromagnetic coupling α_{em} via

$$(\lambda^{ij})^2/4\pi = k\alpha_{em} \tag{2.2}$$

where k is a scaling number.

The effects of k on the process $e^+e^- \rightarrow q\bar{q}$ is discussed in Ref. [13]. The existence of leptoquarks will lead to an s-channel contribution to the process in addition to the usual γ and Z boson exchanged. By demanding that neither the $q\bar{q}$ production cross section nor the forward-backward asymmetry deviate by more than 10% from their SM predictions, the authors of Ref. [13] have placed a limit on the value of M_{LQ} as a function of k. Leptoquarks with mass less than 150 GeV/c^2 can be ruled out if $k = 0.5$ is assumed. For $k = 5$, leptoquarks are ruled out for M_{LQ} less than 450 GeV/c^2.

A leptoquark with universal couplings to all flavors will give rise to FCNC and will be severely constrained. Limits on rare meson decays such as $\pi^\pm \rightarrow e\nu$, $D^0 \rightarrow \mu^+\mu^-$ and $K^\pm \rightarrow e\nu$ are consistent with a relatively light leptoquark if we assume the couplings must be chiral: a given leptoquark can have either left- or right-handed couplings, i.e., $\lambda_1 = -\lambda_2$ or $\lambda_1 = +\lambda_2$. In addition, leptoquarks must satisfy the following conditions: (i) there are three distinct generations of leptoquark LQ_i ($i = 1$, 2 or 3) and (ii) each LQ_i couples only to the corresponding generation of quarks and leptons. Under these conditions, experimental constraints can be satisfied without requiring large M_{LQ} suppression, thereby making leptoquarks accessible at current energies.

This search only considers the class of leptoquarks which have dimensionless fermionic coupling and baryon and lepton number conservation. Also, leptoquarks must be family-diagonal and $SU(3)_c \times SU(2)_L \times U(1)_Y$ invariant. Since the lightest leptoquark is usually spin 0, only spin = 0 and electric charge Q = $-\frac{1}{3}$ or $+\frac{2}{3}$

leptoquarks will be studied. These scalar leptoquarks are denoted by either LQ or S below.

2.2 Pair Production at Hadron Colliders (Leading Order)

At hadron colliders, $LQ\overline{LQ}$ pairs can be produced through $\mathcal{O}(\alpha_s^2)$ processes via gluon-gluon fusion or $q\bar{q}$ annihilation [14, 15, 16].

2.2.1 gg Fusion Production

The Feynman diagrams for $LQ\overline{LQ}$ pair production via gluon-gluon fusion at hadron colliders are shown in Fig. 2.1.

The cross section is

$$\sigma_1(gg \to LQ\overline{LQ}) = \frac{\pi\alpha_s^2}{6\hat{s}}\left[\left(\frac{5}{8}+\frac{31}{4}\frac{m^2}{\hat{s}}\right)\xi + \left(4+\frac{m^2}{\hat{s}}\right)\frac{m^2}{\hat{s}}\ln\left(\frac{1-\xi}{1+\xi}\right)\right] \tag{2.3}$$

where α_s is the strong coupling constant, $\xi = \sqrt{1-\frac{4m^2}{\hat{s}}}$, m is the leptoquark mass, and $\sqrt{\hat{s}}$ is the cms energy of the subprocess.

2.2.2 $q\bar{q}$ Annihilation

The Feynman diagrams for $LQ\overline{LQ}$ pair production via $q\bar{q}$ scattering at hadron colliders are shown in Fig. 2.2.

The cross section due to the diagram of Fig. 2.2(a) is

$$\sigma_2(q\bar{q} \to LQ\overline{LQ}) = \frac{2\pi\alpha_s^2}{27\hat{s}} \tag{2.4}$$

The cross section through diagram Fig. 2.2(b) is

$$\sigma_3(q\bar{q} \to LQ\overline{LQ}) = \frac{2\pi\lambda_{LQ}^2}{9\hat{s}}\left[\left(1-\frac{2m^2}{\hat{s}}\right)\ln\frac{\hat{s}(1+\xi)-2m^2}{\hat{s}(1-\xi)-2m^2} - 2\xi\right] \tag{2.5}$$

where λ_{LQ} is the unknown leptoquark coupling constant.

Because λ_{LQ} is much smaller than α_s, the contribution from σ_3 is insignificant and hence will be ignored when the total cross section is calculated.

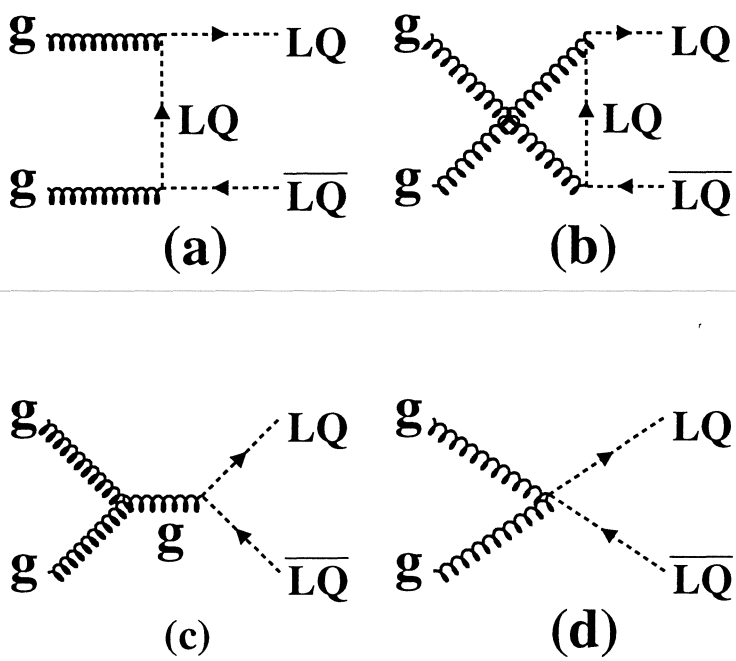

Figure 2.1: Feynman diagrams for leptoquark pair production via gluon-gluon fusion. The dashed lines denote scalar leptoquarks.

2.2.3 Total Cross Section

The total cross section can be obtained by folding the subprocess cross section σ_1 and σ_2 with the proton structure functions [17]:

$$\begin{aligned}
\sigma(p\bar{p} \to LQ\overline{LQ}) &= \sum_{a,b} \int_0^1 d\tau \int_\tau^1 \frac{dx_a}{x_a} \\
&\quad \left[f_{a/A}(x_a) f_{b/B}(\tau/x_a) + (A \leftrightarrow B \text{ if } a \neq b) \right] \hat{\sigma}(\hat{s}) \qquad (2.6) \\
\tau &= x_a x_b \\
\hat{s} &= x_a x_b s = \tau s
\end{aligned}$$

where A, B indicate the proton or antiproton and its 4-momentum, a and b are the associated parton's 4-momentum, x_a and x_b are the Feynman x's, $a = x_a A$ and $b = x_b B$, and $\sqrt{s}$ is the cms energy of the proton-antiproton system. The total cross section thus can be written as:

$$\sigma(p\bar{p} \to LQ\overline{LQ}) = \sum_{i=1}^{3} \int_0^1 d\tau \int_\tau^1 \frac{dx}{x} \left[f_i(x,\hat{s}) f_i(\tau/x,\hat{s})\right] \hat{\sigma}_i(\hat{s}) \tag{2.7}$$

where

$$f_1(x,\hat{s}) f_1(\tau/x,\hat{s}) = g(x,\hat{s}) g(\tau/x,\hat{s}) \tag{2.8}$$

$$\begin{aligned} f_2(x,\hat{s}) f_2(\tau/x,\hat{s}) &= u(x,\hat{s}) u(\tau/x,\hat{s}) + d(x,\hat{s}) d(\tau/x,\hat{s}) + \\ &\quad 2st(x,\hat{s}) st(\tau/x,\hat{s}) + 2sea(x,\hat{s}) sea(\tau/x,\hat{s}) \end{aligned} \tag{2.9}$$

$$\begin{aligned} f_3(x,\hat{s}) f_3(\tau/x,\hat{s}) &= u(x,\hat{s}) u(\tau/x,\hat{s}) + d(x,\hat{s}) d(\tau/x,\hat{s}) + \\ &\quad u(x,\hat{s}) d(\tau/x,\hat{s}) + d(x,\hat{s}) u(\tau/x,\hat{s}) + \\ &\quad 4sea(x,\hat{s}) sea(\tau/x,\hat{s}) \end{aligned} \tag{2.10}$$

Here $g(x,\hat{s})$, $u(x,\hat{s})$, $d(x,\hat{s})$, $st(x,\hat{s})$, $chm(x,\hat{s})$, and $sea(x,\hat{s})$ are *gluon*, *up*, *down*, *strange*, and *sea* distributions for the proton. $u(x,\hat{s})$ and $d(x,\hat{s})$ are actually the sum of *valence* and *sea* distributions. $sea(x,\hat{s})$ is equal to the *sea* distribution of u and d quark.

Equation 2.7 was numerically integrated using the CTEQ3M [18] parton distribution functions. Assuming the unknown leptoquark coupling constant being the electromagnetic coupling strength, the cross section for scalar leptoquark pair production at Tevatron is shown at Fig. 2.3. It is clear that the production cross section (σ_3) due to Fig. 2.2(b) depends on the unknown λ_{LQ} coupling constant and the contribution due to Fig. 2.2(b) is very small even if the electromagnetic coupling strength is assumed. Since most of the fermionic couplings λ_{LQ} of the leptoquarks are assumed to be very small in the mass range up to $\mathcal{O}(1\ \mathrm{TeV}/c^2)$ [16], only the processes in Fig. 2.1 (σ_1) and Fig. 2.2(a) (σ_2) are included to calculate the cross

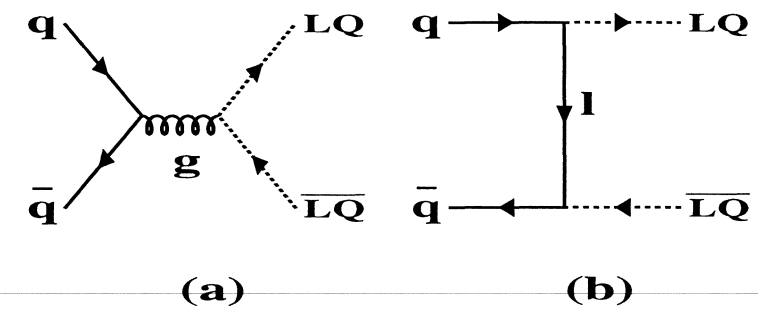

Figure 2.2: Feynman diagrams for leptoquark pair production via $q\bar{q}$ scattering. The dashed lines denote scalar leptoquarks. The contribution from (b) is insignificant and hence ignored when the total cross section is calculated.

section. Thus, the total cross section can be written as:

$$\sigma(p\bar{p} \rightarrow LQ\overline{LQ}) \;=\; \sigma_1 + \sigma_2 \tag{2.11}$$

Equation 2.11 was also numerically integrated using different parton distribution functions: CTEQ3L [18], MRSGFIT [19] and HMRSB300 [20]. Five flavors were selected (except for CTEQ3L when four flavors were selected) and Λ_{QCD}[2] was selected according to Ref. [21] when α_s was calculated. The energy scale was set to the cms energy of the sub-process. Fig. 2.4 shows the theoretical scalar leptoquark pair production cross section at Tevatron with cms energy $\sqrt{s} = 1800$ GeV.

[2] Λ_{QCD} is not predicted by the theory; it is a free parameter chosen as a cutoff energy when the strong coupling constant is calculated. Λ_{QCD} is determined from experiment.

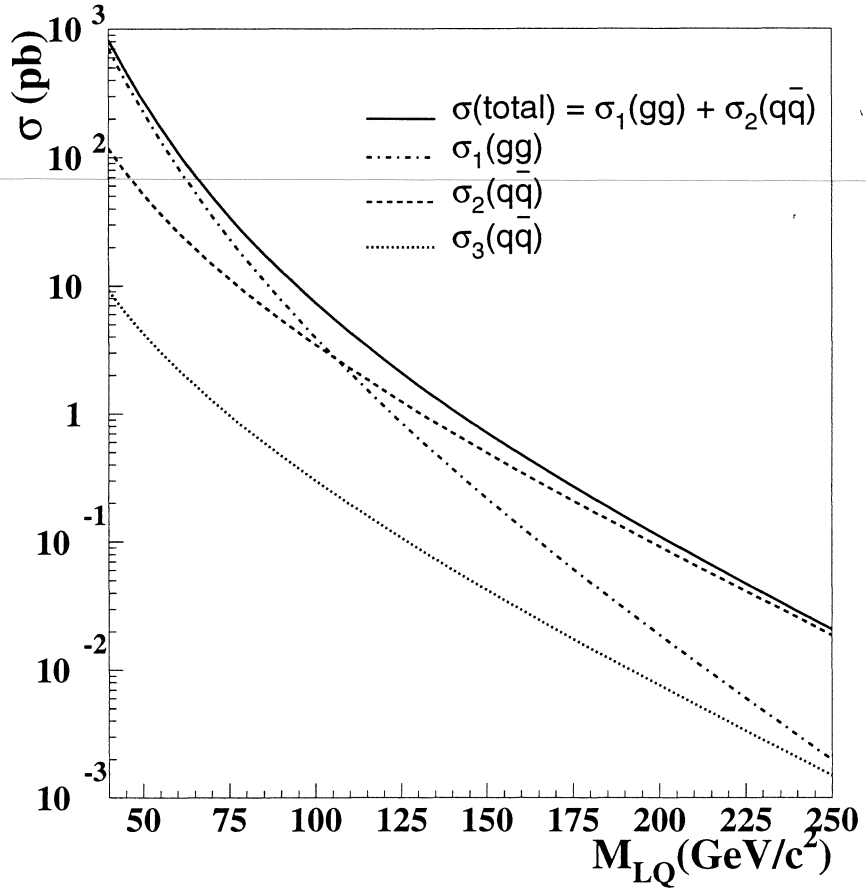

Figure 2.3: Integrated leading order cross sections for scalar leptoquark pair production at Tevatron with $\sqrt{s} = 1.8$ TeV as a function of the leptoquark mass. CTEQ3M ($\Lambda_{QCD} = 158$ MeV) was used as the PDF. Electromagnetic coupling strength was assumed to calculate σ_3.

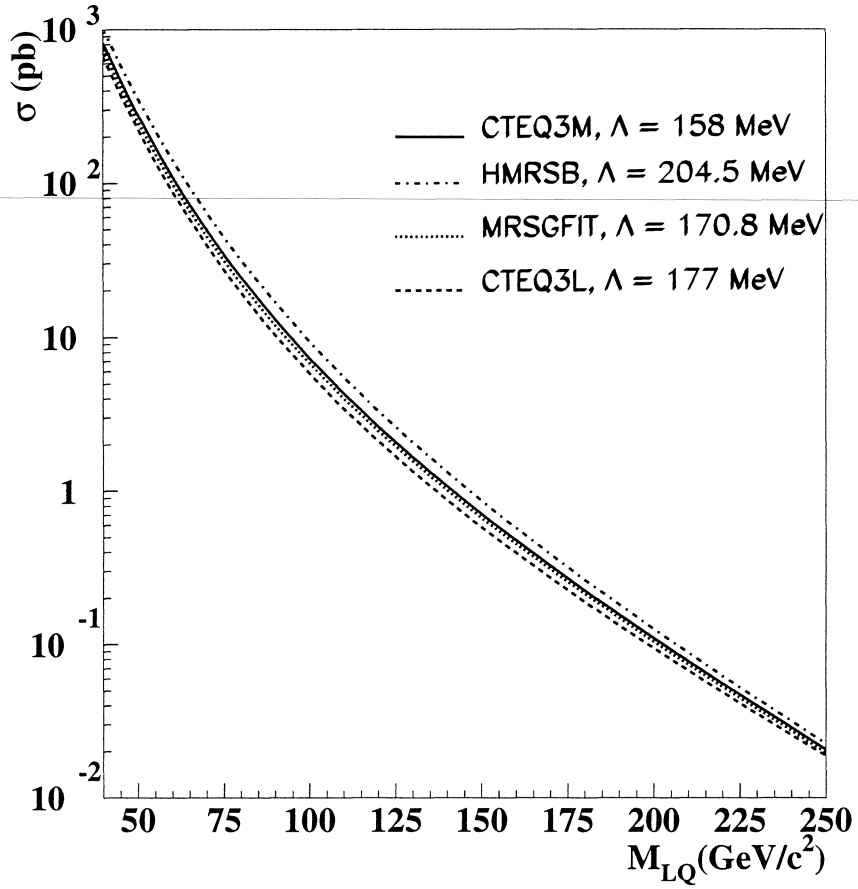

Figure 2.4: Integrated leading order cross sections for scalar leptoquark pair production at Tevatron, $\sqrt{s} = 1.8$ TeV as a function of the leptoquark mass. Results from four different PDF sets are shown. The most modern set is CTEQ3M set. The number of flavors was set to five except that for CTEQ3L which used four flavors when α_s was calculated.

2.3 Next-to-Leading Order Calculations

In the leading order calculation, the dependence of the cross section on the renormalization scale[3] is large, increasing the theoretical uncertainty. Figure 2.6 shows the cross section calculated using three renormalization scales. The difference between these shows the theoretical uncertainty. However, the cross sections in next-to-leading order QCD are under much better theoretical control than the leading-order estimates since the dependence of the cross section on the renormalization scale is reduced.

The QCD radiative corrections to order α_s include virtual corrections, the bremsstrahlung of gluons, and contributions from gluon-quark interactions. The virtual corrections can be classified in self-energy diagrams and vertex corrections for quarks, gluons and leptoquarks, and initial/final state from scalar vertices. Finally, the inelastic Compton process, shown in Figure 2.5, is added at order α_s^3. After these corrections, the total scalar leptoquark pair production cross section is calculated using the CTEQ4M parameterization of the parton densities [22]. The QCD coupling constant is evaluated for $n_f = 5$ active flavors and $\Lambda_{QCD} = 202$ MeV. The result is shown in Figure 2.6 [23].

2.4 Signatures for this Search

As described in Section 2.2, this study is a search for the first generation scalar leptoquark, which couples only to the first generation leptons and quarks. The production and decay chain under study is:

$$p\bar{p} \rightarrow LQ\overline{LQ} \tag{2.12}$$

[3]The renormalization scale μ is a free parameter. It is introduced to replace the different cutoff momentum transfer for the calculation of coupling constant. Different choices of μ will lead to different calculation expansions of invariant amplitude, and thus represent different renormalization schemes.

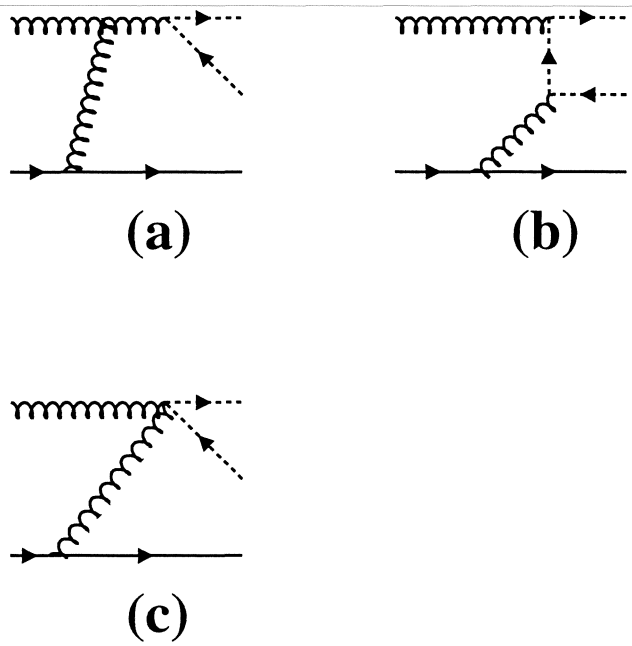

Figure 2.5: The gluon–quark sub-processes.

with the subsequent decay mode of LQ:

$$\begin{aligned} LQ &\rightarrow e^- u \text{ or } \nu_e d & (Q &= -\frac{1}{3}) \\ &\rightarrow e^+ d \text{ or } \nu_e u & (Q &= +\frac{2}{3}) \end{aligned} \tag{2.13}$$

Electrons and positrons can be identified by the presence of a track from charged particles and their energy deposition. u and d quarks will hadronize by forming jets which can be identified by their energy deposition. Since neutrinos only interact weakly, they will escape the DØ detector and lead to "missing" energy.

If both leptoquarks decay to an electron (e^+ or e^-) and a quark (u or d), the signature will be 2 e + 2 jets. If one leptoquark decays to an electron and a quark while the other decays to a neutrino and a quark, the signature will be 1 e + 2 jets + missing transverse energy E_T ($\not{E}_T$). The transverse energy E_T is measured along the direction which is 90° from the proton-antiproton beam direction. If both leptoquarks decay to a neutrino and a quark, the signature will be 2 jets + $\not{E}_T$. In this thesis, the 2 e + 2 jets and 1 e + 2 jets + $\not{E}_T$ final states are studied.

2.5 Existing Limits

Since leptoquarks were first predicted, much theoretical and experimental work has been done to constrain the coupling constants and the mass of leptoquarks.

The production of leptoquarks at the DESY ep collider, HERA, is dependent on the unknown leptoquark coupling constant. In ep collisions, a LQ would be produced as an s-channel resonance via electron-quark fusion. LQs decaying into eq or νq have event topologies identical to neutral-current or charged-current deep-inelastic scattering events. The ZEUS group searched for all $SU(3)_c \times SU(2)_Y \times U(1)$ invariant first generation LQs which conserve baryon and lepton numbers. Based on data samples of 0.82 pb^{-1} (e^-p) and 9.3 pb^{-1} (e^+p), they set limits on coupling $vs.$ mass for the various leptoquark species [24]. For electromagnetic coupling strength,

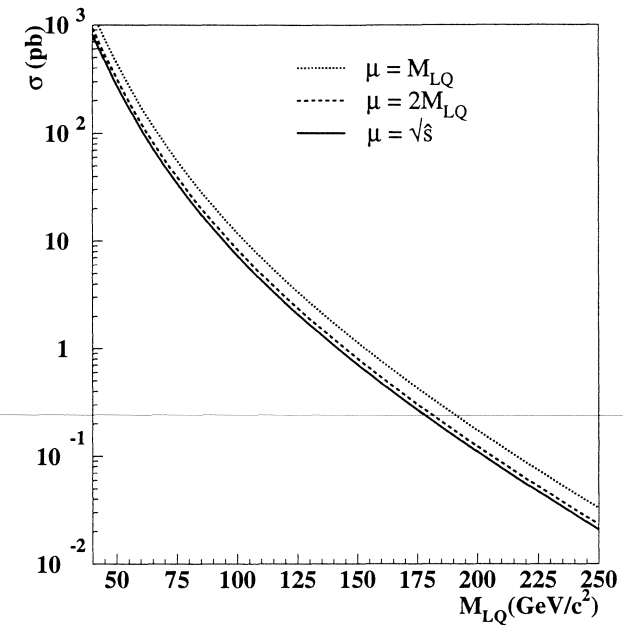

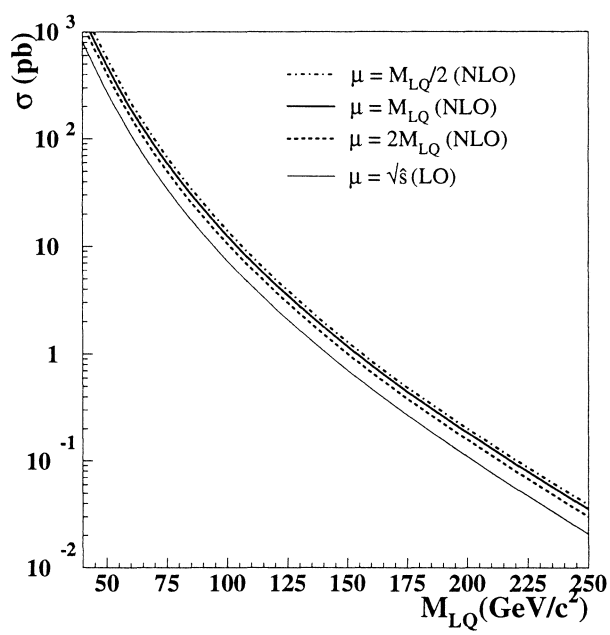

Figure 2.6: The LO and NLO calculation for different renormalization scales. The upper figure shows the dependence of the LO cross section on different renormalization scale. The lower figure shows the dependence of the NLO cross section on different renormalization scales.

scalar leptoquarks which decay to eq were excluded at the 95% confidence level for all masses less than 248 GeV/c^2. The H1 group at HERA also searched for LQs in direct positron-quark fusion processes taking into account possible decays into lepton quark pairs of either the first, second, or third generation. Using e^+p data corresponding to an integrated luminosity of about 3 pb^{-1}, they excluded scalar leptoquarks with mass less than 275 GeV/c^2 if the coupling value is larger then $\sqrt{4\pi\alpha_{em}}$.

The four experiments at the CERN Large Electron-Positron Collider (LEP), OPAL, DELPHI, ALEPH and L3, have searched for scalar, family-diagonal leptoquarks through the decay of Z^0 bosons based on 5 pb^{-1} of data collected at the cms energy $88.2 \leq \sqrt{s} \leq 94.2$ GeV [25]. The null result allowed them to exclude scalar leptoquarks with masses below 45 GeV/c^2.

The CDF and DØ collaborations at Fermilab have published results on their searches for pair produced first generation scalar leptoquarks at the Tevatron [26, 27]. It can be seen from Section 2.2.2 that the hadron colliders have the advantage that the pair production of scalar leptoquarks is relatively independent of the unknown coupling constant. Thus the search at the Tevatron is almost model independent. With 4.05 pb^{-1} data collected, CDF set a first generation scalar leptoquark mass limit of $M_{LQ} > 113$ GeV/c^2 for $\beta = 1$ (β is the branching fraction of leptoquark decaying into electron and u/d quark) and $M_{LQ} > 80$ GeV/c^2 for $\beta = 0.5$ at the 95% confidence level. The DØ collaboration searched for first generation scalar leptoquarks decaying into electrons and u/d quarks and neutrinos and u/d quarks using a data sample of 15 pb^{-1} based on the data collected in 1992–1993. DØ excluded first generation scalar leptoquarks with mass less than 133 GeV/c^2 for $\beta = 1$ and with mass less than 120 GeV/c^2 for $\beta = 0.5$ at the 95% confidence level.

CHAPTER 3

THE APPARATUS

3.1 The Tevatron

The Tevatron is the highest energy accelerator in the world today. It is located at Fermilab in Batavia, Illinois and is a proton-antiproton collider with center of mass energy of 1.8 TeV (10^{12} electron volts). The Tevatron is the last in a chain of accelerators which produce proton and antiproton bunches. The protons and antiprotons are accelerated to 900 GeV (10^9 electron volts) and then collide. Two of the six collision points are BØ and DØ. The two general purpose detectors CDF and DØ are located at BØ and DØ respectively.

The Tevatron is schematically shown in Fig 3.1. The starting point for the chain of the accelerators is a Cockroft-Walton accelerator. Electrons are added to hydrogen atoms to make negative hydrogen ions and the beam of H^- ions is accelerated to an energy of 750 keV (10^3 electron volts). The H^- ions are then injected into a linear accelerator called the Linac. The Linac is made of nine drift tubes which have an alternating electric field which accelerates the H^- ions when the beams emerge into the gaps between the tubes. The H^- ions are accelerated to 400 MeV (10^6 electron volts). After leaving the Linac the beam passes through a carbon foil where the two electrons in the H^- ions are striped off and H^+ (protons) ions are produced. Then the protons are injected into a synchrotron (the Booster) and are accelerated to an energy of 8 GeV (10^9 electron volts). Thereafter the protons are injected into a much larger synchrotron (the Main Ring) where the protons are accelerated to an energy of 120 GeV. The Main Ring is inside an underground tunnel

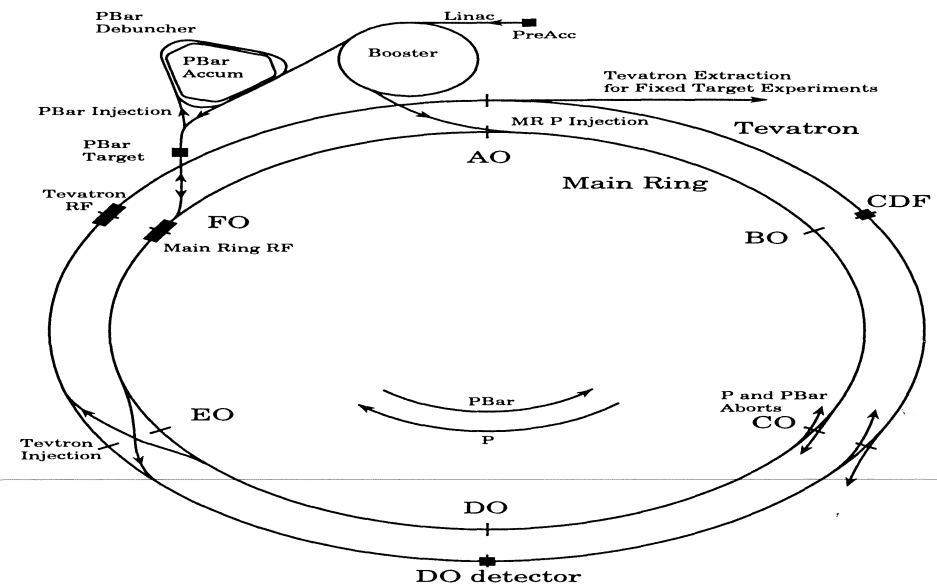

Figure 3.1: The schematic view of the Tevatron.

which is about 6 kilometers in circumference. The Main Ring is made up of dipole and quadrupole magnets and radio frequency cavities (RF cavities).

The 120 GeV protons are then extracted from the Main Ring and injected into the Tevatron which is inside the same underground tunnel that holds the Main Ring.

Some of the 120 GeV proton bunches are extracted to hit on a copper and nickel target. Due to the strong interaction between the target and the energetic protons, many new particles including antiprotons are produced. Because antiprotons produced in this way have a wide range of momenta, antiprotons are extracted to a antiproton source ring where antiproton bunches are reduced in size by a method known as stochastic cooling [28]. After enough antiprotons have been accumulated, six bunches of antiprotons are injected into the Main Ring where the antiprotons are accelerated to an energy of 120 GeV. Then the antiprotons are injected into the Tevatron in the opposite direction to that of the proton bunches. The Tevatron is made of superconducting magnets and RF cavities. Protons and antiprotons are accelerated up to 900 GeV and then collide.

3.2 The DØ Detector

The DØ detector is a general purpose collider detector to study proton-antiproton collisions at $\sqrt{s} = 1.8$ TeV. A cutaway view of the DØ detector is shown in Fig. 3.2. The design goals of the DØ detector were to provide excellent energy and position resolution, good electron and muon identification and measurement, good measurement of jets at large transverse momentum p_T through highly segmented calorimeter with good energy resolution and good missing transverse energy E_T ($\not{E}_T$) measurement as a means of signalling the presence of neutrinos and other non-interacting particles. The primary physics goal of the DØ detector is the study of high mass states and large p_T phenomena.

The DØ detector consists of three major detector components:

A compact tracking system which has good spatial resolution and no central magnetic field.

A hermetic, finely segmented liquid argon uranium calorimeter with stable gain.

A Muon detector surrounding a thick magnetized iron toroid which provides sufficient momentum measurement while minimizing backgrounds from hadron punchthrough.

A detailed description of the detector is available in Ref. [29] and references therein. In this chapter only a brief overview of the detector elements is given.

The DØ coordinate system is a right-handed coordinate system, in which the z-axis is along the proton direction and the y-axis is upward. The angles ϕ and θ are the azimuthal and polar angles with $\theta = 0$ along the proton beam direction. The r-coordinate denotes the perpendicular distance from the beam axis. The pseudo-rapidity, $\eta = -\ln(\tan(\theta/2))$, is approximately equal to the true rapidity $y = 1/2\ln((E + p_z)/(E - p_z))$ in the limit that $(m/E) \rightarrow 0$.

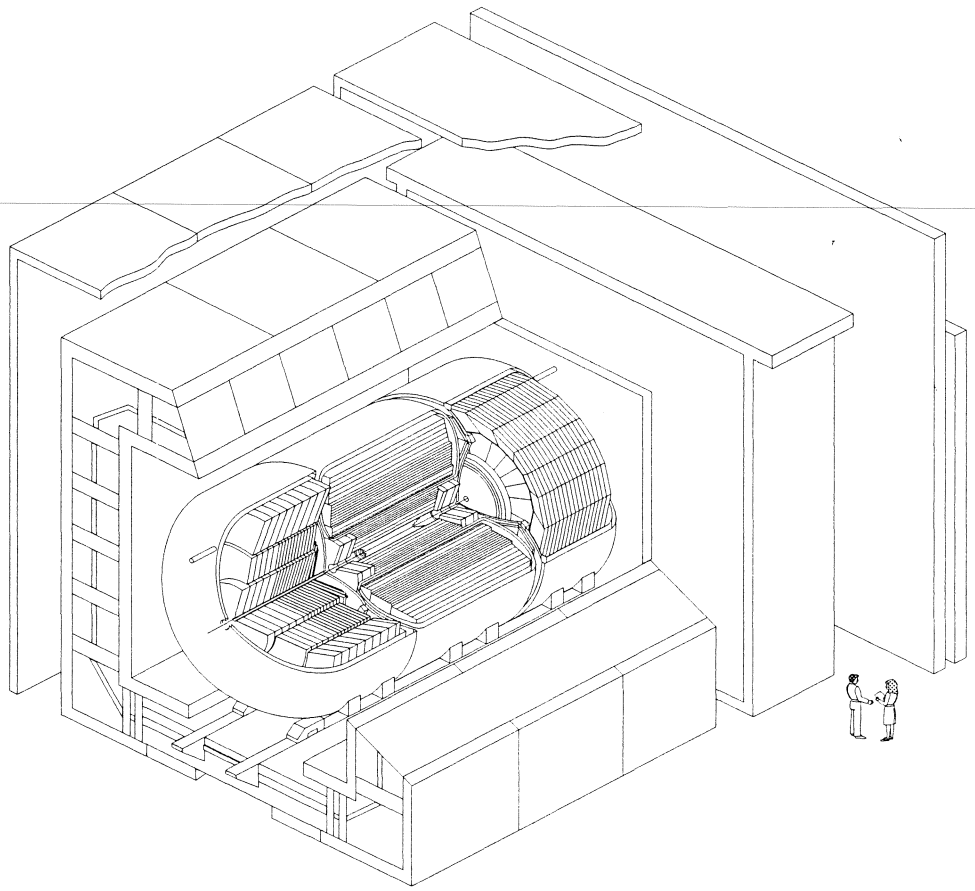

DØ Detector

Figure 3.2: A cutaway view of the DØ detector.

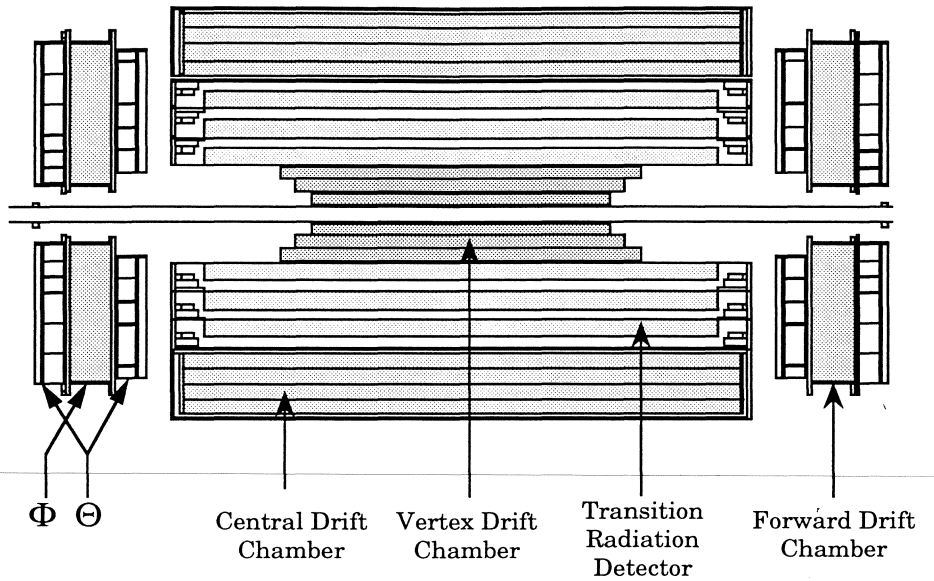

Figure 3.3: A schematic picture of the central detector.

3.2.1 Central Detectors

The central detectors are shown in Fig. 3.3. Because there is no central magnetic field, the central detectors were designed and optimized for good two-track resolution, high efficiency, and good ionization energy measurement so as to distinguish single electrons from closely-spaced conversion pairs. The transition radiation detector was included to gain an additional factor of about 50 for rejection of isolated pions beyond that given by the calorimeter alone. The scale for track spatial resolution was set by the need for primary z-vertex determination and by calorimeter shower matching to be about 1 mm. Good track-fitting efficiency and recognition of $\pi(K) \rightarrow \mu$ decay kinks benefit from the best resolution that can be attained.

The recovery time of the central detector was designed to match the collider bunch-time interval of 3.5 μs. A flash analogue-to-digital conversion (FADC) system is used for signal digitization with a charge sampling time interval of $\approx$10 ns. This provides good two-track resolving power and obtains an effective detector granularity of 100–350 μm. Charge division in the vertex chamber, helical cathode pads in

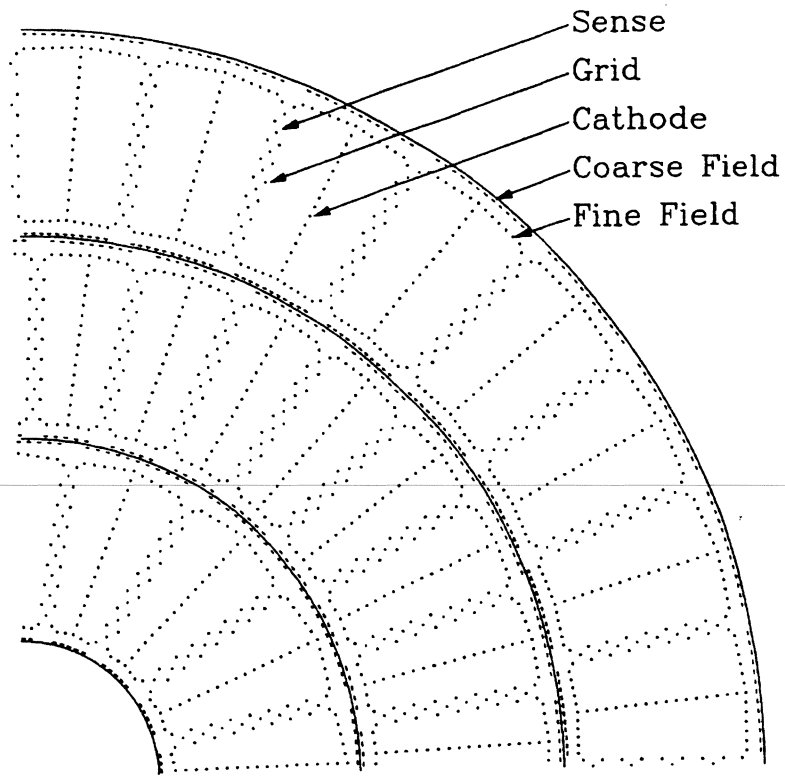

Figure 3.4: The VTX chambers.

the transition radiation detector and delay lines in the central and forward drift chamber are used to obtain robust measurement of the z-coordinate in the large angle chambers.

Vertex (VTX) Chamber. The VTX chamber is the innermost tracking detector in DØ. The inner radius of the VTX is 3.7 cm; the outer radius is 16.2 cm. There are three mechanically-independent, concentric layers of cells in the VTX chamber which is shown in Fig. 3.4. The innermost layer has 16 cells in azimuth; the outer two layers have 32 cells each. In each cell, tight sense wires provide measurement of the $r-\phi$ coordinate. Adjacent sense wires are staggered by ± 100 μm to resolve left-right ambiguities; the cells of the three layers are offset in ϕ to further aid pattern recognition and to facilitate calibration. The sense wires are 25 μm NiCoTin

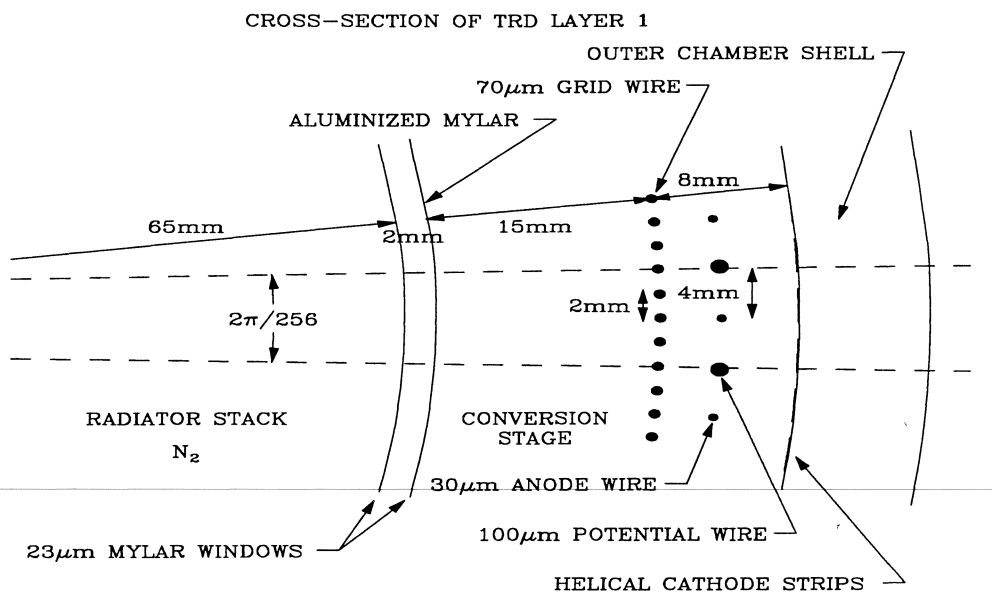

Figure 3.5: Cross sectional view of the TRD.

at 80 g tension. Field and grid wires are made of 152 μm gold-plated aluminum at a tension of 360 g. The gas chosen for operation of the VTX is CO_2(95%)-ethane(5%) at one atmosphere with a small admixture of H_2O to obtain good spatial resolution and track pair resolving power. The gas is unsaturated at the DØ operating conditions.

The resolution in the z direction is 6 mm. The resolution at the $r - \phi$ plane is 60 μm. It is 90% efficient to detect two hits if the separation of the two hits is 0.63 mm; the detection efficiency is higher for larger separation.

Transition Radiation Detector (TRD). The TRD is located outside the shell of the VTX. The purpose of the TRD is to provide independent electron identification in addition to that given by the calorimeters. A π^0 decaying into two unresolved photons looks to the calorimeter and drift chambers much like an electron if it is overlapped by a charged track such as that of a low energy $\pi^{\pm}$. TRD is used to distinguish low energy charged particles overlapped by an energetic neutral

pion from high energy electrons because highly relativistic particles ($\gamma > 10^3$) produce X-ray transition radiation when crossing boundaries between materials with differing dielectric constants.

The DØ TRD shown in Fig. 3.5 consists of three separate units, each containing a radiator and an X-ray detection chamber. The radiator section of each TRD unit consists of 393 foils of 18 μm thick polypropylene in a volume filled with nitrogen gas. The mean gap between foils is 150 μm. The detection of X-rays is accomplished in a two-stage time-expansion radial-drift PWC mounted just after the radiator. The X-rays convert mainly in the first stage of the chamber. The resulting charge drifts radially outward to the sense cells, where the avalanche occurs. The radiator and detector volumes are separated by a pair of 23 μm window. Dry CO_2 gas flows through the gap between these two windows to keep the nitrogen in the radiator from leaking into the detector volume and polluting the recirculating chamber gas, a mixture of $Xe(91\%)/CH_4(7\%)/C_2H_6(2\%)$. The outer window is aluminized and serves as a high-voltage cathode for the drift field in the conversion stage of the detection chamber.

In this analysis, information from the TRD is not used.

Central Drift Chamber (CDC). The CDC provides coverage for tracks at large angles ($30° - 90°$ relative to the beam line). It is located between the TRD and the Central Calorimeter. The purposes of the CDC are to find the z position of the interaction vertex, to provide tracks to distinguish between electrons and photons found in the calorimeter and to aid in the identification and momentum measurement of muons seen in the muon detector. It is a cylindrical shell of length 184 cm and radii between 49.5 and 74.5 cm. It consists of four concentric shells of 32 azimuthal cells per shell. The CDC chambers are shown in Fig. 3.6. Each cell contains seven 30 μm gold-plated tungsten sense wires, read out at one end, and two

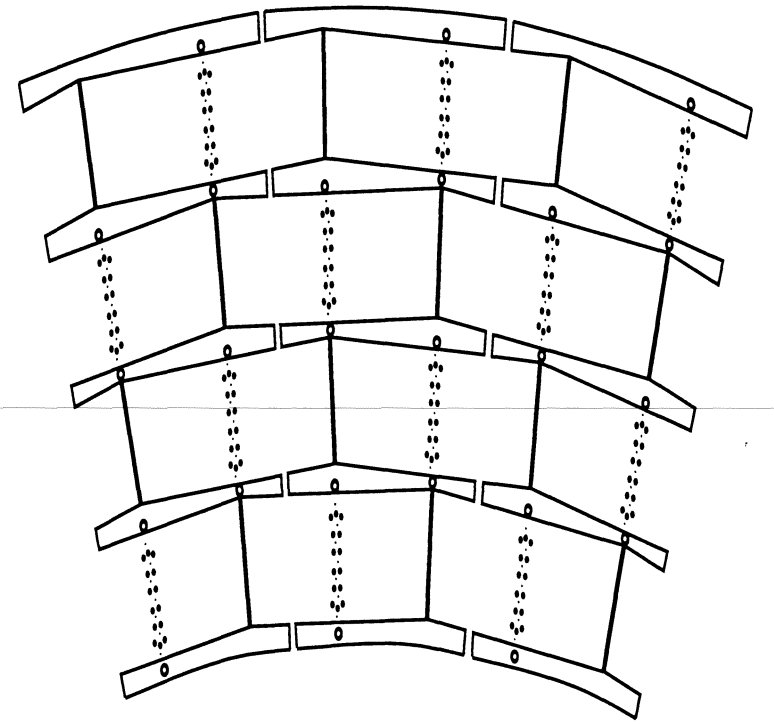

Figure 3.6: The CDC chambers.

delay lines, each read out at both ends. Adjacent wires within the cell are staggered in ϕ by 200 μm to remove the left-right ambiguity. Alternate cells in radius are offset by one half cell to further aid in pattern recognition.

The outer cylinder is 0.95 cm aluminum and serves as the main support for the full central detector. The delay lines embedded in the inner and outer shelves of each cell propagate signals induced from the nearest anode wire; measurement of the difference of arrival times at the two ends permits location of the track along the z-coordinate. Surrounding the first and last anode wires an additional grounded potential wire is added to the usual pair of potential wires between anodes to minimize the signal induced upon the delay line from inner sense wires.

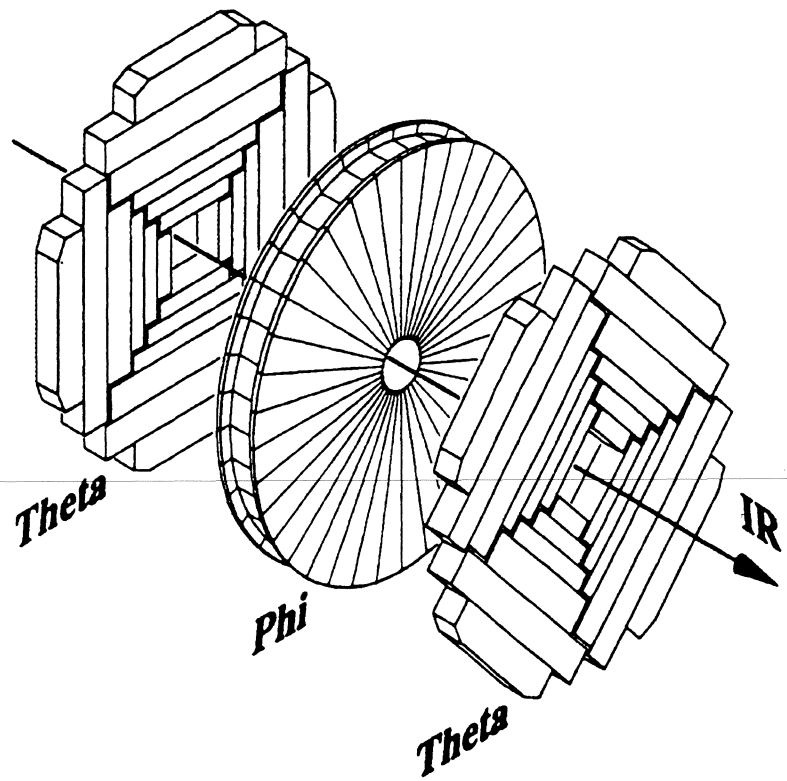

Figure 3.7: The FDC package.

The operating gas in the CDC is Ar(92.5%)CH_4(4%)CO_2(3%) with 0.5% H_2O. A single layer scintillating fiber detector for spatial calibration is located between the CDC and surrounding Central Calorimeter covering about 1/32 of the full azimuth.

The resolution in the z direction is 2 mm. The resolution in the $r - \phi$ plane is 180 μm. The efficiency to detect two hits is 90% if the separation of the two hits is 2 mm; the detection efficiency is higher for larger separation.

Forward Drift Chambers (FDC). The FDC is located at either end of the concentric barrels of the VTX, TRD, and CDC, just before the entrance wall of the end calorimeters: one is located at the north end of the CDC and one at the south. The FDC extend the coverage for charged particle tracking down to 5° from the

beam. There is a small gap between the outer radius of the FDC and the CDC to allow cables from the inner detectors to exit the detector.

The FDC consists of two identical sets of packages. Each FDC package (shown in Fig. 3.7) consists of three separate chambers: a Φ module whose sense wires are radial and measure the ϕ coordinate, is sandwiched between a pair of Θ modules whose sense wires measure separately the θ coordinate. The Φ module is a single chamber containing 36 sectors over the full azimuth, each with 16 anode wires along the z direction. Each Θ module consists of four mechanically separate quadrants, each containing six rectangular cells at increasing radii. Each cell contains eight anode wires in z direction. In order to remove the left-right ambiguity, the sense wires in the three inner cells are at one edge of the cell, allowing the electrons drift in just one direction. The delay line for each Θ cell is identical to that of the CDC in order to give local measurement of the orthogonal coordinate. All adjacent anode wires (in z) of both Θ and Φ modules are staggered by ± 200 μm to help resolve ambiguities. The upstream and downstream Θ modules are rotated by 45° in ϕ with respect to each other. The operation gas for FDC is the same as the CDC, with similar values of the drift field and gas gain.

The resolution in the z direction is 2 mm. The resolution in the $r - \phi$ plane is 200 μm. The efficiency to detect two hits is 90% if the separation of the two hits is 2 mm, the larger separation, the larger detecting efficiency.

3.2.2 Calorimeters

The calorimeter is the key part of the DØ detector. Because there is no central magnetic field, the calorimetry must provide the energy measurement for electrons, photons and jets. Moreover, the calorimeters play an important role in the identification of electrons, photons, jets and muons, and in establishing the transverse energy balance in an event.

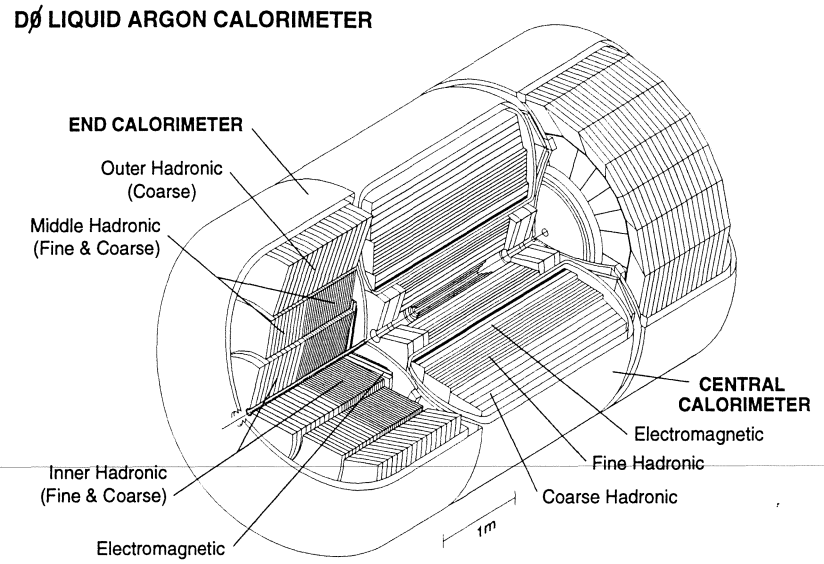

Figure 3.8: The layout of the calorimeter.

The calorimeters are housed in three cryostats, one each for the Central Calorimeter (CC), and the North and South End Calorimeters (ECN and ECS). In the space between the CC and EC a set of scintillating tiles and associated phototubes called the Intercryostat Detector (ICD) is deployed. Figure 3.8 shows the layout of the CC and EC calorimeters located in the three cryostats and the location of the central detectors in relation to the calorimeters. Figure 3.9 shows the side view of one quarter of the full calorimeter and the central detectors. The CC covers roughly $|\eta| \leq 1.2$ and the EC's extend the coverage out to $|\eta| \approx 4$.

Each of the calorimeters is divided into electromagnetic and hadronic layers. The electromagnetic layers are optimized to identify and measure objects such as electrons and photons. The hadronic layers are designed to identify and measure jets. Inclusion of the coarse-hadronic section allows sampling at the end of hadronic showers while keeping the density high in order to avoid punch through of jets to the muon detector.

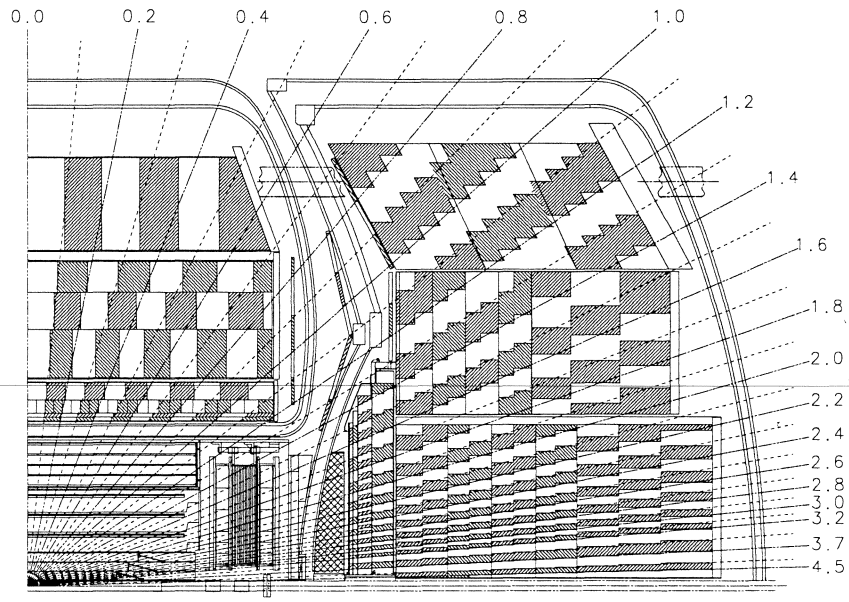

Figure 3.9: The side views of one quarter of the full calorimeter and the central detectors.

Liquid argon was chosen as the active media because liquid argon has the unit gain, the relative simplicity of calibration, the good radiation hardness, and the relatively low unit cost for readout electronics.

Central Calorimeter(CC). The central calorimeter (CC) covers the region $|\eta| \leq 1.2$. The CC includes three concentric cylindrical shells. The inner shell is the EM section which is made up of 32 separate modules. The middle shell in CC contains 16 separate fine hadronic (CCFH) modules. The outer shell in CC is the coarse hadronic (CCCH) which is made up of 16 modules. The three shells are rotated relative to one another so that particles encounter no more than one intermodule ϕ gap. The transverse segmentation is typically 0.1×0.1 in $\eta \times \phi$ space.

The CCEM modules have four longitudinal layers which are approximately 2.0, 2.0, 6.8, and 9.8 radiation length X_0[1]. The third layer covers the depth at which the maximum of the EM shower is located. This layer has transverse segmentation of 0.05×0.05 in $\eta \times \phi$ space. A full CCEM module comprises 20.8 radiation length X_0 and 0.76 nuclear absorption length λ_A[2] and weighs 0.6 metric tons.

The CCFH modules have three longitudinal layers which are approximately 1.3, 1.0 and 0.9 λ_A. The CCCH modules contain just one layer which is 3.2 λ_A. The CCFH (CCCH) modules weigh 8.3 (7.2) metric tons.

End Calorimeter(EC). The two mirror-image end calorimeters ECN and ECS have four module types as shown in Fig. 3.8: one ECEM module, two inner hadronic (IH) modules, 16 middle hadronic (MH) modules and 16 outer hadronic (OH) modules. MH and OH modules are outside the ECEM and IH modules. They are offset to prevent cracks through which particles could penetrate the calorimeter.

The ECEM module contains four layers which are 0.3, 2.6, 7.9 and 9.3 X_0 each with outer radii varying between 84 and 104 cm and inner radius of 5.7 cm. The two ECIH modules are cylindrical with inner and outer radii of 3.92 and 86.4 cm. The fine hadronic portion consists of four readout sections with 1.1 λ_A each. The coarse hadronic portion has a single readout section with 4.1 λ_A. Each of the ECMH modules has 4 fine-hadronic sections with 0.9 λ_A each and a single coarse-hadronic section of 4.4 λ_A. The ECOH modules modules use stainless steel plates inclined at an angle of about 60^0 with respect to the beam axis.

[1]Radiation length X_0 is the mean distance over which a high-energy electron loses all but $1/e$ of its energy by bremsstrahlung.

[2]Nuclear absorption length λ_A is the mean distance over which the number of particles becomes $1/e$ of the original number of particles.

Intercryostat Detector (ICD). As shown in Fig. 3.9, there is a gap between the CC and EC. The material profile along a particle path varies rapidly with rapidity through the region $0.8 \leq |\eta| \leq 1.4$ because this region contains a large amount of uninstrumented material such as cryostat walls, stiffening rings, and module end plates. To correct for energy deposited in the uninstrumented walls, two scintillation counter arrays called intercryostat detectors (ICD) are mounted on the front surface of the ECs. Each ICD consists of 384 scintillator tiles of size $\delta\eta = \delta\phi = 0.1$ exactly matching the calorimeter cells. In addition, separate single-cell structures called "massless gaps" also shown in Fig. 3.9 are installed in both CC and EC calorimeters. One ring with standard segmentation is mounted on the end plates of the CCFH modules; additional rings are mounted on the front plates of both ECMH and ECOH modules. Together, the ICD and massless gaps provide a good approximation to the standard DØ sampling of hadron showers.

Calorimeter Performance. The DØ calorimeters have been tested in a variety of ways. Prototype studies in test beams have verified performance goals and led to the optimization of the design. Combinations of the CCEM/CCFH and ECMH modules as well as the ECEM/ECIH modules have been tested in a test beam. The full CC calorimeter was tested using cosmic rays. Extensive studies of the performance of modules were made using pions and electrons with energies between 10 and 150 GeV.

For the ECEM/ECIH modules, the response to both electrons and pions is linear with particle energy for momentum greater than 10 GeV to within 0.5%. After subtraction of pedestals, and after corrections for gain variations and beam particle momentum, the relative energy resolution for electrons and pions as a function of energy for CCEM, ECEM and ECMH modules can be parameterized as

$$\left(\frac{\sigma_E}{E}\right)^2 = C^2 + \frac{S^2}{E} + \frac{N^2}{E^2} \tag{3.1}$$

Where the constants C, S and N represent the calibration errors, sampling fluctuations, and noise contributions respectively. For electrons in the CCEM, the measured values of these constants are $C = 0.003 \pm 0.004$, $S = (0.162 \pm 0.011)\sqrt{\text{GeV}}$ and $N = 0.140$ GeV. For electrons in the ECEM the measured values of these constants are $C = 0.003 \pm 0.003$, $S = 0.157 \pm 0.006\sqrt{\text{GeV}}$ and $N = 0.29 \pm 0.03$ GeV. For pions in ECMH, the measured values of these constants are $C = 0.047 \pm 0.005$, $S = 0.439 \pm 0.042\sqrt{\text{GeV}}$ and $N = 1.28$ GeV. Ignoring the noise term, the EM calorimeter resolution measured with an ECEM module in the electron test beam was determined to be:

$$\frac{\sigma(E_{EM})}{E_{EM}} = 0.3\% \oplus \frac{16\%}{\sqrt{E_{EM}}} \tag{3.2}$$

and the hadronic resolution measured with an ECMH module in a pion beam is

$$\frac{\sigma(E_{had})}{E_{had}} = 3.2\% \oplus \frac{50\%}{\sqrt{E_{had}}} \tag{3.3}$$

where $\oplus$ indicates addition in quadrature [30, 31, 32, 33].

The calorimeter position resolution is important for rejection of backgrounds to electrons from the near-overlap of photons and charged particles. For ECEM layer 3, the resolution varies between 0.8 and 1.2 mm over the full range of impact positions; the position resolution varies approximately as $E^{-\frac{1}{2}}$. The resolution and linearity obtainable in the calorimeter is closely related to the ratio of the responses to electrons and pions. The e/π response ratio falls from about 1.11 at 10 GeV to about 1.04 at 150 GeV [34].

3.2.3 Muon Detector

The DØ muon detector consists of five separate toroidal magnets, together with sets of proportional drift tube chambers (PDT's). Figure 3.10 shows the elevation view of the DØ detector with the five muon detector toroids and their associated PDT layers. The purpose of the muon system is designed to measure the trajectories

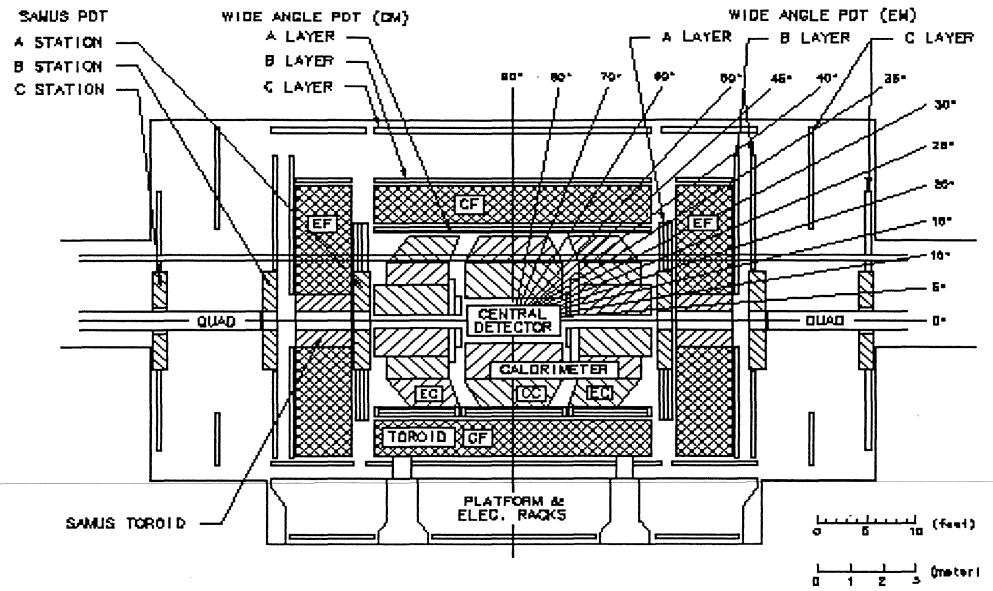

Figure 3.10: The elevation view of the DØ detector.

and momenta. The incident trajectory is determined from a combination of the primary interaction point, the track seen in the central tracking and the first muon chamber track vector. A comparison of incident and exit muon directions provides the bend angle in the toroid. The muon momentum is directly related to the bend angle. With final precise alignment of the muon chambers, three standard deviation determination of the signal is expected for $p_T \leq 200$ GeV/c at $\eta = 0$ and $p_T \leq 30$ GeV/c at $|\eta| = 3.3$.

The central toroid (CF) covers the region $|\eta| \leq 1$ and two end toroids (EFs) cover $1 < |\eta| \leq 2.5$. The small-angle muon system (SAMUS) toroids fit in the central hole of the EF toroids and cover $2.5 < |\eta| \leq 3.6$. Figure 3.11 shows the interaction length for one quarter of the DØ detector. The muon system and calorimeter are quite thick and affords a clean environment for identification and momentum measurement of high p_T muons. The wide angle muon system (WAMUS) provides measurements for all muons traversing the CF and most of those which cross the EF toroids.

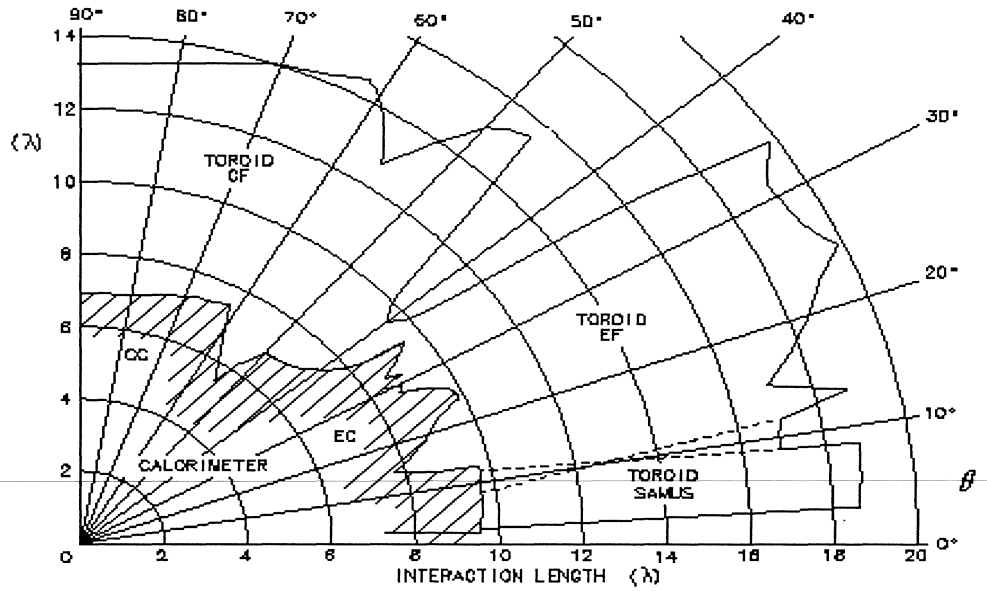

Figure 3.11: The interaction length of the detector.

The WAMUS chambers are deployed in three layers: the "A" layer before the iron toroids and the "B" and "C" layers after the magnets. There are 4 PDT planes in an A layer chamber and 3 PDT planes in the B and C layer chambers. The cell structure for the PDT's is the same for all WAMUS. There are total 164 individual WAMUS chambers. The chambers are operated using the gas mixture Ar(90%)/CF_4(5%)/CO_2(5%).

The SAMUS system consists of three stations: the A station in front of the SAMUS toroid and the B and C stations between the toroid and the beginning of the low beta quadrupole for the DØ proton–antiproton collision point. Each station consists of three doublets of PDTs. There is a total of 5308 tubes in the SAMUS system.

The position resolution of the muon system is about ± 0.3 mm. The corresponding momentum resolution is

$$\frac{\sigma(p)}{p} = 20\% \oplus 0.01p \tag{3.4}$$

where $\oplus$ indicates the addition in quadrature and p is the muon momentum.

3.3 Trigger and Data Acquisition System

The DØ trigger and data acquisition systems are used to select and record interesting events. Fig. 3.12 shows a diagram of the DØ data acquisition system. Detailed information about the DØ trigger and data acquisition system can be found in Ref.'s [35, 36]. Only a brief introduction is given here. The DØ trigger system consists of three levels. The Level 0 (L0) trigger consists of two set of scintillators indicating the occurrence of an inelastic collision. The Level 1 (L1) trigger consists of 32 orthogonal AND-OR hardware lines. The Level 2 (L2) trigger is the software event-filtering process to identify the particle types or event characteristics.

3.3.1 Level 0 Trigger

The Level 0 trigger signals the occurrence of inelastic collisions and monitors the beam luminosity for the experiment. It consists of two hodoscopes built of scintillation counters. The scintillation counters are mounted on the front surfaces of the two end calorimeters. The L0 is more than 99% efficient in detecting non-diffractive inelastic collisions.

In addition to identifying inelastic collisions, the Level 0 trigger provides information on the primary collision vertex z-coordinate. The z-coordinate is determined from the difference in arrival time for particles hitting the two L0 detectors. If there is a probability for multiple interactions, the Level 0 time difference information is ambiguous and a flag is set and passed to the subsequent trigger levels.

The Tevatron luminosity is obtained independently for each beam crossing, Level 0 coincidence with $|z_{vtx}| < 100$ cm, and single hits in groups of similar counters with and without valid coincidences.

3.3.2 Level 1 and 1.5 Trigger

The overall control of Level 1 trigger components and the interface to the next higher level trigger resides in the Level 1 framework. The framework gathers infor-

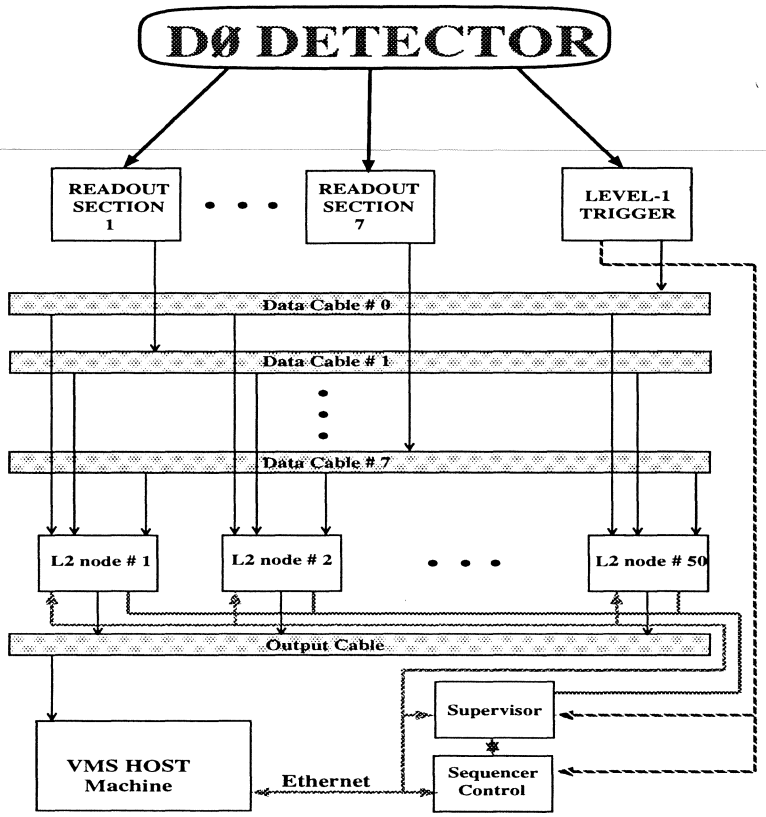

Figure 3.12: The DØ data acquisition system.

mation from each of the specific Level 1 trigger devices, coordinates various vetos, provides the prescaling of triggers too copious to pass on, correlates the trigger and readout function, manages the communication tasks with the front-end electronics and with the Trigger Control Computer (TCC), and provides a large number of scalers which allow accounting of trigger rates and dead-times.

The selection of triggers is performed with an AND-OR Network. The input bits of the network consists of specific pieces of detector information. The outputs are 32 orthogonal AND-OR lines correspond to 32 specific Level 1 triggers. If Level 1.5 confirmation of a specific trigger is required, the framework forms the Level 1.5 decision and communicates the results to the data acquisition hardware. Any interactions with the Level 1 trigger system occur through the TCC and the configurations of the active specific triggers are downloaded from the host computer to the TCC.

The Level 1 trigger consists of both calorimeter and muon trigger hardware. No Level 1 muon triggers were used in this analysis.

The Level 1 calorimeter trigger is activated when it receives the signal from Level 0 indicating that an inelastic collision occurred. The system operates on the analog trigger pickoff from the calorimeter baseline subtractor (BLS) circuits, summed into 0.2×0.2 (in $\eta \times \phi$ space) trigger towers. The EM and hadronic sections of the calorimeter use separate inputs. Each input signal voltage is analog-weighted by the sine of the trigger tower polar angle to give the transverse energy appropriate for an interaction vertex at $z = 0$. This weighted signal is then digitized in a fast 8-bit flash ADC. The 8-bit digital information from the flash ADC provides part of the address for several lookup memories. The lookup memories provide both EM and hadronic transverse energies for each trigger tower above a fixed cut based on both electronic noise and physics considerations, and corrected for the z-vertex position, if known. The sum of the EM and hadronic transverse energy for each

trigger tower is formed and stored in a 9-bit register as an input for future hardware triggers. This sum is also used to form the x- and y-components of the transverse energy using lookup memories. Lookup memories also return the EM and hadronic transverse energies for each trigger tower, without any cut and z-correction. The full event missing transverse energy $\not{E}_T$, is formed from the x- and y-components of the global transverse energies. The global total transverse energies, both corrected and uncorrected, are formed from the corrected and uncorrected global EM and hadronic transverse energies respectively. These seven energy variables: global corrected EM E_T, global corrected hadronic E_T, global corrected total E_T, $\not{E}_T$, global uncorrected EM E_T, global uncorrected hadronic E_T, and global uncorrected total E_T, are each compared with up to 32 programmable thresholds. Each such comparison provides a Level 1 framework AND-OR input term.

3.3.3 Data Acquisition and Level 2 Trigger

The DØ data acquisition system and the Level 2 trigger hardware are intertwined. The data acquisition system consists of 50 parallel nodes connected to the detector electronics and triggers by a set of eight 32-bit wide high speed data cables. The function of the Level 2 system is to collect the digitized data from all relevant detector elements and trigger blocks for events that successfully pass the Level 1 triggers and to apply software algorithms on the data to reduce the rate from the approximately 100 Hz input to about 2 Hz output to the host computer and data logger. All the data for a specific event is sent over parallel paths to memory modules in a selected node. The event data is collected and formatted in final form in the node, and the Level 2 filter algorithms are executed.

The Level 2 software event-filtering process in each node is built as a series of filter tools. Each tool has a specific function related to identification of a type of particle or event characteristic. Among the tools are those for finding jets, muons, calorimeter EM clusters, track association with calorimeter clusters, or to make bet-

ter calculation of $\sum E_T$ and $\not{E}_T$. Other tools recognize specific noise or background conditions. A given event goes to a single L2 node where all the filters are defined by the current trigger menu. If any of the filters pass the event, the event is sent to the DØ Host computer where it is written to tape.

CHAPTER 4

EVENT RECONSTRUCTION AND PARTICLE IDENTIFICATION

The data written to the tape is not the final form of the event because the Level 2 does not consider the detailed information such as the full tracking or full shower shape. In addition, objects such as electrons, photons and jets are not well measured due to the restrictions on online cpu time and disk space. These tasks are done offline by the software package DØRECO. The function of DØRECO is to apply the calibration information to the raw data from each subsystem of the detector to generate corrected hits or energy depositions and apply various algorithms to the hits to find physical objects: electrons, photons, jets, $\not\!\!E_T$ and muons.

4.1 Vertex Determination

The primary interaction point for an event is called the vertex position with coordinates x, y, z. In DØRECO, vertex finding means the determination of the z-coordinate of the interaction point(s), i.e, along the beam line and the $x-y$ plane perpendicular to the beam. It is intended to provide precise information on the primary vertex position and the position of other vertices in the event if they exist.

4.1.1 Beam x-y Position

The (x,y) of the interaction position is stable in the x-y plane between runs and between stores. So the (x,y) position of the interaction point is determined outside DØRECO. The average x-y beam position for groups of runs has been included in DØRECO.

4.1.2 Interaction z Position

The determination of the interaction point in z is through the VERTEX package. The z position is primarily determined by tracks in the CDC. Full tracking for the CDC is done first. All CDC tracks which pass the impact parameter cut are extrapolated to the z axis and the intersection in z for each track is stored in a histogram. A cluster finding algorithm is used to determine the track clusters which have at least three tracks. The z position is the mean value for the intersection in z of all the tracks in one cluster. The z position from the cluster which has the most tracks is considered to be the primary vertex.

For a forward event, which has no activity in the central region, FDC full tracking is done and the vertex position is determined using FDC tracks. A similar procedure as used for the CDC is used to determine the vertex. Only one vertex is reconstructed using FDC tracks.

For events which have neither CDC nor FDC tracks, the vertex is determined by the hits in VTX chamber, where pairs of hits on the first and last wire in a VTX cell are connected and the line is extrapolated to the z axis. These lines are treated as VTX tracks and the vertex z positions are reconstructed using the same method as using the real tracks.

After the vertex z position is determined, a constrained fit is made to determine a more precise z vertex measurement. An overall fit is made to all the CDC (or FDC) tracks associated with an given vertex constraining them to originate from a single interaction point.

4.2 Electron Reconstruction and Identification

The electron reconstruction begins with finding all the electromagnetic (EM) clusters which contain several EM towers. The EM towers (0.2×0.2 in η-ϕ space) include the four layers of the EM calorimeter and the first layer of the fine hadronic

layer (FH1). These towers are ordered in descending energy. The highest energy tower is taken as a *seed*. The highest energy tower adjacent to this tower is added to the first tower. Then the second tower replaces the first tower as a *seed*. The highest energy tower adjacent to this *seed* (except the first seed) will be added to this cluster and so on. This procedure is called the nearest neighbor algorithm. This algorithm will continue until the neighboring highest energy tower is below the energy threshold of 0.05 GeV. This completes one EM cluster finding. New EM clusters are found if there are EM towers not included in the previously found clusters. After the clustering, clusters with total energy greater than 1.5 GeV are kept as electron candidates.

Because the EM calorimeters are typically 20 radiation lengths deep, most of the electromagnetic shower energy will be deposited in the EM calorimeters. For this reason, only those clusters which have at least 90% of their energy in the EM calorimeter are kept as the electron candidates. Since EM showers are narrow, only those clusters which have more than 40% of their energy deposited in the central tower are kept as electron candidates.

Electromagnetic shower profiles in the transverse direction (refer to the electron direction) are of exponential form. The centroid of the EM cluster is determined using energy log weighted mean of the cell positions in the third layer of the EM calorimeter where the η and ϕ segmentation is finer (0.05×0.05).

Electrons are charged particles which are expected to have a track in the central detectors pointing to the calorimeter cluster. Without a central magnetic field, tracks are straight lines. In order to find the tracks associated with the EM cluster, a road is defined as from the primary vertex to the center of the EM cluster. This road is $\pm$ 0.1 radians around the centroid in the ϕ direction. In the θ direction, the road size varies between ± 0.25 radians (for central candidates) and ± 0.1 radians (for forward candidates). Only clusters with at least one track in the road are kept

as electron candidates. Those clusters without a track inside the road are kept as photon candidates. If there are many tracks in a given road, the track that has the smallest distance between the calorimeter centroid position and the extrapolated track is chosen.

The requirement described above are the loose selection criteria for electron candidates. At this stage, most of the electron candidates are actually hadronic jets where a π° or η carries most of the jet energy and the associated tracks are due to soft charged pions or photon (γ) conversions within the jet. In order to further purify the electron candidate, sample information about the longitudinal and transverse profiles in the EM calorimeter, the charged particle ionization energy, and the tracks associated with the electron candidates are used to discriminate against π° and γ backgrounds. The variables used in this analysis are described below.

4.2.1 Electromagnetic Energy Fraction

Electromagnetic Energy Fraction f_{EM} is defined as the ratio of the cluster energy contained within the EM calorimeter and the cluster energy contained within the EM calorimeter and the first layer of the fine hadronic calorimeter (FH1):

$$f_{EM} = \frac{E_{EM}}{E_{EM} + E_{FH1}} \tag{4.1}$$

For electrons, at least 90% of the cluster energy must be contained within the EM calorimeter. Charged hadrons on average deposit less than 10% of their energy in the electromagnetic section of the calorimeter, making this a very powerful discrimination against the charged hadrons.

4.2.2 Cluster Isolation

The EM clusters must be isolated from other particles in the events. The isolation variable is defined as the ratio:

$$f_{iso} = \frac{E(0.4) - E_{EM}(0.2)}{E_{EM}(0.2)} \tag{4.2}$$

where $E(0.4)$ is the cluster energy contained in the four EM calorimeter layers and the first fine hadronic layer (FH1) within a cone of radius 0.4 in $\eta - \phi$ space, E_{EM} (0.2) is the cluster energy contained in the four EM calorimeter layers within a cone of radius 0.2.

4.2.3 Covariance Matrix X^2

The shower shape may be characterized by the fraction of the cluster energy deposited in each layer of the calorimeter. These fractions are dependent on the incident electron energy and are correlated, *i.e.* a shower which fluctuates and deposits a large fraction of its energy in the first layer will then deposit a smaller fraction in the subsequent layers and vice versa. To take into account both the energy observed in a given layer and its correlations with the energy deposited in the other layers, a covariance matrix (M) of 41 observables x_i to characterize the *electron-ness* of the shower is used. The matrix elements are computed from a reference sample of N Monte Carlo electrons with energies ranging between 10 and 150 GeV. They are defined as:

$$M_{ij} = \frac{1}{N} \sum_{n=1}^{N} \left(x_i^n - \bar{x}_i\right) \left(x_j^n - \bar{x}_j\right) \tag{4.3}$$

where x_i is the value of the ith observable for the nth electron and $\bar{x}_i$ is the mean of the ith observable. The observables are the fractional energies in layers EM1, EM2, EM4, the fractional energy in each cell of a 6×6 array of cells in EM3 centered on most energetic tower in the EM cluster, the logarithm of the total cluster energy, and the z position of the event vertex. A matrix is computed for each of the 37 towers into which half the calorimeter is subdivided in pseudo-rapidity. The other half of the calorimeter with negative z coordinate is handled using reflection symmetry. For a shower characterized by the observables x_i', the covariance parameter

$$X^2 = \sum_{i,j=1}^{41} \left(x_i' - \bar{x}_i\right) H_{ij} \left(x_j' - \bar{x}_j\right) \tag{4.4}$$

where $H = M^{-1}$, measures how consistent its shape is with that expected from an electromagnetic shower. In general, the values of the observables x_i are not normally distributed and therefore the covariance parameter X^2 does not follow a normal χ^2 probability distribution.

4.2.4 Cluster Track Match

After the determination of the shower centroid in the calorimeter, the reconstructed track found in the road is required to match the shower centroid. The track is extrapolated into the calorimeter and the significance S of the mismatch between the centroid and the extrapolated track is measured as:

$$S_{CC} = \sqrt{\left(\frac{\Delta\phi}{\delta_{\Delta\phi}}\right)^2 + \left(\frac{\Delta z}{\delta_{\Delta z}}\right)^2} \tag{4.5}$$

$$S_{EC} = \sqrt{\left(\frac{\Delta\phi}{\delta_{\Delta\phi}}\right)^2 + \left(\frac{\Delta r}{\delta_{\Delta r}}\right)^2} \tag{4.6}$$

where S_{CC}, S_{EC} are significance for CC and EC respectively, $\Delta\phi$ the azimuthal mismatch, Δz the mismatch along the beam direction, Δr the mismatch transverse to the beam, and δ_x is the resolution for observable x. An important source of background to electrons is photons from the decay of π° or η mesons which are copiously produced in $p\bar{p}$ collisions. This background can be reduced by requiring a small track match significance S.

4.2.5 Track Ionization

Charged particles will deposit energy in the tracking chambers due to ionization. By requiring that the distribution of ionization per unit length (dE/dx) for tracks associated with EM clusters is consistent with that of a minimum ionizing particle (MIP), the background from photon conversion can be reduced. Since the DØ detector has no central magnetic field, e^+e^- pairs from photon conversions in the material in front of the tracking chambers are not bent apart and often are reconstructed as

a single track. For an e^+e^- pair, the ionization in the tracking chambers is expected to be twice that of a single charged particle. So the backgrounds due to conversions can be reduced by rejecting tracks in a window of dE/dx around 2 MIPs.

4.2.6 Electron Likelihood Identification

According to previous DØ studies in Reference [37, 38, 39], at the same electron identification efficiency, a substantially better background rejection can be achieved if the conventional electron ID variables described above are combined to make a likelihood test. In this analysis, a four-variable (f_{EM}, X^2, track match significance S, and dE/dx) likelihood method is used to identify electrons. Using two simple hypotheses H, signal ($H = e$) and background ($H = b$), an EM cluster is considered to be an electron if it passes the test:

$$\Re(f_h) = \frac{p(x|b)}{p(x|e)} = \frac{f_h p(x|h) + (1 - f_h)p(x|ee)}{p(x|e)} < k \tag{4.7}$$

where x is an observable or a vector of observables and $p(x|H)$ is the probability density for x if the hypothesis H is true. Backgrounds to real electron arise mainly from two sources: charged hadrons that overlap with neutrons (h), and electron-positron pairs from photon conversions (ee). f_h is the fraction of hadron overlaps in the background and can be determined using methods described in Ref. [37].

To a good approximation, the four variables are independent of each other for electrons, photon conversions and hadron overlaps, and $p(x|H)$ can be factorized as:

$$p(x|H) = p_1(f_{EM}|H) \times p_2(X^2|H) \times p_3(S|H) \times p_4(dE/dx|H) \tag{4.8}$$

Figure 4.1 shows the comparison of the four-variables likelihood distribution for electron and non-electron objects. The electron sample is from $Z \rightarrow ee$ data. The non-electron sample is from multi-jet QCD data collected using the JET_3_MON trigger requirement.

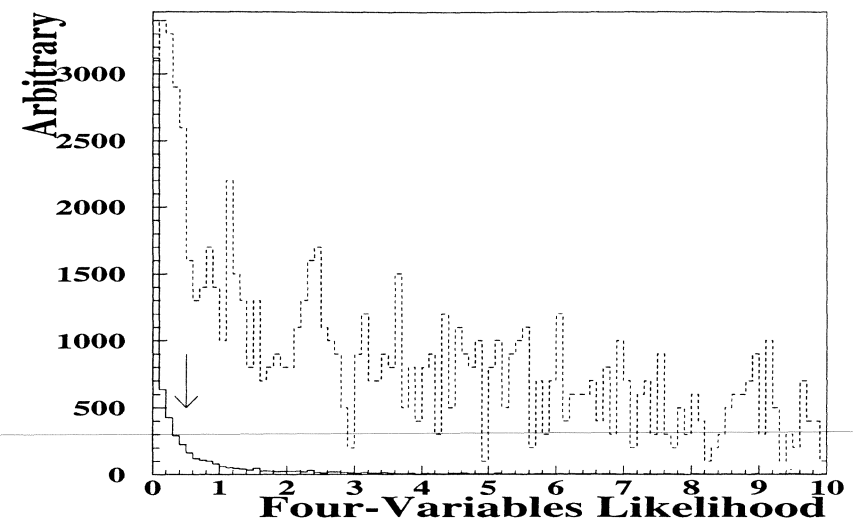

Figure 4.1: The comparison of four-variables likelihood distribution for electron and non-electron objects. The solid line corresponds to electron objects. The dashed line corresponds to non-electron objects. The arrow in the plot indicates the cut used in this analysis.

4.3 Jet Reconstruction

The DØ jet finding algorithm sums the E_T in a cone of radius $R = \sqrt{(\Delta\eta)^2 + (\Delta\phi)^2}$ to identify a jet. This search uses a fixed jet cone size of $R = 0.5$. Beginning with the highest E_T tower, preclusters are formed of contiguous cells out to a radius of about $R = 0.3$. Only towers with $E_T > 1$ GeV are included in preclusters. These preclusters become the starting point for jet finding and the precluster center is used as the initial cone center. A new E_T weighted center is then formed using the E_T of all towers within a radius $R \leq 0.5$ of the center. The process is repeated until the jet is stable. A jet must have $E_T > 8$ GeV. If two jets share energy, they will be merged together as one jet if the shared energy accounts for more than 50% of the energy of the lower E_T jet. Otherwise, they are split as two jets.

Table 4.1: Jet energy resolution fit parameters for each of the calorimeter regions.

η Region	Noise Term N (GeV)	Sampling Term $S(\sqrt{\text{GeV}})$	Constant Term (C)
$\lvert\eta\rvert < 0.5$	7.07 ± 0.09	0.81 ± 0.016	0.0 ± 0.005
$0.5\lvert\eta\rvert < 1.0$	6.92 ± 0.12	0.91 ± 0.019	0.0 ± 0.01
$1.0\lvert\eta\rvert < 1.5$	0.0 ± 1.4	1.45 ± 0.016	0.052 ± 0.006
$1.5\lvert\eta\rvert < 2.0$	8.15 ± 0.21	0.48 ± 0.07	0.0 ± 0.014
$2.0\lvert\eta\rvert < 3.0$	3.15 ± 2.5	1.64 ± 0.13	0.012 ± 0.58

By balancing the transverse energy from both dijet events and direct photon + jet events[1], the jet energy resolution can be obtained in different η regions by a parameterization using the following functional form:

$$\left(\frac{\sigma_E}{E}\right)^2 = \left(\frac{N}{E}\right)^2 + \left(\frac{S}{\sqrt{E}}\right)^2 + C^2 \tag{4.9}$$

where N, S, and C are the noise, sampling, and constant terms, respectively. Table 4.1 shows the fitted parameters for each of the calorimeter regions.

The final kinematic quantities for a jet are defined by

$$\begin{aligned} E_i &= \sum_{\text{towers } k} E_i^k \\ E_T &= \sum E_T^k \\ \phi &= \tan^{-1}(E_y/E_x) \\ \theta &= \cos^{-1}(E_z/\sqrt{E_x^2 + E_y^2 + E_z^2}) \\ \eta &= -\ln \tan(\theta/2) \end{aligned} \tag{4.10}$$

[1]Direct photon events are defined as those events which photon comes from the hard-scattering directly.

where E_i represents the four components of the momentum four vector. E_T is the sum of the individual tower transverse energies, not the magnitude of the vector components, η and ϕ are defined with respect to the interaction vertex which is not always at z =0.

4.4 Missing E_T ($\not{E}_T$) Measurement

The calculation of missing transverse energy $\not{E}_T$ at DØ is based upon energy deposits considered at the level of individual cells:

$$\begin{aligned}
\not{E}_x &= -\sum_{\text{cell } i} E_{xi} \\
\not{E}_y &= -\sum_{\text{cell } i} E_{yi} \\
\vec{\not{E}}_T &= \begin{bmatrix} \not{E}_x \\ \not{E}_y \end{bmatrix} \\
\not{E}_T &= \sqrt{\not{E}_x^2 + \not{E}_y^2} \\
\phi_{\not{E}_T} &= \tan^{-1}(\not{E}_y / \not{E}_x)
\end{aligned} \tag{4.11}$$

where E_{xi} and E_{yi} are the x- and y- component of energy for cell i respectively. The sums are over all cells in the calorimeter.

4.5 Energy Scale Correction

The DØ detector absolute energy scale is determined by the EM calorimeter. By requiring the two electron invariant mass of inclusive dielectron events in the mass region be equal to the Z boson mass measured at LEP [42], the energy scale for EM objects is obtained. If the two electrons are in the same calorimeter cryostates, an independent absolute scale factor for each cryostat is obtained. The process $\pi^\circ \rightarrow \gamma\gamma$ and $J/\psi \rightarrow ee$ were studied to check the calibration at different energies.

The effects which contribute to uncertainties in the jet energy response include non-linearities in the calorimeter response to hadrons, non-uniformities of the calorimeter, contributions from the uranium noise, and residual energy of the hard scattering (underlying event). The correction for the jet energy response includes: correction for the proper energy scale in the central region, out-of-cone showering correction, η and EMF dependence correction, underlying event and uranium noise correction.

To determine the jet energy scale for the central region, DØ used the methods described in Ref. [44] to measure the cumulative response of the calorimeter to the fragmentation products associated with a jet, the so-called Missing Transverse Energy Projection Fraction (MPF) technique. DØ used a set of data containing a 'photon' and one or more jets. The 'photon' was defined as an electromagnetic cluster (EMF ≥ 0.90) with no associated track. The imbalance along the direction of the photon in the transverse plane was attributed to the mismeasurement of the hadronic jet. MPF is then defined as

$$MPF = \frac{-\hat{n} \cdot \vec{\not{E}}_T}{E_T^\gamma} \tag{4.12}$$

where $\hat{n}$ is the unit vector along the direction of the photon, E_T^γ is the corrected transverse energy of the photon, and $\vec{\not{E}}_T$ is the measured missing transverse energy of the event. Then the calorimeter response to the jet R_j is:

$$R_j = 1 - MPF \tag{4.13}$$

Thus, the response of the calorimeter to the hadronic jet is measured relative to the known response to the EM cluster.

DØ uses the fixed cone algorithm for jet finding. Due to fragmentation, the final state parton shower may be wider in the calorimeter. Some of the energy may fall out side of the cone. To measure this out-of-cone effect, DØ has substituted single

particle test-beam showers for fragmentation products in the Monte Carlo event generators [40]. The energy deposited outside of the jet cone due to showering was corrected.

After the corrections described above for jets in the central calorimeter, the η-dependence of the jet scale is determined using dijet events. One jet is required to be central ($|\eta| \leq 0.7$). The η of the other jet is allowed to be any value. By requiring that the two jets balance each other in the transverse plane, the correction for the energy and E_T of forward jets can be obtained. If one jet is required to be central ($|\eta| \leq 0.7$) and the EMF of the other jet is allowed to be any value, the correction of the EMF-dependence of the jet can be obtained by requiring the dijet balance.

Because the energy flow of the underlying event is independent of (approximately) that of the hard scatter, the correction for underlying event energy can be determined by measuring the energy density in minimum bias events and then subtracting that energy density from the jet energy. The energy in the jet due to uranium noise was estimated by considering data taken without zero suppression.

The cumulative correction from all of these effects is shown in Fig. 4.2 [41]. The curve in the figure shows the mean value of the jet E_T corrections. For central jets with E_T above 20 GeV, the correction is typically 15% [41]. The correction generally increase with η as out-of-cone losses increase, while it decreases at the very lowest jet E_T due to lower energy. The error band for the jet E_T corrections is calculated as [43]:

$$E_T(+1\sigma) = 4\% \cdot E_T + 1 \text{ GeV} \tag{4.14}$$

$$E_T(-1\sigma) = -4\% \cdot E_T - 1 \text{ GeV} \tag{4.15}$$

where E_T is the corrected jet transverse energy.

After the electron, photon and jet energy corrections, the $\not\!\!E_T$ of the event is corrected:

$$\not\!\!E_{Tx} = \not\!\!E_{Tx}^{uncor} - \sum_j \Delta E_x^j \tag{4.16}$$

$$\not\!\!E_{Ty} = \not\!\!E_{Ty}^{uncor} - \sum_j \Delta E_y^j \tag{4.17}$$

where $\not\!\!E_{Tx}^{uncor}$, $\not\!\!E_{Ty}^{uncor}$ are the uncorrected $\not\!\!E_T$ component in the x, y directions. The sum is over the corrections in E_T applied to all electrons, photons and jets in the event.

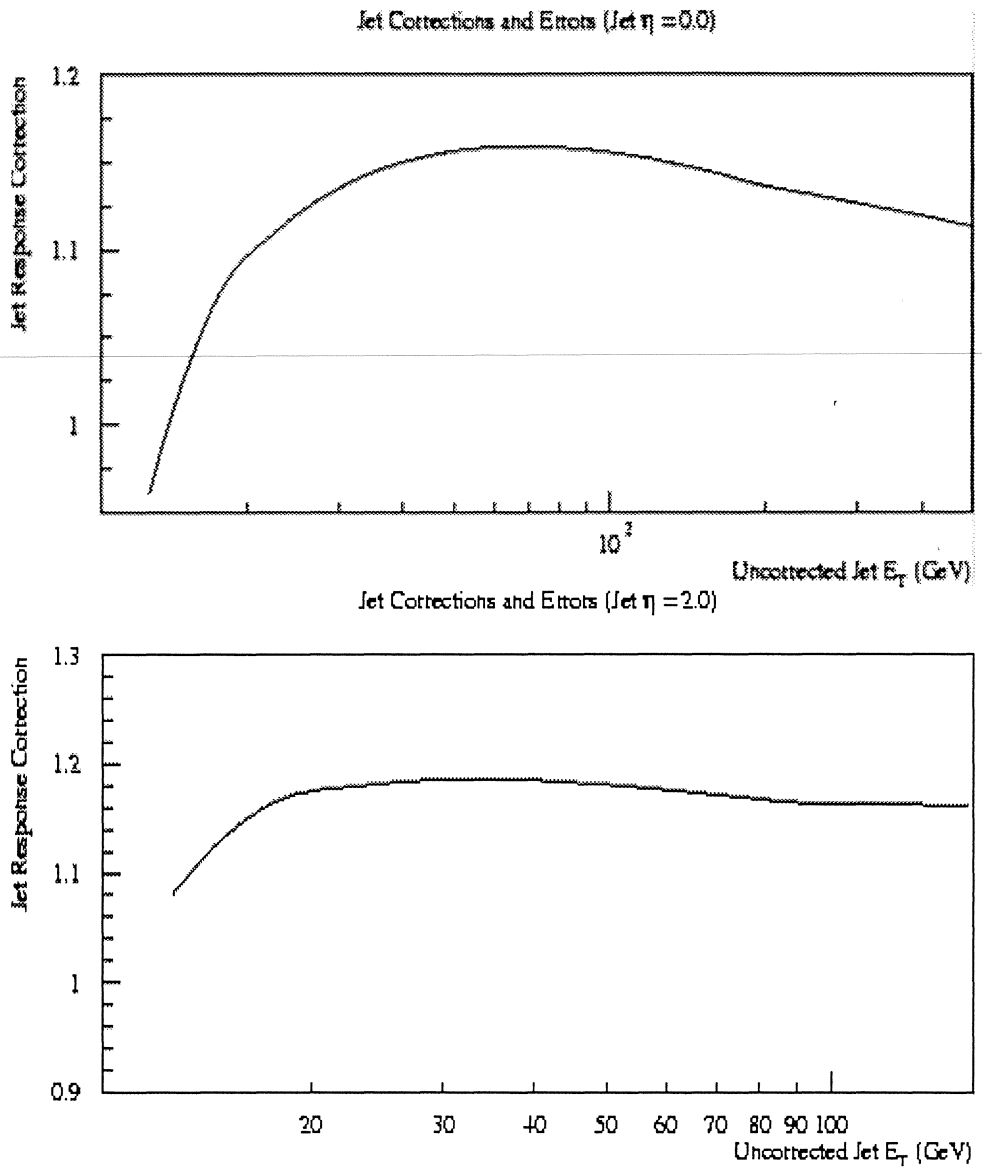

Figure 4.2: The cumulative energy correction for jets. The upper plot shows the energy correction for jets with $\eta = 0$. The lower plot shows the energy correction for jets with $\eta = 2.0$.

CHAPTER 5

ANALYSIS

As described in Section 2.4, first generation scalar leptoquarks couple only to first generation leptons and quarks. The final states for the leptoquark pair production would be $eeqq$, $e\nu qq$ or $\nu\nu qq$. Quarks will hadronize in the detector and form a jet. Neutrinos will escape the DØ detector and are a source of missing energy. So the signatures of first generation scalar leptoquark pair production at the Tevatron are: 2 e + 2 jets ($eejj$), 1e + 2 jets + $\not\!\!E_T$ ($e\nu jj$) and 2 jets + $\not\!\!E_T$ ($\nu\nu qq$). In this thesis, the 2 jets + $\not\!\!E_T$ channel is not investigated[1].

In this chapter, Section 5.1 describes the event selection criteria in the $eejj$ channel and the search result. Section 5.2 describes the event selection criteria in the $e\nu jj$ channel and the search result. Section 5.3 describes the combination of the results from the two channels.

5.1 $eejj$ Channel

There are many processes which produce the signature of $eejj$ other than first generation scalar leptoquark pair production. These kind of processes are called *physicsbackgrounds*. Another source of background which mimics the leptoquark signature is the mismeasurement or instrumental background. The backgrounds will be described in detail in Section 5.1.2.

[1]For the 2 jets + $\not\!\!E_T$ channel, the major background is QCD multijets events with one or more jet energy mismeasured. Because of the large cross section of QCD multijets events (several hundred μb), the QCD mismeasurement background is large.

The analysis strategy is to choose selection criteria (called *cuts*) which will separate the signal from the backgrounds. In reality, we cannot identify each event as a signal event or a background event due to statistical fluctuation. So, we cannot select a signal sample without background contamination. However, we can optimize the selection criteria to keep as many of the signal events as possible and to reject most of the background events. These optimized *cuts* can be obtained by comparing characteristics of the leptoquark signal events' signature with that of the background events' signature. To know the characteristics of the signal events and background events, we use Monte Carlo (MC) simulation to simulate the leptoquark signal events and physics background events. Mismeasurement background can be estimated from the collider data. In what follows, *signal events* refers to signal MC events. *Background events* refers to background MC events for the physics backgrounds and multi-jet collider data for the mismeasurement background. The fraction of signal events passing the cuts is called the signal efficiency.

5.1.1 Signal Simulation

Leptoquark pair production at the Tevatron was simulated using the event generator ISAJET v7.13 and v7.22 [45] for eleven leptoquark masses: M_{LQ} =60, 80, 100, 120, 140, 160, 180, 200, 220, 240 and 260 GeV/c^2. For each leptoquark mass, 2000 or 5000 events were generated. No generator level cuts were applied. Detector response was simulated using GEANT v3.14, v3.15 [46] and trigger simulation (L2PROD v7.08 [46]). Finally, the MC events were reconstructed using DØRECO v12.20 and v12.21 [46]. Table 5.1 shows a summary of the leptoquark MC events.

5.1.2 Backgrounds

As described above, the backgrounds for the $eejj$ channel include both physics backgrounds and mismeasurement background.

Table 5.1: The status of the leptoquark pair production MC events.

M_{LQ} (GeV/c^2)	No. of events	Generator	GEANT version	RECO version
60	2000	ISAJET 7.13	v3.14	v12.20
80	2000	ISAJET 7.13	v3.14	v12.20
100	2000	ISAJET 7.13	v3.14	v12.20
120	2000	ISAJET 7.13	v3.14	v12.20
140	2000	ISAJET 7.13	v3.14	v12.20
160	2000	ISAJET 7.13	v3.14	v12.20
180	2000	ISAJET 7.13	v3.14	v12.20
200	2000	ISAJET 7.13	v3.14	v12.20
220	5000	ISAJET 7.22	v3.15	v12.21
240	5000	ISAJET 7.22	v3.15	v12.21
260	5000	ISAJET 7.22	v3.15	v12.21

Physics Backgrounds. Physics backgrounds are those physics processes whose final states have at least two electrons and two quarks/gluons. Quarks/gluons are reconstructed as jets. The most important physics backgrounds are: $Z, \gamma^* \rightarrow ee$ production in conjunction with jets (Z+jets), $t\bar{t}$ production with both W bosons decaying into e and ν_e; $Z \rightarrow \tau\tau$ with both τ decays into e and ν_e, and WW production in conjunction with jets and both W bosons decaying into e and ν_e. Because we don't have sufficient collider data to estimate the physics backgrounds, we use MC simulation. Table 5.2 shows a summary of the physics backgrounds MC events. Details are given below.

$Drell - Yan$: For the Z, γ^* + jets background, four MC event sets were produced with different Z, γ^* masses due to the strong M_{ee} dependence of the cross

Table 5.2: Summary of the physics backgrounds MC events. The detailed information is addressed in the text.

Process	Cross section (pb)	No. of events	Generator	GEANT version	RECO version	Remark
$t\bar{t} \to ll$	0.395	101339	HERWIG v5.7	v3.15	v12.21	top mass 170 GeV/c^2
$Z \to \tau\tau \to ll$	644.0	28,691	PYTHIA v5.60	v3.14	v12.20	Z boson p_T >25 GeV/c
$WW \to ee$	0.11	9,034	ISAJET v7.08	v3.14	v12.15	2e E_T >10 GeV 2 pjets E_T > 5 GeV
$Z, \gamma^* \to ee$		20,000	ISAJET v7.13	v3.14	v12.20	Z, γ^* mass range
	145.4	460,000	ISAJET v7.22	v3.15	v12.21	20–60 GeVc^2
$Z, \gamma^* \to ee$		10,000	ISAJET v7.13	v3.14	v12.20	Z, γ^* mass range
	201.9	480,000	ISAJET v7.22	v3.15	v12.21	60–120 GeV/c^2
$Z, \gamma^* \to ee$		10,000	ISAJET v7.13	v3.14	v12.20	Z, γ^* mass range
	2.13	40,000	ISAJET v7.22	v3.15	v12.21	120–250 GeV/c^2
$Z, \gamma^* \to ee$	0.112	10,000	ISAJET v7.13	v3.14	v12.20	Z, γ^* mass range 250–500 GeV/c^2

section. The four MC event sets correspond to the M_{ee} mass ranges 20–60 GeV/c^2, 60–120 GeV/c^2, 120–250 GeV/c^2, and 250–500 GeV/c^2. The Z, γ^* mass range 0–20 GeV/c^2 was ignored because the final state electrons would be softer than our offline 25 GeV E_T cut (discussed below). Also, the Z, γ^* mass range 500 GeV/c^2 and above was ignored because the cross section is very small (about 0.0032 pb), and we would not get many events even if the total efficiency was 100%. The ISAJET v7.13 and v7.22 event generator was used to produce the events and showerlibrary (v3.14 and v3.15) was used to simulate the DØ detector. Figure 5.1 shows the dielectron invariant mass distribution of the four MC sets.

$t\bar{t}$: For the $t\bar{t}$ background, events were generated using HERWIG v5.7 generator, followed by showerlibrary and trigger simulation. After the $t\bar{t}$ pair was produced, both top quarks decay into a b quark and a W boson, followed by W boson was forced to decay into $e\nu_e$, $\mu\nu_\mu$ or $\tau\nu_\tau$. So these MC events contain the contribution of tau decays into electrons: $W \to \tau\nu_\tau \to e\nu_e\nu_\tau\nu_\tau$. The top quark mass is assumed

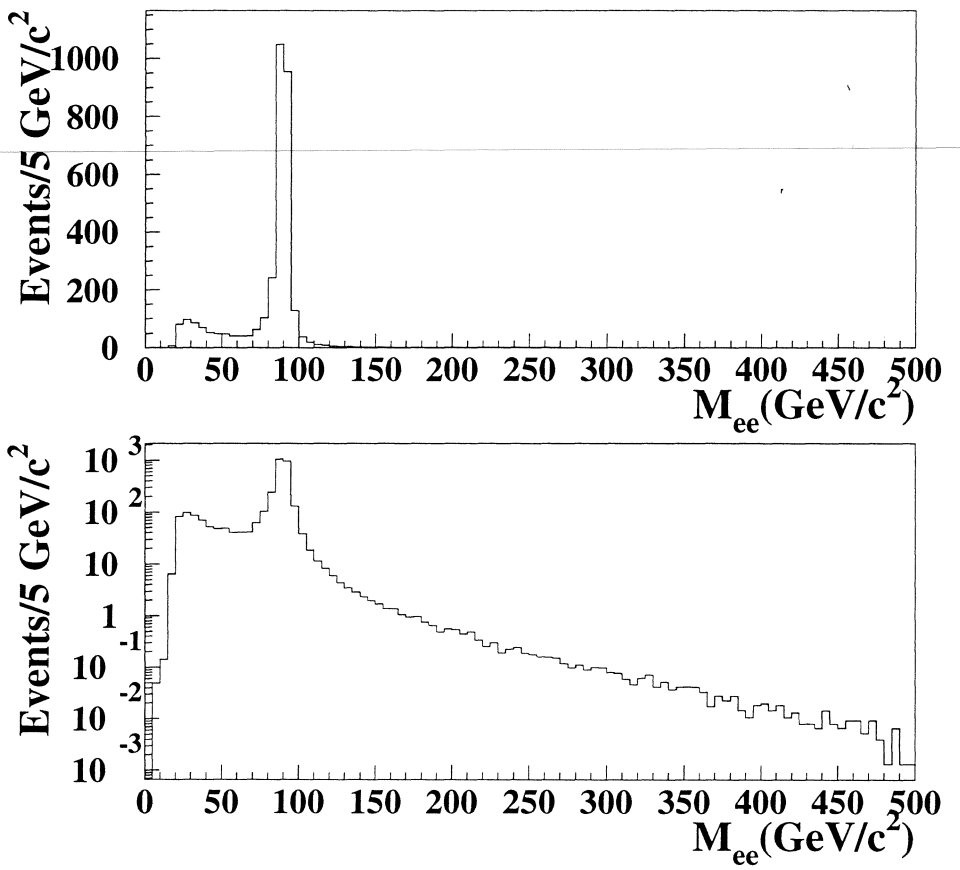

Figure 5.1: The invariant mass distribution for the Drell-Yan MC sample. The upper figure is linear scale while the lower figure is logarithmic scale.

to be 170 GeV/c^2. These MC events were produced by the DØ top group and there were no generator level cuts.

$Z \rightarrow \tau\tau$: For the $Z \rightarrow \tau\tau \rightarrow ll$ background, events were generated using PYTHIA v5.60, followed by showerlibrary and trigger simulation. In order to enhance the Z+jets–like topology, Z boson $p_T > 25$ GeV/c was required at the generator level. These MC events were produced by the DØ top group and there were no generator level cuts.

WW : For the $WW \rightarrow ee$ background, events were generated using ISAJET v7.08, followed by showerlibrary and trigger simulation. After the WW production, each W boson was forced to decay into an electron and a neutrino. The events were produced by the DØ top group.

Mismeasurement Background. The mismeasurement background is mainly from QCD multijet production. For QCD events with four or more jets, if two of the jets are misidentified as electrons, the events can pass the offline cuts. Although the probability of two jets being misidentified as two electrons is very small (on the order of 10^{-8}, see Section 5.1.6), this background can not be ignored due to the large QCD cross section.

5.1.3 Distributions of Physics Variables for MC Signal and MC Backgrounds

The E_T distributions of the two leading electrons for the MC signal and background samples are shown in Figure 5.2. The events are normalized to the same luminosity for the signal events and background events and then scaled for display. The numbers on the plots for each process show the scaling for that process. One electron with $E_T > 10$ GeV has been required for the leading electron E_T distribution. Two electrons with $E_T > 10$ GeV has been required for the second leading electron E_T distribution. One jet was required for the leading jet E_T distribution

after two electrons with $E_T > 10$ GeV have been required and excluded from jets. Two jet were required for the second leading jet E_T distribution after two electrons with $E_T > 10$ GeV have been required and excluded from jets. The arrow in each plot shows the offline cuts which are discussed in the following section.

Figure 5.3 shows the electron and jet invariant mass distribution after the events passed the following kinematic cuts: two electrons with $E_T > 15$ GeV and two jets with $E_T > 20$ GeV. Each event was plotted twice (both ej mass combinations for an event were included in the plots). The four combination of the ej invariant mass (M_{e1j1}, M_{e2j2}, M_{e1j2} and M_{e2j1}) were calculated along with the difference between M_{e1j1} and M_{e2j2}, M_{e1j2} and M_{e2j1}. The invariant masses with the smaller mass difference were selected to make the plot. The invariant mass of the electron and jet peaks near the input leptoquark mass, with the broadening of the peak due mostly to jet energy resolution and initial and final state gluon radiation.

Figure 5.4 shows the invariant mass distribution of the dielectron pair of the leptoquark events and four physics backgrounds after two electrons with $E_T > 10$ GeV were imposed. The $Z, \gamma^* \rightarrow ee$ sample in Figure 5.4 (c) is from the MC events of mass range 60–120 GeV/c^2. The dielectron mass distribution for the leptoquark events was broad and flat, but the dielectron mass distribution for the $Z, \gamma^* \rightarrow ee$ events peaks around 90 GeV/c^2 as expected. A Z boson mass window cut is very efficient in reducing the $Z, \gamma^* \rightarrow ee$ background.

5.1.4 Offline Events Selection Criteria

The criteria to choose the offline electrons and jets kinematic cuts is to retain the greatest number of signal events while rejecting the greatest amount of background. At this first step, the electron identification efficiency is assumed to be 100%. Then 120, 140 and 160 GeV/c^2 leptoquark MC samples were used and the significances s/b and $s/\sqrt{b}$ (where s is the expected number of leptoquark events and b is the total expected background) were calculated for $E_T^e \geq 20$, 25, 30 GeV and $E_T^j \geq 15$, 20,

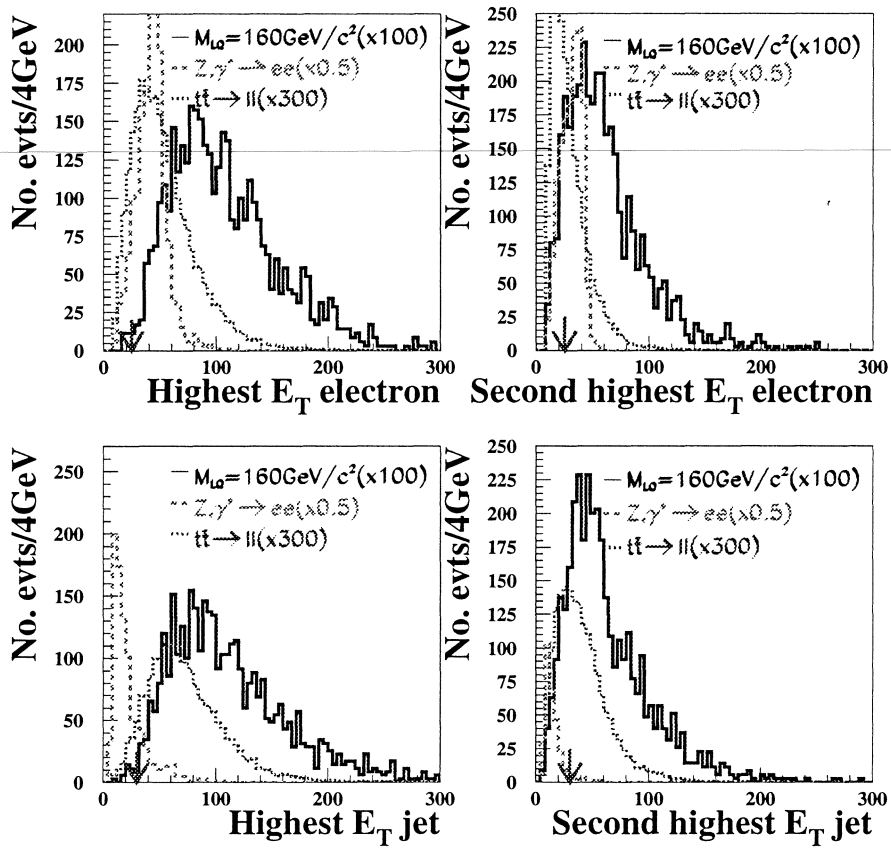

Figure 5.2: The E_T distribution of the leading two electrons and leading two jets of the MC signal and major background events. The explanation of this plot is in the text.

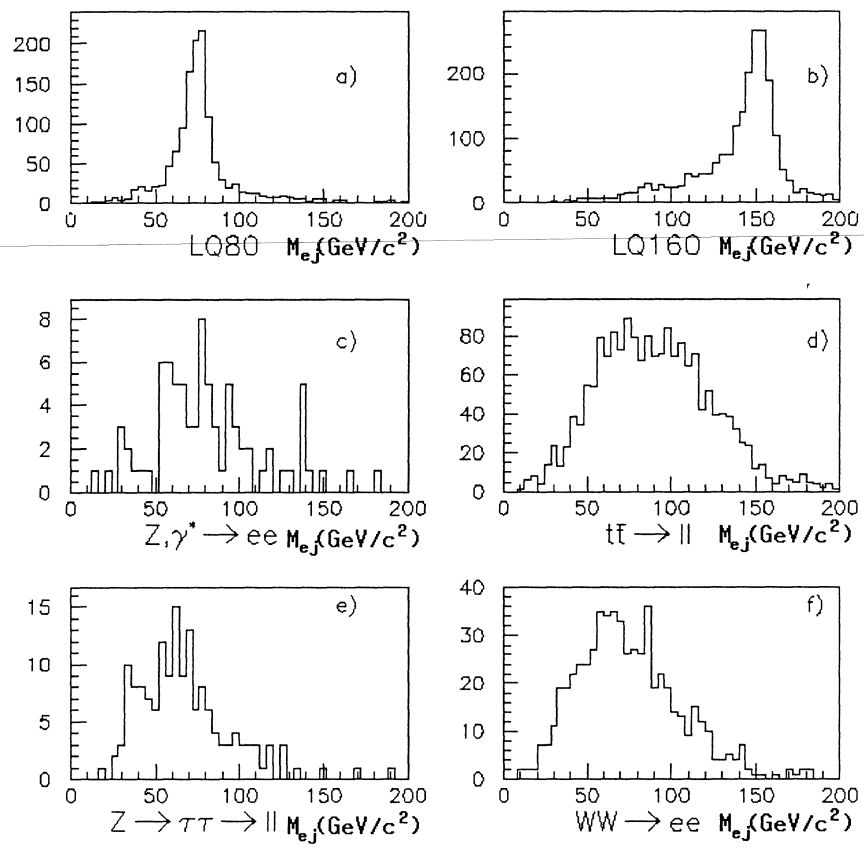

Figure 5.3: The one electron and one jet invariant mass distribution for the MC signal and background events. a and b are MC signal events with leptoquark mass M_{LQ} = 80 GeV/c^2 and 160 GeV/c^2, respectively. The ej invariant mass peaks around the input leptoquark mass. c, d, e and f are backgrounds from $Z, \gamma^* \rightarrow ee$ ($60 < M_{ee} < 120$ GeV/c^2), $t\bar{t} \rightarrow ll$, $Z \rightarrow \tau\tau \rightarrow ll$ and $WW \rightarrow ee$ respectively. Note that two electrons with $E_T > 15$ GeV and two jets with $E_T > 20$ GeV were required. Both ej mass combinations for each event were included in the plots. The explanation of these plots is in the text.

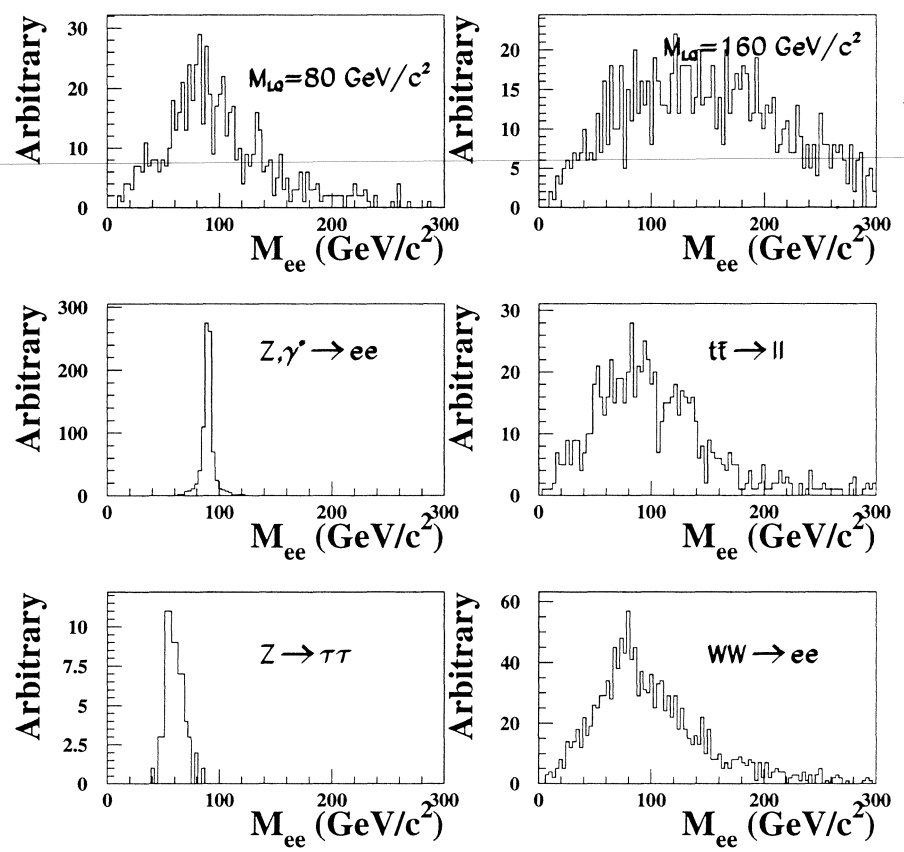

Figure 5.4: The invariant mass distribution of the dielectron from the MC signal and major background events. Two electrons with $E_T > 10$ GeV were required. The explanation of these plots are in the text.

25, 30, 35. The result is shown in Table 5.3. From Table 5.3, if two electrons with $E_T \geq 25$ GeV and two or more jets with $E_T \geq 30$ GeV are required, the maximum of $s/\sqrt{b}$ for $M_{LQ} = 120$, 140 and 160 GeV/c^2 can be obtained. So for the offline kinematic cuts, we require two or more electrons with $E_T \geq 25$ GeV and two or more jets with $E_T \geq 30$ GeV.

After the two electrons and two jets requirement, the remaining events are mostly from $Z, \gamma^* + 2$ jets events. This background can be reduced dramatically by rejecting the events for which the two-electron invariant mass falls in 76 GeV/$c^2 < M_{ee} <$ 106 GeV/c^2. The efficiency of this cut is shown in Table 5.4.

None of the above cuts makes explicit use of the fact that for the "correct" ej pair which comes from a leptoquark decay, the invariant mass M_{ej} would be equal to the actual LQ mass. Reconstructing LQ masses based on the observed ej masses has been shown to give considerable background rejection while affecting signal acceptance only slightly. In this $eejj$ channel, all decay products of both LQ's are visible. This analysis uses the two electrons and two leading jets to calculate the ej pair mass (the leading electron $e1$, second leading electron $e2$, leading jet $j1$ and second leading jet $j2$). The masses of the four possible ej pairs ($e1j1$, $e2j2$, $e1j2$ and $e2j1$) are computed. Because each event is hypothesized to contain two leptoquarks, the ej pairs are further grouped into two pairs ($e1j1$ and $e2j2$ vs. $e1j2$ and $e2j1$)[2] and the mass differences are computed. The assignment which gives the smallest mass difference is then retained for the remainder of the analysis as the most likely to satisfy the leptoquark model. Here one variable is defined as:

$$\delta M_{LQ} \equiv \frac{\sqrt{(M_1 - M_{LQ})^2 + (M_2 - M_{LQ})^2}}{M_{LQ}} \tag{5.1}$$

where M_1 and M_2 are reconstructed masses of the two ej pairs, and M_{LQ} is the hypothesized LQ mass. Figure 5.5 shows the distribution of δM for the total back-

[2]Each jet and electron is required to be used once and only once within the two leptoquark mass pairings.

grounds and LQ MC signal events. A requirement of $\delta M \leq 0.3$ was found to be optimal for high mass LQ events to further increase the signal over background ratio.

5.1.5 Data Selection

Data used in this analysis were taken during Run Ia (stream RUN1A_LQ_2EM_TIGHT), Run Ib (stream RUN1B_LQ_2EM_TIGHT) and Run Ic (stream RUN1C_LQ_2EM_TIGHT). After excluding bad runs[3], the data sample represents a total integrated luminosity of $L = 117.7 \pm 6.4$ pb^{-1}. The uncertainty is the systematic uncertainty (5.4%) determined by the luminosity group [47].

Before applying the offline cuts, the energies of the electrons, photons and jets were corrected using the CAFIX 5.0 package [41]. The main corrections are a scale factor applied to the electromagnetic energy response (that brings the Z boson mass peak to the LEP measured value) and a correction to the hadronic energy response (that balances the transverse energy of hadronic jets recoiling against highly electromagnetic jets). The energy correction is described in detail in Section 4.5.

A sample of events with two or more isolated electron candidates is first selected. Then the kinematic cuts are imposed on the electrons followed by the requirement of two or more high transverse energy jets. The remaining events are mostly from the Z, γ^* + jets. Finally the Z boson mass window cut (invariant mass of the two electrons) is imposed to reduce most of the Z, γ^* + jets background.

L1 and L2 Triggers. Events from Run Ia had to pass a hardware level trigger (L1 trigger) EM_2_MED requiring at least 2 electromagnetic objects with transverse energy $E_T > 7$ GeV. Events from Run Ib and Ic had to pass the L1 trig-

[3]Bad runs are defined as those data runs when detector is not working properly during the data collecting.

Table 5.3: s/b and $s/\sqrt{b}$ for different offline selections.

M_{LQ}(GeV/c^2)	120		140		160	
	s/b	$s/\sqrt{b}$	s/b	$s/\sqrt{b}$	s/b	$s/\sqrt{b}$
2 E_T^e >20, 2 E_T^j >15 GeV	0.81	10.39	0.40	5.09	0.20	2.59
2 E_T^e >20, 2 E_T^j >20 GeV	1.55	13.90	0.77	6.89	0.40	3.58
2 E_T^e >20, 2 E_T^j >25 GeV	2.54	17.10	1.26	8.49	0.67	4.53
2 E_T^e >20, 2 E_T^j >30 GeV	3.82	19.78	1.91	9.87	1.07	5.55
2 E_T^e >20, 2 E_T^j >35 GeV	4.81	20.58	2.52	10.78	1.44	6.18
2 E_T^e >25, 2 E_T^j >15 GeV	1.02	11.08	0.52	5.59	0.26	2.87
2 E_T^e >25, 2 E_T^j >20 GeV	2.07	15.27	1.06	7.77	0.55	4.08
2 E_T^e >25, 2 E_T^j >25 GeV	3.25	18.31	1.66	9.36	0.89	5.03
2 E_T^e >25, 2 E_T^j >30 GeV	5.93	23.36	3.04	11.96	1.73	6.82
2 E_T^e >25, 2 E_T^j >35 GeV	5.99	21.66	3.24	11.71	1.88	6.82
2 E_T^e >30, 2 E_T^j >15 GeV	1.13	10.98	0.58	5.67	0.31	2.98
2 E_T^e >30, 2 E_T^j >20 GeV	2.07	14.34	1.08	7.50	0.58	4.04
2 E_T^e >30, 2 E_T^j >25 GeV	2.96	16.39	1.56	8.64	0.86	4.77
2 E_T^e >30, 2 E_T^j >30 GeV	5.53	21.01	2.94	11.18	1.73	6.55
2 E_T^e >30, 2 E_T^j >35 GeV	5.64	19.56	3.17	10.99	1.89	6.56

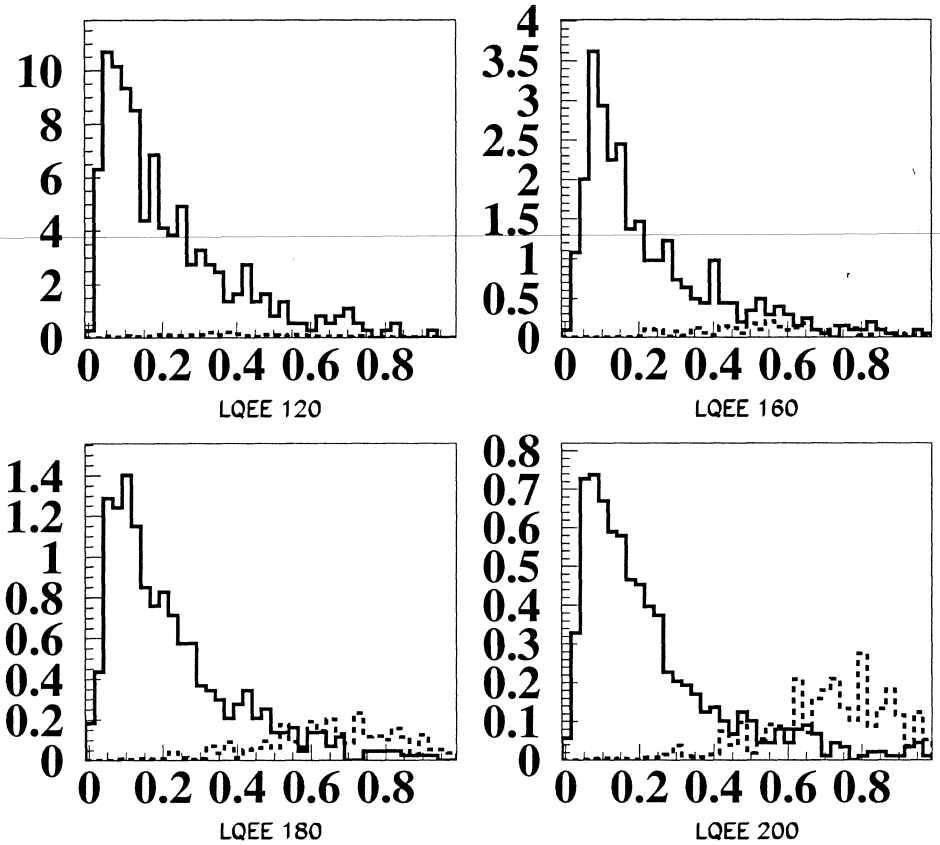

Figure 5.5: The distributions of δM for signal and background for four different LQ masses. The vertical axis is the number of events. The solid lines in the plots are the δM distributions of the signal events, and the dashed lines in the plots are the δM distributions of the total backgrounds. All the offline cuts were applied except the δM requirement.

Table 5.4: Selection of the Z boson mass window cuts.

Cuts	Signal (M_{LQ} = 40 – 260 GeV/c^2) Acceptance (%)	Z, γ^* + jets Rejection (%)
$\lvert M_{ee} - M_Z \rvert > 10$ GeV/c^2	83 – 96	41
$\lvert M_{ee} - M_Z \rvert > 15$ GeV/c^2	75 – 93	83
$\lvert M_{ee} - M_Z \rvert > 20$ GeV/c^2	58 – 91	83

ger EM_2_MED requiring at least 2 electromagnetic towers with transverse energy $E_T > 7$ GeV and at least 1 hadronic plus EM trigger tower with $E_T > 3$ GeV.

In addition to the L1 trigger requirement, events from Run Ia passing ELE_2_HIGH had to pass the online software filter (L2) requiring two or more electromagnetic clusters with $E_T > 10$ GeV, with electron longitudinal and transverse shape requirements; one of the clusters was also required to be isolated from other energy deposits in the event. Events from Run Ib passing EM2_EIS_EIS had to pass a L2 trigger requiring one or more electromagnetic clusters with $E_T > 20$ GeV, with electron shape and isolation requirements and two or more electromagnetic clusters with $E_T > 16$ GeV, with electron shape and isolation requirements. Events from Run Ic passing EM2_EIS2_HI had to pass a L2 trigger requiring two or more electromagnetic clusters with $E_T > 20$ GeV, with electron shape and isolation requirements. Table 5.5 shows the triggers and the corresponding luminosities.

Offline Selection. After the candidate events pass the trigger requirements, they must satisfy the following requirements:

- Electrons:

  Two good electrons, with $E_T > 25$ GeV and in a fiducial region defined as $|\eta| < 2.5$ are required for the events. At least one electron must be in the

Table 5.5: Triggers used in the $eejj$ channel.

	L2 trigger name	Luminosity (pb^{-1})
Run Ia	ELE_2_HIGH	13.7
Run Ib	EM2_EIS_EIS	93.7
Run Ic	EM2_EIS2_HI	10.3
Run I (total)	-	117.7

Central Calorimeter (CC) region, defined as $|\eta_{det}| < 1.2$. A good electron is an energy cluster which passes the following quality 4.2 cuts:

* $f_{EM} > 0.9$
* four-variables likelihood $\Re \leq 0.5$
* cluster isolation $f_{iso} \leq 0.1$

- Jets:

  Two jets with $E_T > 30$ GeV in a fiducial region $|\eta| < 2.5$ must be found in the events. Because electrons are also identified as jets, the jets have to be separated from the electrons in $\eta - \varphi$ space: $\delta R(e,j) = \sqrt{(\Delta\eta)^2 + (\Delta\varphi)^2} > 0.25$.

- Z boson mass cut:

  After the two electron and two jet cuts, the remaining events are mostly from $Z, \gamma^* + 2$ jets events. This background can be reduced dramatically by rejecting the events for which the two electron invariant mass falls in 76 GeV/$c^2 < M_{ee} <$ 106 GeV/c^2.

  Figure 5.6 shows the E_T distributions of the electrons and jets, as well as the M_{ee}, M_{ej} distributions after the trigger requirement for Run Ib data. The

arrows in the plots indicate the offline kinematic cuts. For the M_{ej} plots, both combinations of ej mass for each event were included in the plots. Table 5.6 shows the number of events passing the imposed offline cuts. Figure 5.7 shows the two electron invariant mass distribution for Run I data and the total backgrounds requiring two electrons with $E_T > 25$ GeV and two jets with $E_T > 15$ GeV. Figure 5.8 shows the two electron invariant mass distribution for Run I data and the total background requiring two electrons with $E_T > 25$ GeV and two jets with $E_T > 30$ GeV. Both plots have a nice Z boson mass peak for collider data and background events. This indicates that the major background is from Drell-Yan process after the imposed cuts. There are three events (run 84870 event 29117, run 90278 event 31411, and run 92263 event 14233) outside the Z boson mass window. Detailed information about these three events is given in Table 5.7.

- LQ mass window cuts:

  After requiring $\delta M \leq 0.3$ as described in Section 5.1.4, none of the three events survive at LQ mass points 60, 100, 120, 140, 160, 200, 220, 240, 260 GeV/c^2. Event – run 92263 event 14233 – survives at LQ mass point 80 GeV/c^2. Event – run 84870 event 29117 – survives at LQ mass point 180 GeV/c^2. Because the LQ MC events were simulated at the step of 20 GeV/c^2 of the LQ masses, the fact that a candidate event survives at a simulated LQ mass point does not mean that the candidate event only survives at the LQ mass point. If the LQ MC events were simulated at a smaller step of the LQ masses, the candidate event may be survive at several LQ mass point. To find out the boundary of LQ masses inside which the candidate event survives, Equation 5.1 can be used. Put the information of the candidate event into Equation 5.1:

$$\delta M_{LQ} \equiv \frac{\sqrt{(M_1 - M_{LQ})^2 + (M_2 - M_{LQ})^2}}{M_{LQ}} = 0.3 \tag{5.2}$$

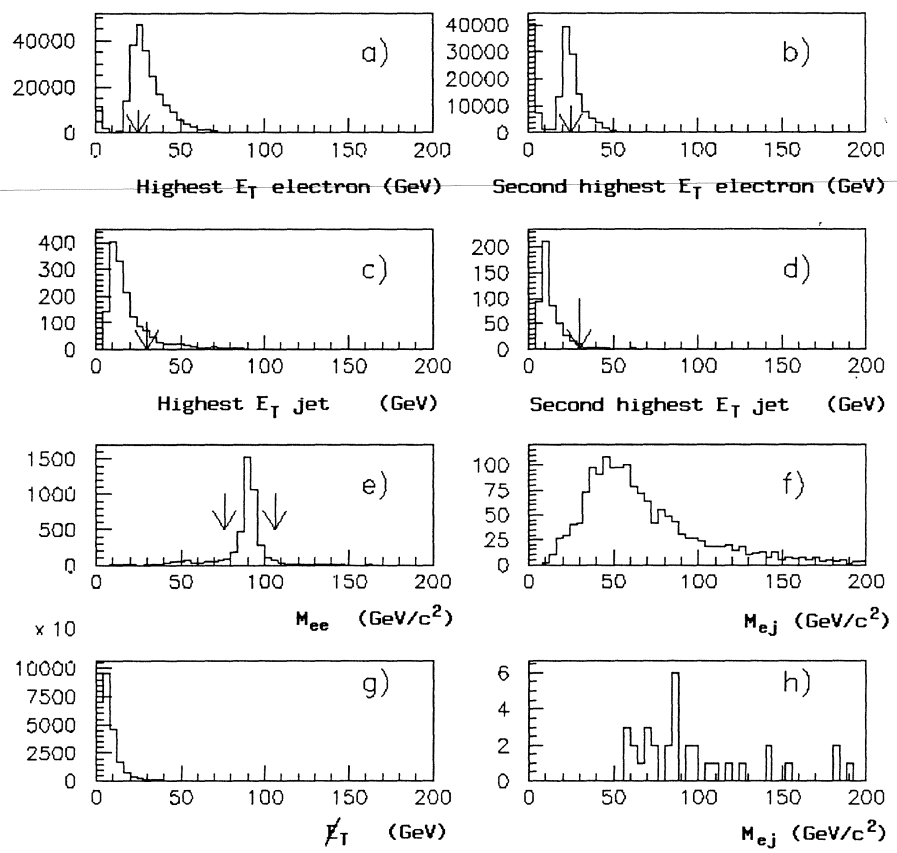

Figure 5.6: Distributions of kinematic quantities for Run Ib data. a, b, c, d and g are the electron and jet E_T, and $\not{E}_T$ distribution; e is the invariant mass distribution of the dielectron pair. f is the invariant mass distribution of ej with two electrons of $E_T > 10$ GeV excluded from the jets; h is the invariant mass distribution of ej with two electrons of $E_T > 25$ GeV and two jets of $E_T > 30$ GeV requirements.

Table 5.6: The number of events passing the imposed cuts. All the events in the table passed the trigger requirements and the electron identification criteria (see text). Three events from Run I survive all the offline cuts except the LQ mass window cuts.

Cuts imposed	No. of events passing cuts
$2e + 2j$: $E_T^e > 25$ GeV, $E_T^j > 30$ GeV	22
$2e + 2j$: $E_T^e > 25$ GeV, $E_T^j > 30$ GeV $M_{ee} > 106$ GeV/c^2 or < 76 GeV/c^2	3

where M_1 and M_2 are reconstructed masses of the two ej pairs for the candidate event, and M_{LQ} is the hypothesized LQ mass. 0.3 is used because the cut $\delta M_{LQ} \leq 0.3$ was used before. The lower and upper band of LQ masses between which the candidate event survives can be obtained by solving the above equation.

5.1.6 Background Estimation

Physics Backgrounds. As described in Section 5.1.2, the most important physics backgrounds are $Z, \gamma^* \rightarrow ee$ production in conjunction with jets (Z+jets), $t\bar{t}$ production with the two W bosons decaying into e and ν_e, $Z \rightarrow \tau\tau$ where both τ's decay into $e\nu_e\nu_\tau$, WW production in conjunction with jets with both W bosons decaying into e and ν_e.

$Drell - Yan$ $(Z, \gamma^* \rightarrow ee)$: As indicated in Section 5.1.2, four Z, γ^* + jets MC event sets were produced with different Z, γ^* mass due to the strong M_{ee} dependence of the cross section. The event generator ISAJET v7.13 and v7.22 was used to produce the events and showerlibrary was used to simulate the DØ detector. Because ISAJET uses a leading order calculation and Z, γ^* + 2 jets events are higher order process, the cross section of Z, γ^* + 2 jets events given by ISAJET is not correct. If we calculate the expected number of Z, γ^* + 2 jets events based on the ISAJET cross

Table 5.7: Detailed information on the three candidate events before the δM cut.

Object(run 84870, event 29117)	E_T (GeV)	η	φ
Electron 1	62.51	1.73	4.83
Electron 2	48.65	0.79	0.81
Jet 1	75.61	-0.33	3.07
Jet 2	74.74	-0.86	5.82
Jet 3	34.36	-0.94	2.46
$\not{E}_T$	12.44	–	1.04
M_{ee} (GeV/c^2)	113.1		
M_{e1j1} (GeV/c^2)	130.6		
M_{e2j2} (GeV/c^2)	239.7		
M_{e1j2} (GeV/c^2)	131.7		
M_{e2j1} (GeV/c^2)	198.8		

Object(run 90278, event 31411)	E_T (GeV)	η	φ
Electron 1	53.08	−0.02	4.15
Electron 2	33.46	−1.85	0.28
Jet 1	77.52	1.26	0.81
Jet 2	34.47	−1.54	2.95
$\not{E}_T$	6.34	–	1.49
M_{ee} (GeV/c^2)	118.4		
M_{e1j1} (GeV/c^2)	154.9		
M_{e2j2} (GeV/c^2)	66.9		
M_{e1j2} (GeV/c^2)	86.4		
M_{e2j1} (GeV/c^2)	232.2		

Object(run 92263, event 14233)	E_T (GeV)	η	φ
Electron 1	33.65	−0.14	0.74
Electron 2	26.87	−0.68	1.01
Jet 1	53.53	−1.74	4.32
Jet 2	32.56	0.41	2.85
$\not{E}_T$	10.50	–	3.99
M_{ee} (GeV/c^2)	18.2		
M_{e1j1} (GeV/c^2)	111.9		
M_{e2j2} (GeV/c^2)	57.7		
M_{e1j2} (GeV/c^2)	60.3		
M_{e2j1} (GeV/c^2)	86.5		

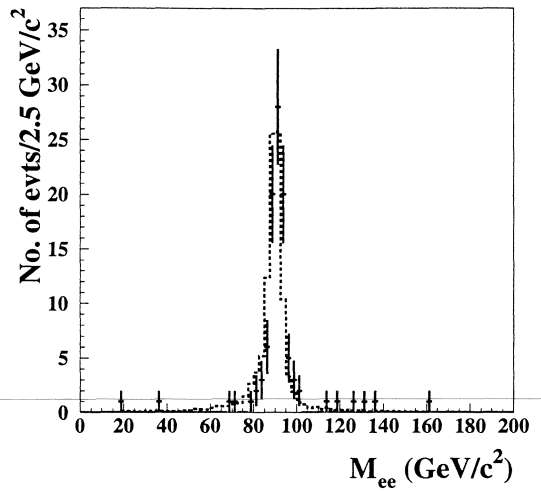

Figure 5.7: Invariant mass distribution for electron pairs requiring two electrons with $E_T > 25$ GeV and two jets with $E_T > 15$ GeV. Points are Run I data. Dashed line is the total expected background.

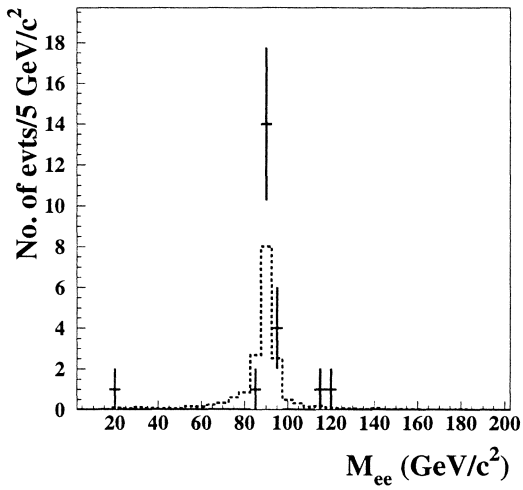

Figure 5.8: Invariant mass distribution for electron pairs requiring two electrons with $E_T > 25$ GeV and two jets with $E_T > 30$ GeV. Points are Run I data. Dashed line is the total expected background.

section, we may underestimate this background. However, we can treat these four sets of Z, γ^* events as four independent backgrounds. Then the ISAJET calculated cross section can be used along with the data to calculate the expected number of events inside and outside the Z mass range 76–106 GeV/c^2. In order to reduce the statistical error, two good electrons are required with $E_T > 25$ GeV, but the two jets requirement is loosened to $E_T > 15$ GeV. The number of expected events inside the Z mass range 76–106 GeV/c^2 is scaled to the number of Run I events inside the same range after all other backgrounds (including mismeasurement background, see Section 5.1.6) are subtracted from the data. The scaling factor is 1.165. Table 5.8 shows the number of events for Run I data and backgrounds inside and outside the Z boson mass range 76–106 GeV/c^2 with the looser cuts. Then, the offline cuts are applied to the four sets of Z, γ^* MC events. The number of expected events outside the Z boson mass range is scaled by the scaling factor and is our expected background from the Z, γ^* + jets events. Table 5.9 shows the number of events from Z, γ^* background inside and outside the Z boson mass range 76–106 GeV/c^2 with the offline cuts. The total background from Z, γ^* events is 2.24 ± 0.24 events after the offline cuts without the leptoquark mass window cut.

$t\bar{t} \rightarrow ll$: For the $t\bar{t}$ background, events were generated with event generator HERWIG v5.7, and with showerlibrary and trigger simulation. The top quark mass is assumed to be 170 GeV/c^2. The dependence of kinematic and fiducial cuts acceptance on the top mass around the real top mass is small and was ignored [48, 49]. The DØ measured $t\bar{t}$ pair production cross section of 5.77 ± 1.76 pb for top mass of 170 GeV/c^2 was used [48]. The number of expected $t\bar{t} \rightarrow ll$ events corresponding to 117.7 pb^{-1} integrated luminosity is 0.74 ± 0.05 events without the LQ mass window cut.

$Z \rightarrow \tau\tau \rightarrow ll$: For the $Z \rightarrow \tau\tau \rightarrow ll$ background, in order to enhance the Z+jets–like topology, Z boson $p_T > 25$ GeV/c was required at the generator level. To

Table 5.8: The number of events of Run I data and backgrounds inside and outside the Z boson mass range 76–106 GeV/c^2 with looser cuts: two electrons with $E_T >$ 25 GeV and two jets with $E_T >$ 15 GeV.

Physics Process	*ee* fiducial range	Number of events inside 76–106 GeV/c^2	Number of events outside 76–106 GeV/c^2
Z, γ^*(20–60 GeV/c^2)	CC–CC	0.00 ± 0.00	1.32 ± 0.20
	CC–EC	0.00 ± 0.00	0.27 ± 0.07
Z, γ^*(60–120 GeV/c^2)	CC–CC	49.16 ± 4.06	3.57 ± 0.42
	CC–EC	27.39 ± 2.21	1.20 ± 0.19
Z, γ^*(120–250 GeV/c^2)	CC–CC	0.02 ± 0.01	1.06 ± 0.10
	CC–EC	0.01 ± 0.01	0.71 ± 0.07
Z, γ^*(250–500 GeV/c^2)	CC–CC	0.00 ± 0.00	0.09 ± 0.01
	CC–EC	0.00 ± 0.00	0.06 ± 0.01
Z, γ^*(total)	–	76.58 ± 4.62	8.28 ± 0.52
other physics backgrounds	–	0.48 ± 0.03	1.37 ± 0.08
mismeasurement background	–	0.32 ± 0.12	0.76 ± 0.27
Run I data	–	90	10
scaling number	–	1.165	–

Table 5.9: The number of events from Run I data and expected backgrounds inside and outside the Z boson mass range 76–106 GeV/c^2 with the offline cuts: two electrons with $E_T > 25$ GeV and two jets with $E_T > 30$ GeV.

Physics Process	*ee* fiducial	Number of events	
		inside	outside
	range	76–106 GeV/c^2	76–106 GeV/c^2
Z,γ^*(20–60 GeV/c^2)	CC–CC	0.00 ± 0.00	0.46 ± 0.10
	CC–EC	0.00 ± 0.00	0.07 ± 0.03
Z,γ^*(60–120 GeV/c^2)	CC–CC	8.39 ± 0.82	0.76 ± 0.16
	CC–EC	4.25 ± 0.45	0.32 ± 0.09
Z,γ^*(120–250 GeV/c^2)	CC–CC	0.00 ± 0.00	0.18 ± 0.03
	CC–EC	0.01 ± 0.00	0.10 ± 0.02
Z,γ^*(250–500 GeV/c^2)	CC–CC	0.00 ± 0.00	0.02 ± 0.00
	CC–EC	0.00 ± 0.00	0.01 ± 0.00
Z,γ^*(total)	–	12.64 ± 0.94	1.92 ± 0.21
Z,γ^*(total) $\times$ 1.165	–	14.73 ± 1.10	2.24 ± 0.24
other physics backgrounds	–	0.29 ± 0.02	0.81 ± 0.05
mismeasurement background	–	0.05 ± 0.02	0.14 ± 0.05
total backgrounds	–	15.07 ± 1.10	3.19 ± 0.25
Run I data	–	19	3

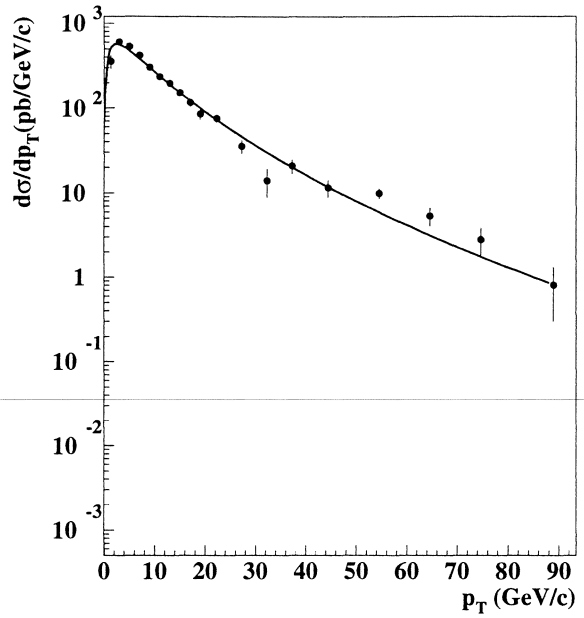

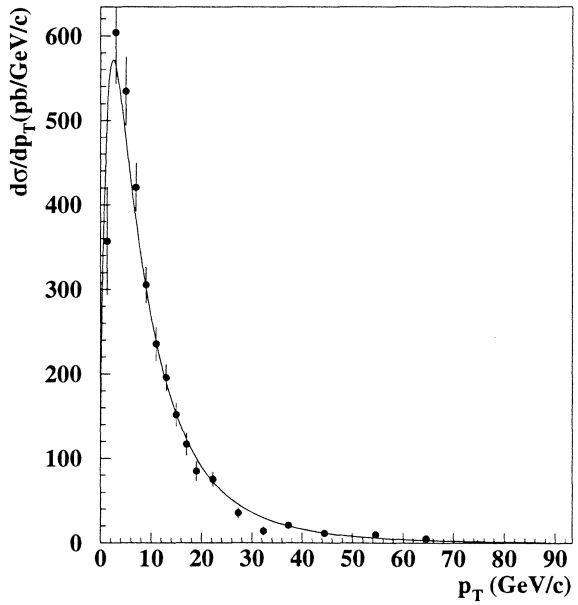

Figure 5.9: The DØ measured Z boson p_T distribution. The upper plot is semi-log scale and the lower plot is linear scale.

calculate the cross section for Z boson $p_T > 25$ GeV/c, the DØ measured Z boson p_T distribution was used. Figure 5.9 shows the DØ measured Z boson p_T distribution [50] and the fit function. The Z boson p_T distribution was fit using function:

$$\frac{d\sigma}{dp_T} = \alpha_1 p_T^2 e^{-\alpha_2 p_T^{\alpha_3}} \tag{5.3}$$

where $\alpha_1 = 3.95 \times 10^4$ pb/(GeV/c)^2, $\alpha_2 = 4.48$, and $\alpha_3 = 0.33$. To get the cross section for Z boson production with $p_T > 25$ GeV/c, integrations over p_T range 25–500 and 0–500 GeV/c were calculated, respectively. Then the DØ measured Z boson cross section 6318.8 $\pm$ 486.7 pb [51] was scaled by the ratio of the two integrations. The result is the cross section for Z boson with $p_T > 25$ GeV/c, which is 644.0 $\pm$ 49.6 pb. Because the cross section is an exponential function of the Z boson p_T, the integration from 500 GeV/c to infinity is very small and therefore was ignored. The expected number of events from $Z \rightarrow \tau\tau$ corresponding to 117.7 pb^{-1} integrated luminosity is 0.04 ± 0.01 events without the leptoquark mass window cut.

$WW \rightarrow ee$: For the $WW \rightarrow ee$ background, events were generated with the event generator ISAJET v7.08 and followed by showerlibrary and trigger simulation. After the WW pair is produced, both W bosons decay into electron and neutrino. The cross section for WW pair production has been calculated to be 10 pb^{-1} [52]. The expected number of events from $WW \rightarrow ee$ is 0.03 ± 0.01 events without the leptoquark mass window cut.

Mismeasurement Background. As indicated in Section 5.1.2, the QCD mismeasurement background can not be ignored. The QCD background was studied using the collider data. The data from the QCD trigger JET_3_MON (requiring at least three jets (cone $R = 0.3$) with $E_T > 10$ GeV) corresponding to an integrated luminosity of 0.318 pb^{-1} was used.

First, the probability for a jet to be misidentified as an electron (with the electron identification criteria used in this analysis) was calculated. The events were required to pass the JET_3_MON trigger. Since JET_3_MON trigger selects events with three or more jets which are predominantly from QCD processes, the possibility that the events contain real electrons is very small. The electrons in these multijet events are mostly from mismeasurement. $\not\!\!E_T < 10$ GeV was required to reduce the number of $W +$ jets events. Real Z boson events were removed by requiring that the events had only one electron passing the offline cuts and if the invariant mass of the electron and any jet fell in the Z boson mass window, the jet was required to have EM fraction less than 0.9. The number of electrons with $E_T > 25$ GeV in the data was counted separately for the CC and EC regions. Then the number of jets with $E_T > 25$ GeV for the same sample was counted for the CC and EC regions. The probability for one jet to be misidentified as an electron is the number of electrons divided by the number of jets in the sample. The probability for two jets to be misidentified as two electrons is the square of the one electron probability. Table 5.10 shows the probabilities for one or two misidentified electrons.

Then, the QCD sample was used again to estimate the mismeasurement background. This time, the JET_3_MON trigger was required but without the $\not\!\!E_T$ cut. Four jets with $E_T > 25$ GeV were required. In each event, all the combinations of two jet pairs with $E_T > 25$ GeV were counted separately for CC–CC and CC–EC. For each combination, at least two of the remaining jets had to satisfy the offline jet cuts with $E_T > 30$ GeV (see Section 5.1.4). Otherwise, this combination was rejected. Then the invariant mass of the jets pair was calculated and was required to be $M_{jj} < 76$ GeV$/c^2$ or $M_{jj} > 106$ GeV$/c^2$. The number of the combinations was calculated and that number times the probability for two jets to be misidentified as two electrons is the mismeasurement background in 0.318 pb^{-1} data. Finally, the

Table 5.10: The probability for jets to be misidentified as electrons.

One electron		Two electrons	
$P_{j\to e}$(CC)	$P_{j\to e}$(EC)	P_{CC-CC}	P_{CC-EC}
$(1.56 \pm 0.52) \times 10^{-4}$	$(3.86 \pm 1.11) \times 10^{-4}$	$(2.43 \pm 1.62) \times 10^{-8}$	$(6.02 \pm 2.65) \times 10^{-8}$

mismeasurement background was scaled up to 117.7 pb^{-1} data. The mismeasurement background is 0.14 ± 0.05 without the leptoquark mass window cut.

Summary. For all the background processes studied, estimates of the yields expected for integrated luminosity of 117.7 pb^{-1} are 3.19 ± 0.25 events without the leptoquark mass window cut. The leptoquark mass window cut depends on leptoquark mass. Table 5.11 shows the total background events and the number of candidate events from Run I data with the leptoquark mass window cut. The LQ masses 68, 86, 160 and 180 GeV/c^2 are the boundary LQ masses obtained by solving Equation 5.2. The systematic errors come from the uncertainty in the integrated luminosity, physics background cross section uncertainties and the uncertainties in the electron and jet energy scales. The uncertainty in the integrated luminosity is about 5.4%. The uncertainty of jet energy scale is determined using the method described in Section 4.5. The uncertainty in the EM scale correction is small, about 0.4%. So the uncertainty in the EM scale correction is neglected. The resolution of the jet energy in both MC and data is about the same. The cross section uncertainties of $Z, \gamma^* \to ee$ events and WW events are assigned 20%, respectively. The cross section uncertainties of $t\bar{t}$ production and $Z \to \tau\tau$ events are from Ref. [48, 50]. So the systematic errors are calculated only considering the uncertainty of the cross section, the uncertainty of the integrated luminosity, and the uncertainty in jet energy scales. The errors are shown in different columns of Table 5.15 separately.

Table 5.11: The total background resulting from the $eejj$ LQ search. The column labelled "data" gives the number of events surviving in the combined Run I data sample after applying all selection requirements. The first, second, third and fourth errors in column two are statistical, jet energy scale uncertainty (4% + 1 GeV), cross section uncertainty, and luminosity uncertainty, respectively.

M_{LQ} (GeV/c^2)	Total Background Events	Run I Data
60	$0.23 \pm 0.07 \pm 0.04 \pm 0.05 \pm 0.01$	0
68	$0.47 \pm 0.09 \pm 0.12 \pm 0.10 \pm 0.02$	0
68	$0.47 \pm 0.09 \pm 0.12 \pm 0.10 \pm 0.02$	1
80	$0.83 \pm 0.12 \pm 0.25 \pm 0.17 \pm 0.04$	1
86	$0.94 \pm 0.13 \pm 0.22 \pm 0.20 \pm 0.05$	1
86	$0.94 \pm 0.13 \pm 0.22 \pm 0.20 \pm 0.05$	0
100	$1.20 \pm 0.15 \pm 0.14 \pm 0.26 \pm 0.06$	0
120	$0.97 \pm 0.13 \pm 0.26 \pm 0.22 \pm 0.05$	0
140	$0.64 \pm 0.11 \pm 0.19 \pm 0.14 \pm 0.03$	0
160	$0.32 \pm 0.08 \pm 0.10 \pm 0.07 \pm 0.02$	0
160	$0.32 \pm 0.08 \pm 0.10 \pm 0.07 \pm 0.02$	1
180	$0.12 \pm 0.04 \pm 0.03 \pm 0.02 \pm 0.01$	1
186	$0.12 \pm 0.03 \pm 0.03 \pm 0.02 \pm 0.01$	1
186	$0.12 \pm 0.03 \pm 0.03 \pm 0.02 \pm 0.01$	0
200	$0.06 \pm 0.01 \pm 0.04 \pm 0.01 \pm 0.00$	0
220	$0.03 \pm 0.01 \pm 0.01 \pm 0.01 \pm 0.00$	0
240	$0.02 \pm 0.01 \pm 0.01 \pm 0.00 \pm 0.00$	0
260	$0.01 \pm 0.01 \pm 0.01 \pm 0.00 \pm 0.00$	0

5.1.7 Signal Efficiency

As described above, there are three candidate events from Run I data without the leptoquark mass window cut. The total expected background is 3.19 $\pm$ 0.25 events in agreement with the data. After the leptoquark mass window cut is applied, the number of candidate events is still in agreement with the background estimation. In order to determine the mass limit on leptoquarks, the signal efficiency must be studied. Here the signal efficiency includes the efficiencies of the trigger, kinematic, fiducial and electron quality cuts.

Method. We could impose the same kinematic and quality cuts on the MC signal events as on the Run I data if the MC signal events were simulated perfectly. The kinematic and fiducial quantities can be simulated reasonably well in the MC events, however, to find a good electron, more detailed knowledge about the EM shower development (both longitudinal and transverse) must be taken into account. So the Run I data along with the MC events is used to calculate the signal efficiency.

Trigger Efficiency. As described in Section 5.1.5, the L2 filters ELE_2_HIGH, EM2_EIS_EIS and EM2_EIS2_HI require not only trigger tower kinematic cuts, but also electromagnetic shower shape and isolation cuts. Shower shape and energy distribution due to the underlying event are not simulated reliably enough to allow a determination of the trigger efficiency from MC events alone. The kinematic acceptance of the filter can be calculated using the Monte Carlo events by imposing the L1 and L2 kinematic criteria. The efficiency of the electron shape and isolation requirements is obtained using the collider data. During Run Ib data taking, the EM2_EIS_ESC filter has the same kinematic requirements for the highest two EM clusters and the same electron shape requirement for the highest EM cluster as the EM2_EIS_EIS filter. The only difference is that the EM2_EIS_ESC filter did not require any shape or isolation cuts for the second highest EM cluster, whereas

the EM2_EIS_EIS filter did require the electron shape and isolation cuts. The L2 electron shape and isolation cuts efficiency of the EM2_EIS_EIS filter can be obtained by comparing EM2_EIS_ESC and EM2_EIS_EIS after requiring that there are two electrons with $E_T > 25$ GeV and $|\eta| < 2.5$:

$$\begin{aligned} \varepsilon_{EIS} &= \frac{N_2}{N_1} \\ &= (99.1\ ^{+0.9}_{-2.3})\% \end{aligned} \tag{5.4}$$

where N_1 is the number of events passing trigger EM2_EIS_ESC, N_2 is the number of events passing triggers EM2_EIS_ESC and EM2_EIS_EIS, and the error is statistical only. Using the same method, the efficiency for electron shape cut (ELE) can be obtained:

$$\varepsilon_{ELE} = (99.3\ ^{+0.7}_{-2.3})\% \tag{5.5}$$

The efficiency for the kinematic part is 100% for ELE_2_HIGH, EM2_EIS_EIS and EM2_EIS2_HI. Because the three triggers used in this channel have the same kinematic efficiency, almost the same electron shape cut efficiency. Moreover, Run Ib data account for 85% of the total Run I data. Therefore, EM2_EIS_EIS is used to estimate the trigger efficiency.

Combining the filter level electron shape and isolation cuts efficiency and the L1 and L2 kinematic cuts acceptance, we can obtain the trigger efficiency for EM2_EIS_EIS:

$$\begin{aligned} \varepsilon_{trig} &= \varepsilon^2_{EIS} \cdot \frac{N_p}{N_T} \\ &= (98.2\ ^{+1.8}_{-4.6})\% \end{aligned} \tag{5.6}$$

where N_p is the number of events passing the kinematic requirements of L1 and L2 triggers in addition to the offline kinematic cuts described in Section 5.1.4 and N_T is the number of events passing the offline kinematic cuts only.

Electron ID Efficiency. Since the quality parameters of the electron identification cannot be simulated well, the only way to get the electron identification cut efficiency is from collider data. The method used to determine the electron ID efficiency is similar to that in Ref. [53]. Because Ref [53] used Run Ia data, the electron ID efficiency needs to be recalculated using Run Ib data. The Run Ib $Z \rightarrow ee$ collider data (from the WZ group) are used to calculate the electron ID efficiency. Only events passing the EM2_EIS_EIS filter are accepted from the $Z \rightarrow ee$ data. Because of the difference between the central calorimeter (CC) and forward calorimeter (EC), the electron ID cut efficiency is obtained separately for the two regions. The CC fiducial region is defined by the detector η of the EM centroid $|\eta_{det}| < 1.2$; the EC fiducial region is defined by $1.2 < |\eta_{det}| < 2.5$. To get a sample of unbiased electrons with a reduced level of background, one electron is tagged with the electron ID cuts (described in Section 5.1.5), fiducial cut of $|\eta| < 2.5$, and kinematic cut of $E_T > 25$ GeV. The other electron must pass the kinematic cut of $E_T > 25$ GeV and have $|\eta_{det}| < 2.5$. Here "unbiased" means that no offline electron ID cut have been applied but the object has been loosely identified as an electron. Because the electron ID cut efficiency depends on the electron E_T, the same $Z \rightarrow ee$ sample is used twice. The first time, the first electron is tagged and the second electron is counted as an unbiased sample. Then, the second electron is tagged and the first electron is counted as an unbiased sample. The electron ID efficiency is calculated based on the sum of these two samples. Figure 5.10 shows the invariant mass distribution of the tagged electron and the unbiased electron in the CC; Figure 5.11 shows the invariant mass distribution of the tagged electron and the unbiased electron in the EC.

Because the unbiased sample contains some background, a parent sample is defined consisting of all unbiased electrons from dielectron pairs with invariant mass M_{ee} in the range 86 GeV/c^2 $< M_{ee} <$ 106 GeV/c^2 and a control sample is defined

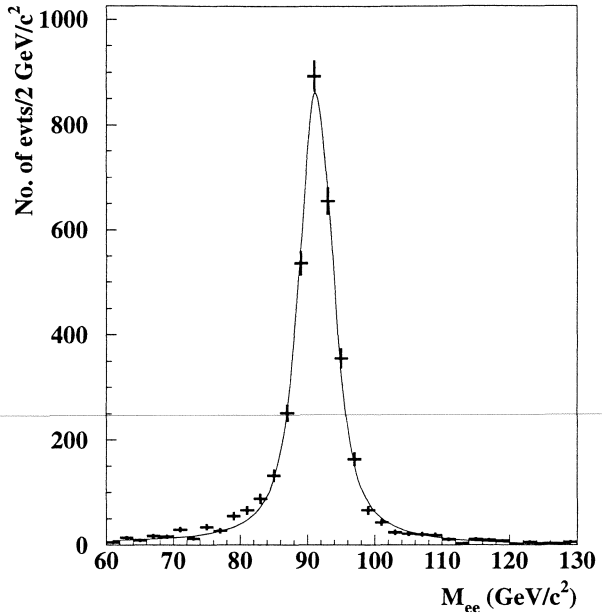

Figure 5.10: Invariant mass distribution for electron pairs with unbiased electron in the CC.

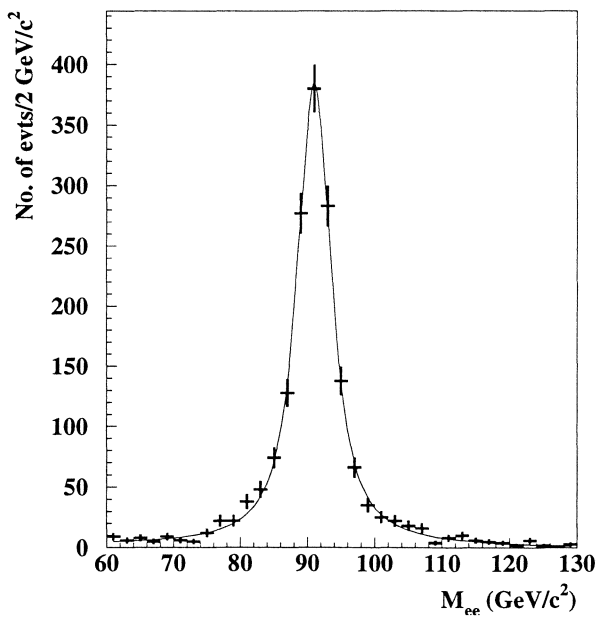

Figure 5.11: Invariant mass distribution for electron pairs with unbiased electron in the EC.

consisting of all the unbiased electrons from the dielectron pairs with invariant mass M_{ee} in the range 60 GeV/c^2 < M_{ee} < 70 GeV/c^2. The control sample is assumed to be all background. The M_{ee} distributions of Figures 5.10 and 5.11 are fit using a Breit-Wigner curve convoluted with a Gaussian plus a straight line background. To estimate the fraction of background in the parent sample, the fit background straight line and the fit total curve are integrated over the parent sample range. The ratio of the above two integrations is the fraction of background in the parent sample. The background fraction f_b is 0.27% (0.40%) for the CC (EC).

In order to get the electron ID cut efficiency, the background must be subtracted from the parent sample. To do this, the above background fraction f_b was used. In addition, the control sample was used as pure background events to calculate the background efficiency defined as the ratio of the number of electrons passing the ID cut to the total number of electrons in the control sample. The efficiency for the electron ID cuts is then given by:

$$\begin{aligned} \varepsilon_{e-\mathrm{ID}} &= \frac{N_s^p}{N_s} \\ &= \frac{\varepsilon - \varepsilon_b f_b}{1 - f_b} \end{aligned} \tag{5.7}$$

where N_s is the total number of unbiased electrons in the parent sample, N_s^p is the number of unbiased electrons passing the ID cuts, ε is the fraction of electrons in the parent sample that pass the cuts and ε_b is the fraction of electrons in the control (background) sample passing the cuts. The electron ID efficiency is listed in Table 5.12. The uncertainty is due to the finite number of $Z \rightarrow ee$ events. The two-electron ID efficiency is given by:

$$\begin{aligned} \varepsilon_{e-\mathrm{ID}}(\mathrm{CC}-\mathrm{CC}) &= \varepsilon^2_{e-\mathrm{ID}}(\mathrm{CC}) \\ \varepsilon_{e-\mathrm{ID}}(\mathrm{CC}-\mathrm{EC}) &= \varepsilon_{e-\mathrm{ID}}(\mathrm{CC})\varepsilon_{e-\mathrm{ID}}(\mathrm{EC}) \\ \varepsilon_{e-\mathrm{ID}}(\mathrm{EC}-\mathrm{EC}) &= \varepsilon^2_{e-\mathrm{ID}}(\mathrm{EC}) \end{aligned} \tag{5.8}$$

Table 5.12: Efficiencies of the electron ID cuts used in this analysis obtained from $Z \rightarrow ee$ events.

electron ID cuts	eff. ε_{e-ID}(CC) (%)	eff. ε_{e-ID}(EC)(%)
$f_{EM} \geq 0.9$ $\Re \leq 0.5$ $f_{iso} \leq 0.1$	88.05 $\pm$ 2.49	65.78 $\pm$ 3.02

Table 5.13: Two-electron ID cut efficiencies used in this analysis obtained from $Z \rightarrow ee$ events.

eff. ε_{e-ID}(CC-CC) (%)	eff. ε_{e-ID}(CC-EC)(%)	eff. ε_{e-ID}(EC-EC)(%)
77.53 $\pm$ 4.38	57.92 $\pm$ 3.12	43.27 $\pm$ 3.97

Table 5.13 shows the two electron ID efficiencies with the electrons in the CC–CC, CC–EC, and EC–EC fiducial regions.

In addition to the electron ID, there is a difference between the MC and collider data for the electron track finding efficiency. The correction factor for the MC sample is $\varepsilon_{trk}(\mathrm{CC}) = 0.873 \pm 0.013$ for a CC electron and $\varepsilon_{trk}(\mathrm{EC}) = 0.939 \pm 0.020$ for a EC electron [54]. So the correction for the electron pairs is [54]:

$$\begin{aligned} \varepsilon_{trk}(CC-CC) &= \varepsilon^2_{trk}(\mathrm{CC}) \\ &= (76.2 \pm 2.3)\% \qquad (5.9) \\ \varepsilon_{trk}(CC-EC) &= \varepsilon_{trk}(\mathrm{CC})\varepsilon_{trk}(\mathrm{CC}) \\ &= (82.0 \pm 2.1)\% \qquad (5.10) \\ \varepsilon_{trk}(EC-EC) &= \varepsilon^2_{trk}(\mathrm{EC}) \\ &= (88.2 \pm 3.8)\% \qquad (5.11) \end{aligned}$$

Offline Cut Acceptance. The offline kinematic cuts for the two electrons and two jets include E_T, fiducial cuts, Z boson mass cut, and LQ mass window cut. The MC events passing these cuts are then grouped into three subgroups according to the location of the two electrons (CC–CC, CC–EC, EC–EC). The offline kinematic acceptances are:

$$\begin{aligned} A(\mathrm{CC}-\mathrm{CC}) &= \frac{N_{\mathrm{CC-CC}}}{N_{tot}} \\ A(\mathrm{CC}-\mathrm{EC}) &= \frac{N_{\mathrm{CC-EC}}}{N_{tot}} \\ A(\mathrm{EC}-\mathrm{EC}) &= \frac{N_{\mathrm{EC-EC}}}{N_{tot}} \end{aligned} \tag{5.12}$$

where A(CC-CC) is the kinematic acceptance for events with both electrons in the CC region (same for the other two combinations), $N_{\mathrm{CC-CC}}$ is the number of events with both electrons in the CC region passing the kinematic cuts, and N_{tot} is the total number of events. Table 5.14 shows the offline kinematic cut acceptance for the MC events at different leptoquark masses. For both electron in the EC region, the acceptance is less than 1%. Considering the two EC electron ID efficiency (43.27 $\pm$ 3.97) %, the contribution to the total MC signal efficiency from EC–EC electrons is about 0.5%. So events with both electrons in the EC region are rejected.

Overall Efficiency. Finally then, the overall MC signal efficiency can be obtained by combining the trigger efficiency, electron ID cut efficiency, electron tracking efficiency, and the kinematic acceptance. The overall signal efficiency is given by:

$$\begin{aligned} \varepsilon_s &= A(\mathrm{CC}-\mathrm{CC})\varepsilon_{e-\mathrm{ID}}(\mathrm{CC}-\mathrm{CC})\varepsilon_{trk}(\mathrm{CC}-\mathrm{CC})\varepsilon_{trig} + \\ &\quad A(\mathrm{CC}-\mathrm{EC})\varepsilon_{e-\mathrm{ID}}(\mathrm{CC}-\mathrm{EC})\varepsilon_{trk}(\mathrm{CC}-\mathrm{EC})\varepsilon_{trig} \end{aligned} \tag{5.13}$$

The result is shown in Table 5.15. The efficiencies of masses 63, 68, 86, 93 and 186 GeV/c^2 are from a linear interpolation using the efficiencies of the two nearest LQ mass.

Table 5.14: Offline cuts acceptance for the leptoquark MC events at different mass points in $eejj$ channel. The uncertainties in the table are statistical only.

M_{LQ} (GeV/c^2)	A(CC–CC) (%)	A(CC–EC) (%)
60	1.50 ± 0.27	0.35 ± 0.13
80	5.40 ± 0.52	1.10 ± 0.23
100	9.65 ± 0.69	3.25 ± 0.40
120	13.85 ± 0.83	4.80 ± 0.49
140	17.05 ± 0.92	5.60 ± 0.53
160	22.40 ± 1.06	5.85 ± 0.54
180	23.20 ± 1.08	7.00 ± 0.59
200	26.15 ± 1.14	8.55 ± 0.65
220	25.28 ± 0.71	8.68 ± 0.42
240	26.14 ± 0.72	8.72 ± 0.42
260	27.74 ± 0.74	9.18 ± 0.43

5.1.8 Signal Cross Section Upper Limit Calculation

For the search for leptoquark pair production in the 2 e + 2 jets channel, three events survive in the data before the leptoquark mass window cut is applied. The total background is 3.19 ± 0.25 events. After the leptoquark mass window cut is applied, none or one event survive for different LQ mass point. The number of candidates events is consistent with the prediction from the Standard Model. So there is no evidence for leptoquark pair production. From the MC signal efficiency, total backgrounds, the number of observed candidates (Table 5.15), and the total luminosity, a 95% confidence level cross section limit on the leptoquark pair production

Table 5.15: The signal efficiency from the $eejj$ LQ search. The errors on efficiency is statistical only.

M_{LQ}	Signal Efficiency %		
(GeV/c^2)	Mean	Lower band	Upper band
60	1.03 ± 0.18	0.49	1.09
63	1.42 ± 0.21	0.81	1.51
68	2.08 ± 0.27	1.33	2.20
80	3.65 ± 0.41	2.60	3.87
86	4.69 ± 0.48	3.57	5.03
93	5.90 ± 0.56	4.71	6.39
100	7.11 ± 0.64	5.84	7.74
120	10.27 ± 0.85	8.49	10.99
140	12.50 ± 1.00	11.04	13.25
160	15.73 ± 1.24	14.22	16.38
180	16.73 ± 1.29	15.02	17.53
186	17.46 ± 1.34	15.75	18.21
200	19.16 ± 1.44	17.45	19.78
220	18.72 ± 1.28	17.34	19.60
240	19.23 ± 1.32	17.90	20.19
260	20.38 ± 1.40	19.15	21.33

can be calculated using Bayesian statistics. The general method of limit calculation using Bayesian statistics is described in Ref. [55] and is outlined below.

5.1.9 Outline of Signal Cross Section Upper Limit Calculation

For discrete k, let us use the symbol $P(k|\mu, I)$ to represent the probability of observing k given that propositions μ and I are true. In a particular counting experiment, if k represents the number of observed events and μ represents the expected number of events, the likelihood function of the probability $P(k|\mu, I)$ can be described using the Poisson distribution function:

$$P(k|\mu, I) = \frac{e^{-\mu}\mu^k}{k!} \tag{5.14}$$

where I indicates all the information used to calculate μ, as well as the assumption that the Poisson distribution is the correct function to describe the probability. We call I the *prior* condition. The expected number of events can be written as:

$$\mu = b + L\epsilon\sigma \tag{5.15}$$

where b is the total background from the Standard Model, L is the integrated luminosity, ϵ is the overall signal efficiency, and σ is the theoretical (assumed) signal production cross section. Combing Equation 5.15 and Equation 5.14, the probability of observing k events is:

$$P(k|\sigma, L, \epsilon, b, I) = \frac{e^{-(b+L\epsilon\sigma)}(b + L\epsilon\sigma)^k}{k!} \tag{5.16}$$

Now, the interesting question is: given the k observed events, what is the probability that the leptoquark cross section is σ? Here, Bayes' theorem is used to calculate the probability:

$$\begin{aligned} P(\sigma, L, \epsilon, b|k, I) &\propto P(k|\sigma, L, \epsilon, b, I)P(\sigma, L, \epsilon, b|I) \\ &\propto \frac{e^{-(b+L\epsilon\sigma)}(b + L\epsilon\sigma)^k}{k!}P(\sigma, L, \epsilon, b|I) \end{aligned} \tag{5.17}$$

where the constant of proportionality is determined by the condition:

$$\int_0^\infty d\sigma \int_0^\infty dL \int_0^1 d\epsilon \int_0^\infty dbP(\sigma, L, \epsilon, b|k, I) = 1.0 \tag{5.18}$$

A good assumption can be made that σ, L, ϵ, b are independent of each other. So $P(\sigma, L, \epsilon, b|I)$ can be written as the product of the individual probabilities:

$$P(\sigma, L, \epsilon, b|I) = P(\sigma|I)P(L|I)P(\epsilon|I)P(b|I) \tag{5.19}$$

Although no one knows the true cross section for the pair production of leptoquarks, we can assume the maximum cross section for leptoquark production and assume a flat prior probability like:

$$P(\sigma|I) = \begin{cases} \frac{1}{\sigma_{max}} & \text{if } \sigma > 0 \\ 0 & \text{otherwise} \end{cases} \tag{5.20}$$

σ_{max} is chosen so that the probability that the leptoquark production cross section is greater than σ_{max} is very small. The other prior probability distributions are assumed to be truncated normal distributions:

$$P(L|I) = \begin{cases} \frac{1}{\sigma_L\sqrt{2\pi}} e^{-\frac{(L-\bar{L})^2}{2\sigma_L^2}} & \text{if } L > 0 \\ 0 & \text{otherwise} \end{cases} \tag{5.21}$$

$$P(\epsilon|I) = \begin{cases} \frac{1}{\sigma_\epsilon\sqrt{2\pi}} e^{-\frac{(\epsilon-\bar{\epsilon})^2}{2\sigma_\epsilon^2}} & \text{if } \epsilon > 0 \\ 0 & \text{otherwise} \end{cases} \tag{5.22}$$

$$P(b|I) = \begin{cases} \frac{1}{\sigma_b\sqrt{2\pi}} e^{-\frac{(b-\bar{b})^2}{2\sigma_b^2}} & \text{if } b > 0 \\ 0 & \text{otherwise} \end{cases} \tag{5.23}$$

where σ_L, σ_ϵ and σ_b are the errors for L, ϵ and b, respectively; $\bar{L}$, $\bar{\epsilon}$ and $\bar{b}$ are the mean values for L, ϵ and b, respectively.

At this stage, the uninteresting parameters (nuisance parameters) in Equation 5.17 can be integrated out:

$$P(\sigma|k,I) = \int_0^\infty dL \int_0^1 d\epsilon \int_0^\infty dbP(\sigma, L, \epsilon, b|k, I) \tag{5.24}$$

After normalization, $P(\sigma|k,I)$ is called the *posterior probability distribution.* $P(\sigma|k,I)$ is the probability distribution for the leptoquark production cross section given the data observed. The 95% confidence level cross section upper limit can be determined by solving the equation:

$$0.95 = \int_0^{\sigma_{UL}} d\sigma P(\sigma|k,I) \tag{5.25}$$

where $P(\sigma|k,I)$ is normalized and σ_{UL} is what we called the *cross section upper limit.*

In practice, the posterior probability distribution for the signal cross section is calculated using the **LIMIT** program [56]. The program performs Monte Carlo integration to solve the integrals and takes into account correlations between the errors. Figure 5.12 shows the leptoquark cross section upper limits at the 95% CL assuming a branching fraction $\beta = 1.0$. The bump on the 95% CL cross section limits between $M_{LQ} = 160$ GeV/c^2 and 186 GeV/c^2 is due to the fact that there is one candidate event between M_{LQ} masses 160 and 180 GeV/c^2. The theoretical cross sections are obtained by using CTEQ4M (with five flavors and $\Lambda_{QCD} = 202$ MeV) parton distribution functions (pdf) [23] at different renormalization scale for $\beta = 1$.

5.1.10 Results

For the intermediate points between any neighboring points of 95% CL cross section limit, linear interpolation is used to calculate the cross-section limits. The leptoquark mass limits are then obtained by translating the cross section limits to mass limits. The mass limit for $\beta = 1$ is 204 GeV/c^2 if the lower theoretical cross section band (corresponding to $\mu = 2M_{LQ}$) is used.

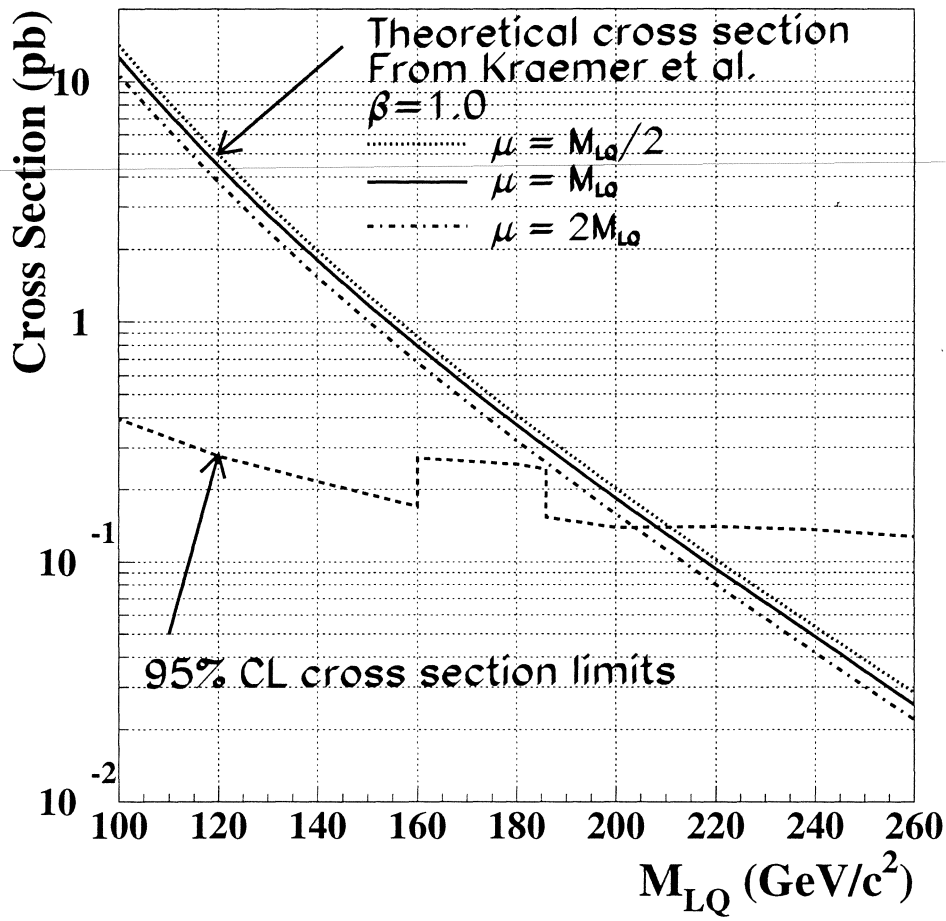

Figure 5.12: The 95% CL cross section upper limits for $\beta = 1.0$. Detailed information is given in the text.

5.2 $e\nu jj$ Channel

To understand the leptoquark and background signatures which have the final state $e\nu qq$, leptoquark pair production and major backgrounds were simulated using the ISAJET, VECBOS and HERWIG generators. The DØ detector response to the MC events was simulated using the DØ detector simulator DØGEANT. The DØ trigger information was stored in the MC events by running the trigger simulator. The events were reconstructed using the program DØRECO.

5.2.1 Signal Simulation

Leptoquark pair production at the Tevatron was simulated using the ISAJET v7.13 and v7.22 event generator for eleven leptoquark masses: M_{LQ} = 60, 80, 100, 120, 130, 140, 150, 160, 180, 200, 220, 240 and 260 GeV/c^2. There were no generator level cuts. The MC events were then passed through showerlibrary v3.14 and v3.15, trigger simulation (L2PROD v7.08), and reconstruction DØRECO v12.20 and v12.21. Table 5.16 shows the status of the signal MC samples.

5.2.2 Backgrounds

Any physics process with a final state reconstructed as one electron plus $\not\!\!E_T$ plus two jets can mimic the signal events. These are the backgrounds. As in the $eejj$ channel, the background events can be divided into two categories: physics backgrounds and mismeasurement backgrounds.

Physics Backgrounds. Physics backgrounds are those physics processes with a final state having at least one electron, one neutrino, and two quarks/gluons. Quarks/gluons could be reconstructed as jets. The most important physics backgrounds are: W + 2 jets where W decays into electron and neutrino and $t\bar{t}$ production with one W boson decaying into e and ν_e. The status of the physics background MC events are shown in Table 5.17.

Table 5.16: The status of the leptoquark pair production MC events in $e\nu jj$ channel.

M_{LQ} (GeV/c^2)	No. of events	Generator	GEANT version	RECO version
60	2000	ISAJET 7.13	v3.14	v12.20
80	2000	ISAJET 7.13	v3.14	v12.20
100	2000	ISAJET 7.13	v3.14	v12.20
120	2000	ISAJET 7.13	v3.14	v12.20
140	2000	ISAJET 7.13	v3.14	v12.20
160	2000	ISAJET 7.13	v3.14	v12.20
180	2000	ISAJET 7.13	v3.14	v12.20
200	2000	ISAJET 7.13	v3.14	v12.20
220	5000	ISAJET 7.22	v3.15	v12.21
240	5000	ISAJET 7.22	v3.15	v12.21
260	5000	ISAJET 7.22	v3.15	v12.21

$t\bar{t}$: For the $t\bar{t}$ background, events were generated with the event generator HERWIG v5.7. After the $t\bar{t}$ pair production, both top quarks decay into a b quark and a W boson, followed by one W boson decaying into $e\nu_e$, $\mu\nu_\mu$ or $\tau\nu_\tau$. So these MC events contain the contribution of tau decays into electrons: $W \rightarrow \tau\nu_\tau \rightarrow e\nu_e\nu_\tau\nu_\tau$. The top quark mass was assumed to be 170 GeV/c^2. These MC events were produced by the DØ top group and there were no generator level cuts.

$W + 2\ jets$: For the W + 2 jets background, events were generated with the event generator VECBOS and were put into PYTHIA v5.60 for hadronization. After the W boson is produced, it decays into a lepton and a neutrino. The events were produced by the DØ top group. At the generator level, the W boson p_T was required to be larger than 25 GeV/c.

Table 5.17: The status of the physics backgrounds MC events in $e\nu jj$ channel. The detailed information is addressed in the text.

Process	Cross section (pb)	No. of events	Generator	GEANT version	RECO version	Remarks
$t\bar{t} \rightarrow l$ + jets	2.62	101,339	HERWIG v5.7	v3.15	v12.21	top mass 170 GeV/c^2
W + 2 jets	810	345,296	VECBOS v3.0	v3.15	v12.21	$Q^2 =< p_T^2 >$, $W \rightarrow l\nu$

Mismeasurement Background. The mismeasurement background is mainly from QCD multijet production. For QCD events with three or more jets, if one of the jets is misidentified as an electron and the energy of the jets in the event is mismeasured, the events will have the "signature": 1 e + 2 jets + $\not\!\!E_T$. Because the probability for one jet to be misidentified as an electron is about 10^{-4}, the background from this source cannot be ignored.

5.2.3 Distributions of Physics Variables for MC Signal and MC Backgrounds

Distributions of the E_Ts of the electron, the leading and second leading jets, and the $\not\!\!E_T$ for the MC signal and background samples are shown in Figure 5.13. The events are normalized to the same luminosity for the signal events and background events and then scaled for display. The numbers in the plots for each process show the scaling for that process. No cuts have been applied for the leading electron E_T and $\not\!\!E_T$ distributions. One jet was required for the leading jet E_T distribution after one electron with $E_T > 10$ GeV has been required and excluded from jets. Two jet were required for the second leading jet E_T distribution after one electron with $E_T >$ 10 GeV has been required and excluded from jets. Figure 5.14 shows the electron and jet invariant mass distribution, the $\not\!\!E_T$ and jet transverse mass distribution for signal (M_{LQ} = 120 GeV/c^2) and background events with one electron and two or

more jets with $E_T > 10$ GeV. Figures 5.15 and 5.16 show the invariant mass (of an electron and a jet) vs. transverse mass (of $\not\!\!E_T$ and another jet).

5.2.4 Offline Events Selection Criterion

The criterion to choose the offline electron and jets kinematic cuts is to retain the greatest number of signal events while rejecting the greatest amount of background. Using the same method as described in Section 5.1.4, the requirements of one electron with $E_T > 25$ GeV and two jets with $E_T > 25$ GeV, and $\not\!\!E_T > 40$ GeV were determined. Because the final states have only one electron and the leptoquark signal tends to be central, one and only one CC electron was required. Two or more central jets ($|\eta| < 1.0$) with $E_T > 25$ GeV were required. More Selection Criterion are described in Section 5.2.5.

5.2.5 Data Selection

Data used in this analysis were taken during Run Ia (stream RUN1A_LQ_ENU), Run Ib (stream RUN1B_LQ_ENU) and Run Ic (stream RUN1C_LQ_ENU). After excluding bad runs and requiring GOOD–BEAM, the data sample represented a total integrated luminosity of $L = 103.7 \pm 5.6$ pb^{-1}.

As described in Section 5.1.5, before applying the offline cuts, the energies of electrons, photons and jets were corrected using the CAFIX 5.0 package.

After the leptoquark pair is produced, if one leptoquark decays to an electron and a quark and another leptoquark decays to a neutrino and a quark, the final state is 1 e, 2 jets, and large $\not\!\!E_T$. A sample of events with one isolated CC electron candidate was selected first. Then the kinematic cuts were imposed on the electron followed by the requirement of two high transverse energy central jets and $\not\!\!E_T$. The remaining events were mostly from W + 2 jets events. Finally tighter cuts were imposed to eliminate this background.

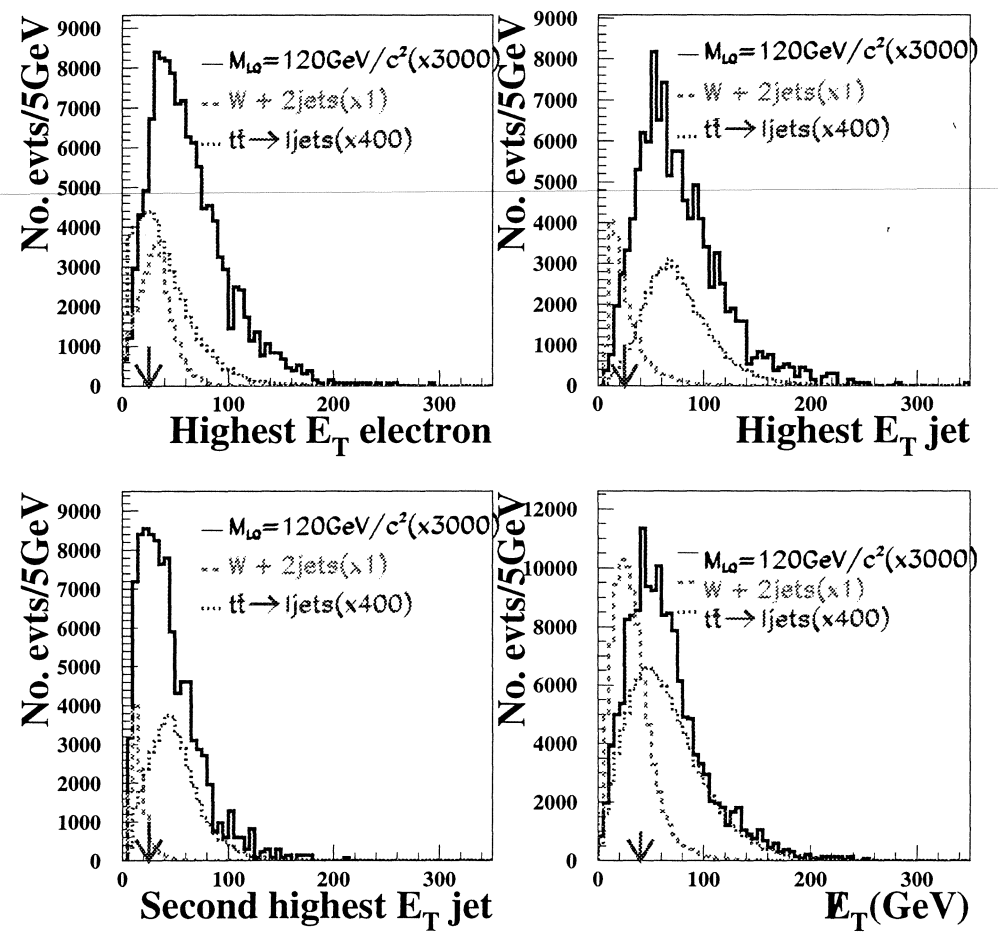

Figure 5.13: The kinematic distributions for the MC signal and background events. The arrows in the plots indicate the offline E_T cuts. More detailed information is given in the text.

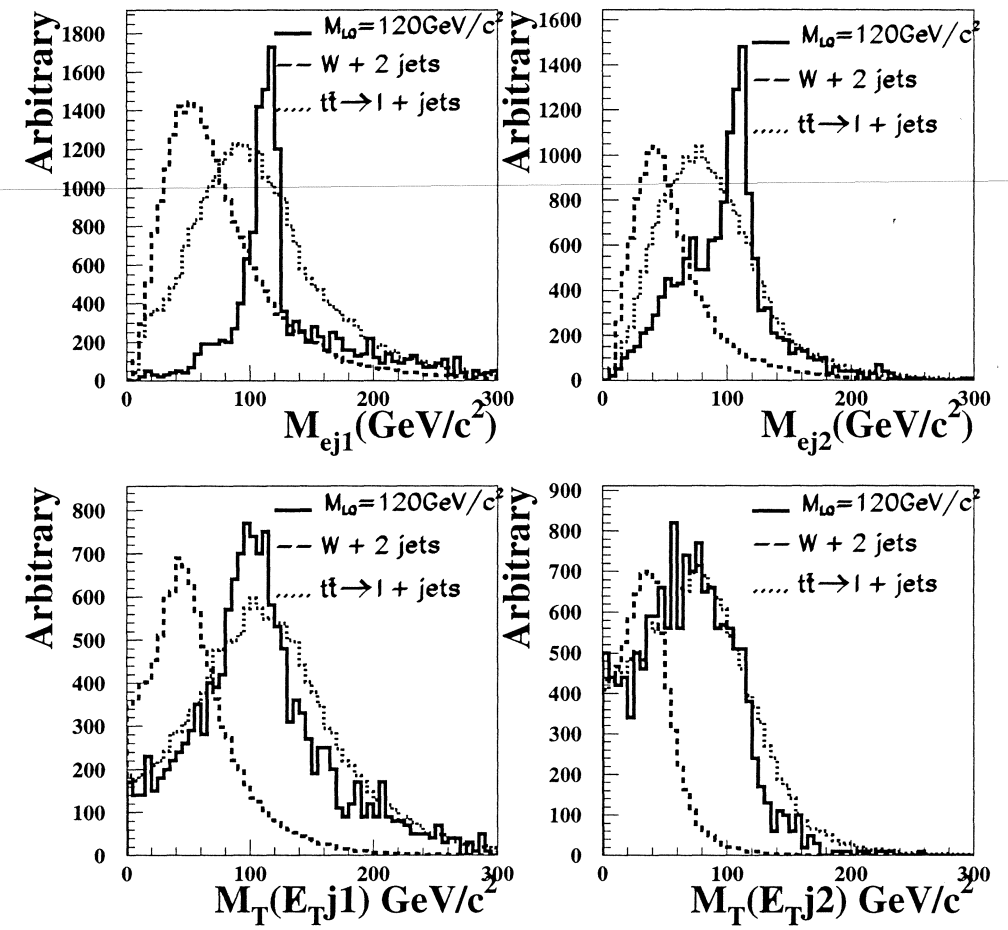

Figure 5.14: The invariant mass distributions (of an electron and one of the leading two jets j_1, j_2) and transverse mass distributions (of $\not\!\!E_T$ and one jet). One electron and two or more jets with E_T greater than 10 GeV were required.

L1 and L2 Trigger. Events from Run I had to pass the L1 trigger EM_JET which required at least 1 electromagnetic tower with $E_T > 12$ GeV and at least 2 hadronic plus EM trigger towers with $E_T > 5$ GeV.

In addition to the L1 trigger requirement, events passing ELE_JET (Run Ia) had to pass the online software L2 trigger requiring one or more electromagnetic clusters with $E_T > 12$ GeV, with electron longitudinal and transverse shape cuts, two or more jets with $E_T > 10$ GeV, and $\not\!\!E_T > 10$ GeV. Events passing ELE_JET_HIGH (Run Ib and Run Ic) had to pass the online software L2 trigger requiring one or more electromagnetic clusters with $E_T > 15$ GeV, with electron long longitudinal and transverse shape cuts, two or more jets with $E_T > 10$ GeV, and $\not\!\!E_T > 14$ GeV.

Offline Selection. After the candidate events passed the trigger requirements, they were required to satisfy the following offline requirements:

- Electrons:

  One and only one good electron, with $E_T > 25$ GeV in the Central Calorimeter (CC) region (defined as $|\eta| < 1.2$) was required. Requiring a CC electron keeps 90% of the signal and rejects about 60% of the QCD mismeasurement background. A good electron is an energy cluster which passes the following quality cuts:

  * electromagnetic fraction: $f_{EM} > 0.9$
  * four-variable likelihood: $\Re \leq 0.5$.
  * Cluster Isolation: $f_{iso} \leq 0.1$.

- Jets:

  Two central jets with $E_T > 25$ GeV in a fiducial region $|\eta| < 1.0$ must be found in the events. The central jets requirement has a signal efficiency of

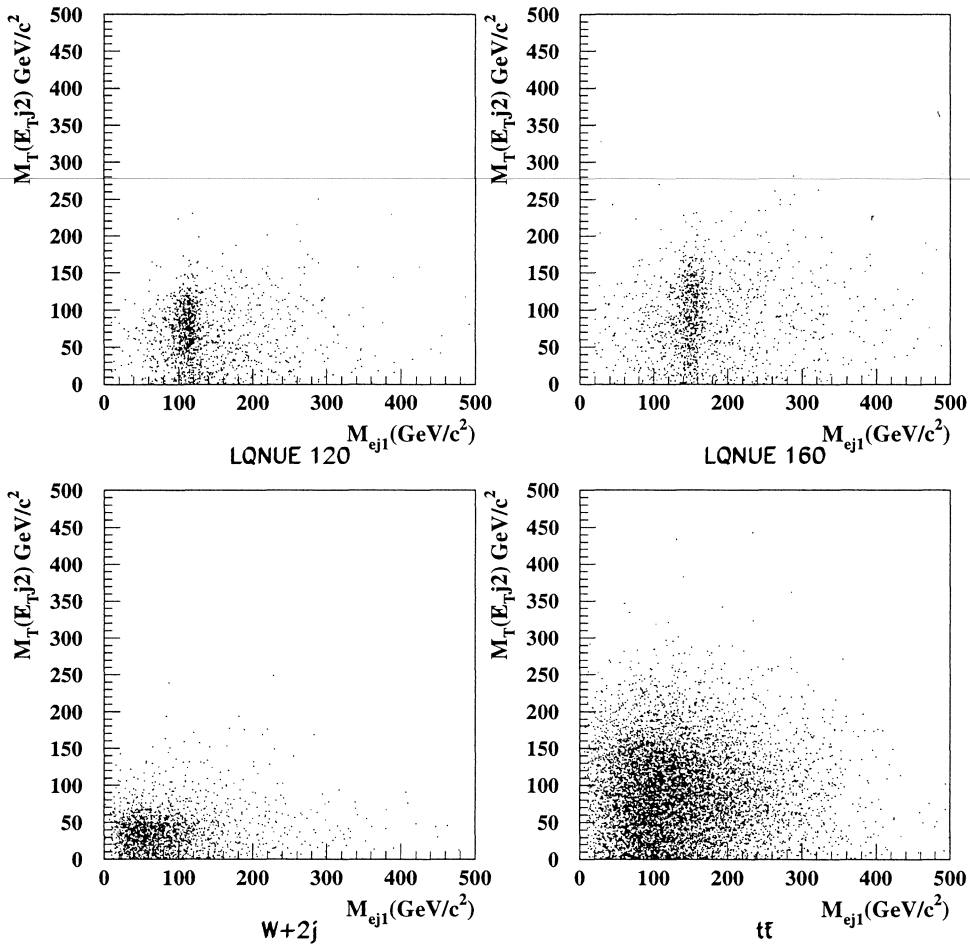

Figure 5.15: $M_{e,j1}$ vs. $M_T(\not{E}_T j2)$. One electron and two or more jets with $E_T > 10$ GeV was required.

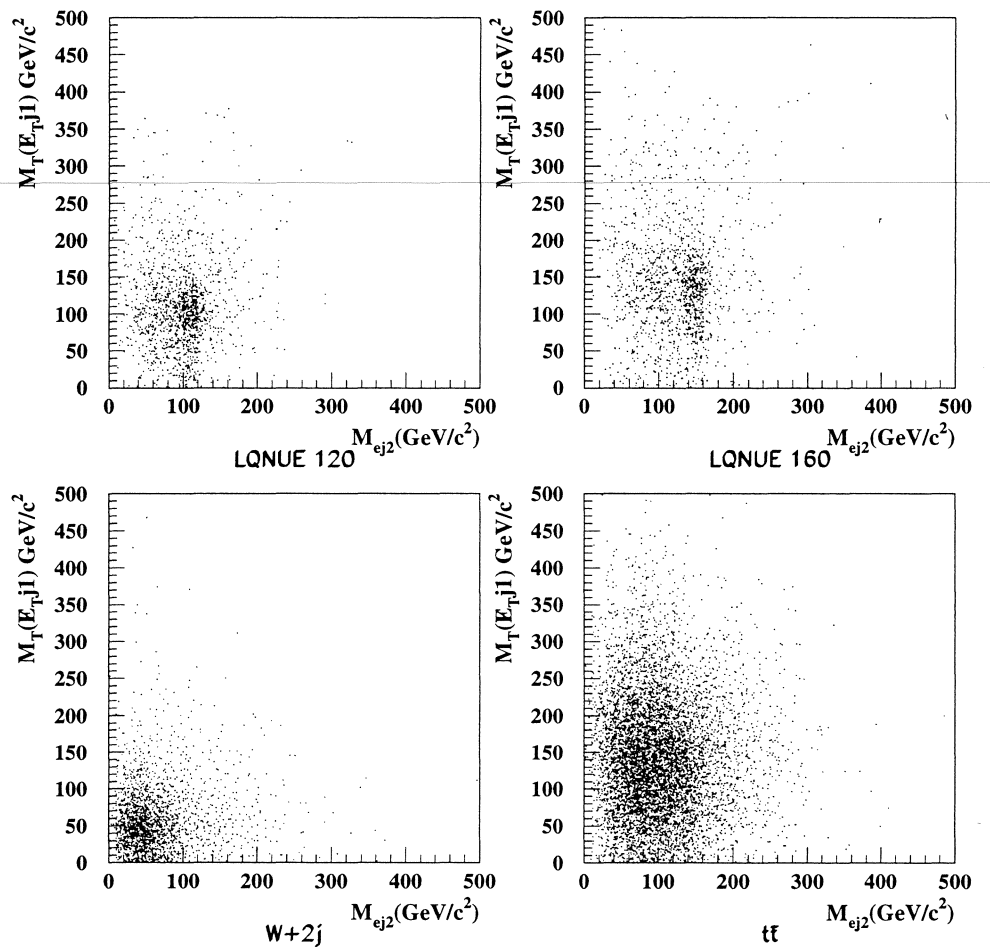

Figure 5.16: M_{ej2} vs. $M_T(\not{E}_T j1)$. One electron and two or more jets with $E_T > 10$ GeV was required.

80% while rejecting 50% of W + 2 jets events and QCD mismeasurement background. Because electrons are also identified as jets, the jets have to be separated from the electron in $\eta - \varphi$ space: $\delta R(e,j) = \sqrt{(\Delta\eta)^2 + (\Delta\varphi)^2} > 0.5$. The value 0.5 was selected because there are no heavy flavor quarks in the final states of first generation scalar leptoquarks and this cut eliminates some of the $t\bar{t}$ background. Top quarks decay into a b quark and a W boson and some b quarks decay into an electron and lighter quark. The electron and the lighter quark from a b quark decay tend to be very close together because of the Lorentz boost of the b quark.

- $\not{E}_T$:

  $\not{E}_T > 40$ GeV was required and the $\not{E}_T$ must not be opposite or parallel to the above two jets ($\Delta\varphi > 0.25$) to eliminate events having large $\not{E}_T$ due to jet E_T mismeasurement.

After the basic offline kinematic cuts described above, tighter cuts were imposed to further reduce the backgrounds:

- 2 or 3 jets:

  By looking at Figure 5.17 after the basic offline kinematic cuts, the $t\bar{t}$ background tends to have more high E_T jets per event. This is because top quarks decay into a b quark and a W boson. The W boson decays into either leptons or quarks. The first generation leptoquark events have only two quarks in the final states. Although there are initial and final state radiation in the leptoquark events, the jets from the initial and final state radiation tend to be soft. Thus only 2 or 3 jets with $E_T > 25$ GeV in a fiducial region $|\eta| < 2.5$ was required. This cut will have a signal efficiency of 85% – 88% depending on the leptoquark mass and rejects 40% of the top background.

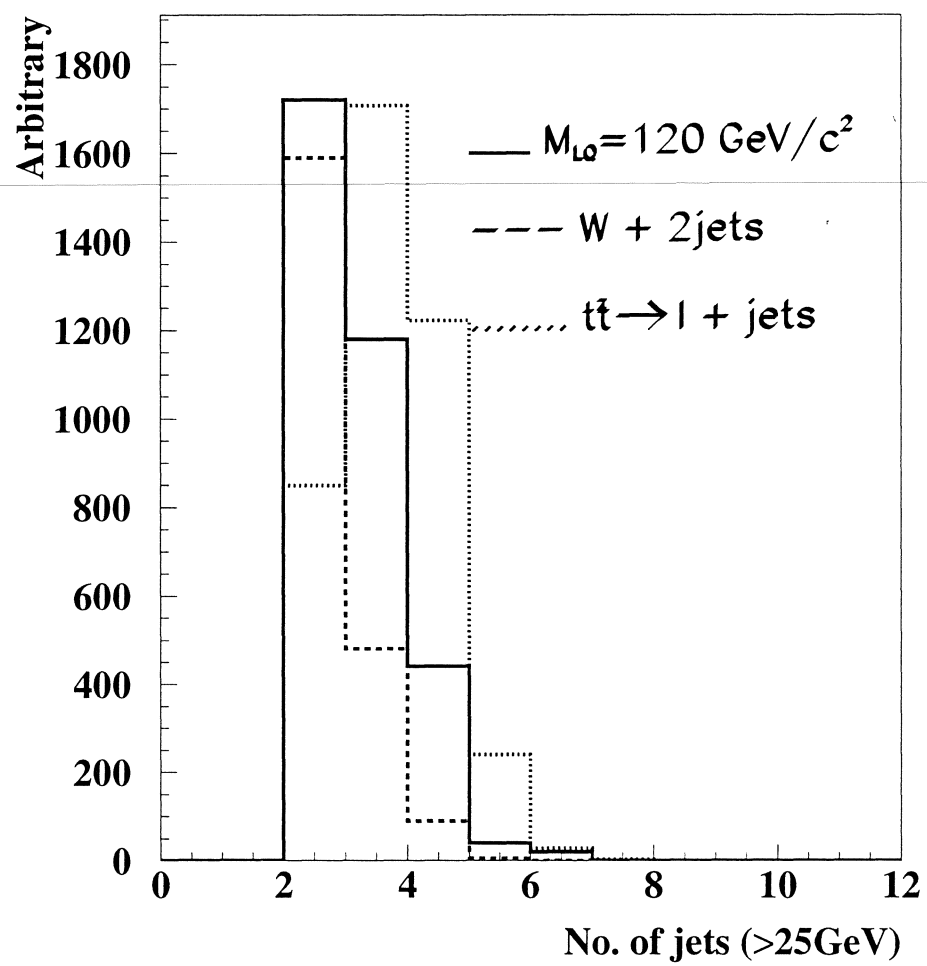

Figure 5.17: The number of jets with $E_T > 25$ GeV and $|\eta| < 2.5$. The basic offline kinematic cuts have been applied.

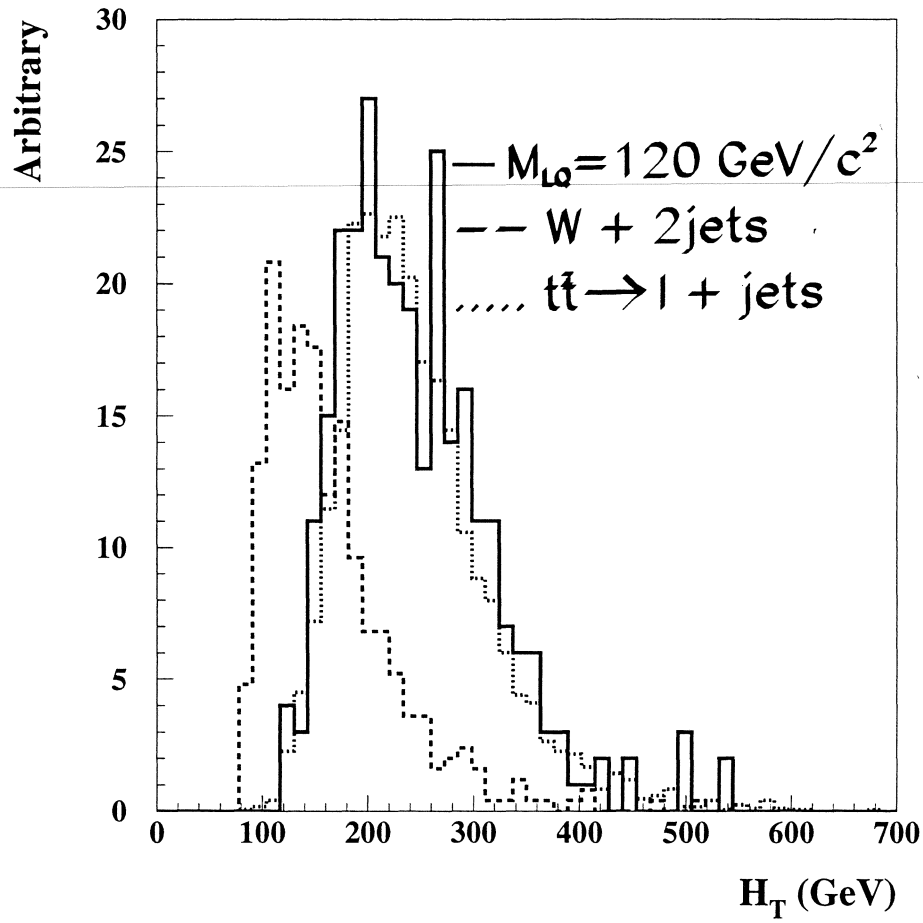

Figure 5.18: The H_T distribution after the basic offline kinematic cuts have been applied and two or three jets in $|\eta| < 2.5$ were required.

- H_T requirement:

  Figure 5.18 shows the H_T distribution after the basic offline kinematic cuts and the two or three jets requirement for the leptoquark events with leptoquark mass $M = 120$ GeV/c^2 and the backgrounds. Here H_T is defined as:

$$H_T = \sum E_T^j(> 15 \text{ GeV}) + E_T^e \tag{5.26}$$

  $H_T > 170$ GeV was required to reduce the $W + 2$ jets background. This cut has a signal efficiency of 88%–100% depending on the leptoquark mass. Also it rejects 64% of the $W + 2$ jets background and 50% of the QCD mismeasurement background.

- Muon exclusion:

  As mentioned above, the leptoquark event final states don't contain heavy flavor quarks. and so are no muons from semi-leptonic decay. Although the leptoquark event final state radiation can produce some mesons such as π^+ which decays to muon, events with muons account for only about 0.5% of the total leptoquark events. The background, however, can be reduced. Loose muons with $p_T > 4$ GeV/c were excluded. A loose muon is defined as:

  * For Run number < 89,000:

    QUADRANT ≤ 4

    IFW4 ≤ 1

    (HFrac > 0.6 AND EFracH1 > 0) OR HFrac = 1.0

    A-stubs veto

  * For run > 89,000:

    (QUADRANT ≤ 4 AND IFW4 ≤ 1) OR

    (QUADRANT ≤ 12 AND IFW4 $= 0$)

(HFrac > 0.6 AND EFracH1 > 0) OR HFrac = 1.0

A-stubs veto

"QUADRANT ≤ 4" means only CF muons ($|\eta| \leq 1.0$) are vetoed. "IFW4" is the quality-of-fit of the muon using information from the muon system only. "HFrac" and "EFracH1" are often referred to as "MTC" quantities [58] which reject combinatorial fakes and cosmic rays. MTC is a package which performs muon tracking in the calorimeter during reconstruction. There are two kind of roads in the calorimeter: 5 cell $\times$ 5 cell roads and 3 cell $\times$ 3 cell roads centered around the muon track from WAMUS projected into the calorimeter. "HFrac" is the fraction of hadronic layers which have a cell (in a 5 cell $\times$ 5 cell road) contributing to the muon track out of the total number of hadronic layers the muon track traverses. "EFracH1" is the fraction of energy in the outer most layer of the calorimeter out of the total energy within 3 cell $\times$ 3 cell road. "A-stubs veto" rejects muon tracks having no B or C layer hits.

The muon exclusion has a signal efficiency of 99.5% and rejects 20% of the QCD mismeasurement background and 10% of the top quark background.

Fig. 5.19 shows the electron and neutrino transverse mass distribution for the collider data and total background events after the basic offline cuts have been applied (one electron with $E_T > 25$ GeV, two jets with $E_T > 25$ GeV, and $\not\!\!E_T > 40$ GeV). There are 74 Run I events passing the basic cuts. The expected number of total background events is 77.91 ± 2.76 events. Fig 5.20 shows the electron and neutrino transverse mass distribution for the collider data and total background events after the above cuts have been applied. There are 32 Run I events passing the cuts. The expected number of total background events is 29.65 ± 1.64 events.

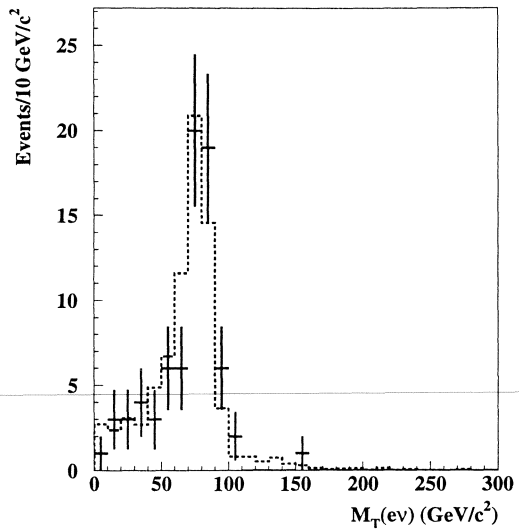

Figure 5.19: The electron and neutrino transverse mass distribution for the collider data and total background events after the basic offline cuts have been applied.

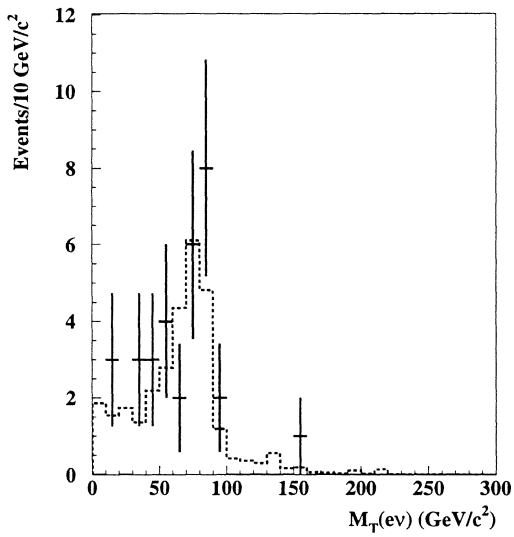

Figure 5.20: The electron and neutrino transverse mass distribution for the collider data and total background events after the offline cuts (except transverse mass and LQ mass window cuts) have been applied.

Table 5.18: Detailed information for the remaining candidate event.

Object(run 89708, event 24871)	E_T (GeV)	η	φ
Electron	61.94	0.34	1.51
Jet 1	58.92	0.17	3.74
Jet 2	54.00	0.09	0.72
Jet 3	48.00	0.87	2.13
$\not{E}_T$	92.62	–	4.89
$M_T(e\nu)$ (GeV/c^2)	150.43		
$M(ej_1)$ (GeV/c^2)	112.14		
$M(ej_2)$ (GeV/c^2)	50.76		

- Transverse mass cuts:

  Figure 5.21 shows the electron and neutrino transverse mass $M_T(e\nu)$ distribution after one electron was required to have $E_T > 10$ GeV and in the fiducial region of $|\eta| < 2.5$ for the signal and background events. Figure 5.21 shows the electron and neutrino transverse mass distribution after all the above offline cuts for the signal and background events. $M_T(e\nu) > 100$ GeV/c^2 is required to eliminate most of the $W + 2$ jets and $t\bar{t}$ backgrounds. This cut has a signal efficiency of 62%–74% depending on the leptoquark mass and rejects 98% of the $W + 2$ jets events, 75% of the top events, and 63% of the QCD mismeasurement background.

  After all the above cuts, there is one event (run 89708 event 24871) which is a top candidate. Detailed information about this event is given in Table 5.18.

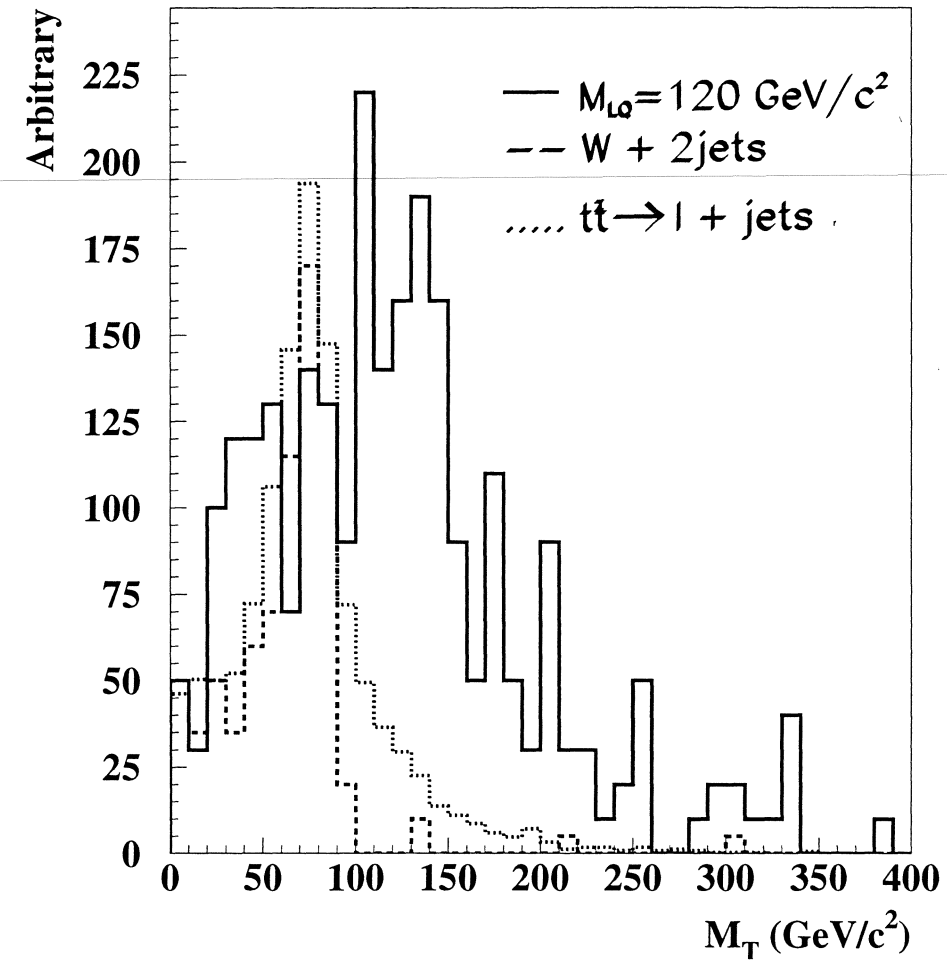

Figure 5.21: The transverse mass distribution of the electron and neutrino after the electron $E_T > 10$ GeV was required.

- LQ mass window cut:

  To make explicit use of the fact that leptoquark events in the $e\nu jj$ channel have one ej pair corresponding to the decay products of one leptoquark, naively, one would expect that, for the correct ej pair, the invariant mass M_{ej} would be equal to the actual LQ mass. In this channel, only one LQ of the pair produced in $p\overline{p}$ annihilation decays via ej, so only one mass can be properly reconstructed. The corresponding variable δM is defined as

  $$\delta M \equiv \frac{|M_{ej} - M|}{M} \tag{5.27}$$

  where M_{ej} is one of the two possible ej masses and M is the target LQ mass. There are two possible ej pairs in $e\nu jj$ events, one for each of the two jets. In this analysis, the pairing which minimizes δM was chosen.

  Figure 5.22 shows the δM distributions for signal and total background for four different LQ masses. All analysis requirements other than δM have been applied. One sees that a requirement on δM can indeed reject considerable background while maintaining high signal efficiency. Figure 5.23 shows $s^{1.15}/b^{0.35}$ for each of the four panels in Figure 5.22. A requirement of $\delta M \leq 0.2$ is optimal for a 200 GeV/c^2 leptoquark.

Table 5.19 shows the number of collider data events and expected background events after each cut. For each cut, the number of data events is consistent with that of the expected background events. After $\delta M \leq 0.2$ cut, one candidate event survives at LQ mass points 60, 100, 120, 140 GeV/c^2. To obtain the boundary of LQ masses inside which the candidate event survived, Equation 5.27 can be used. Solve the equation:

$$\delta M \equiv \frac{|M_{ej} - M|}{M} = 0.2 \tag{5.28}$$

where M_{ej} is one of the two possible ej masses and M is the hypothesized LQ mass, the boundary of LQ masses can be obtained.

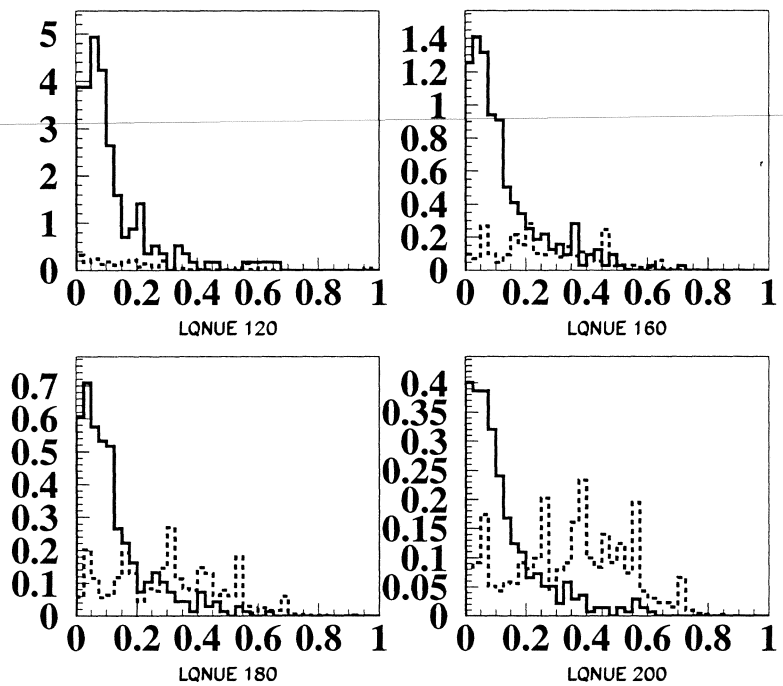

Figure 5.22: Distributions for δM for signal (solid line) and background (dashed line) for four different LQ masses. The horizontal axis is δM and the vertical axis is the number of events.

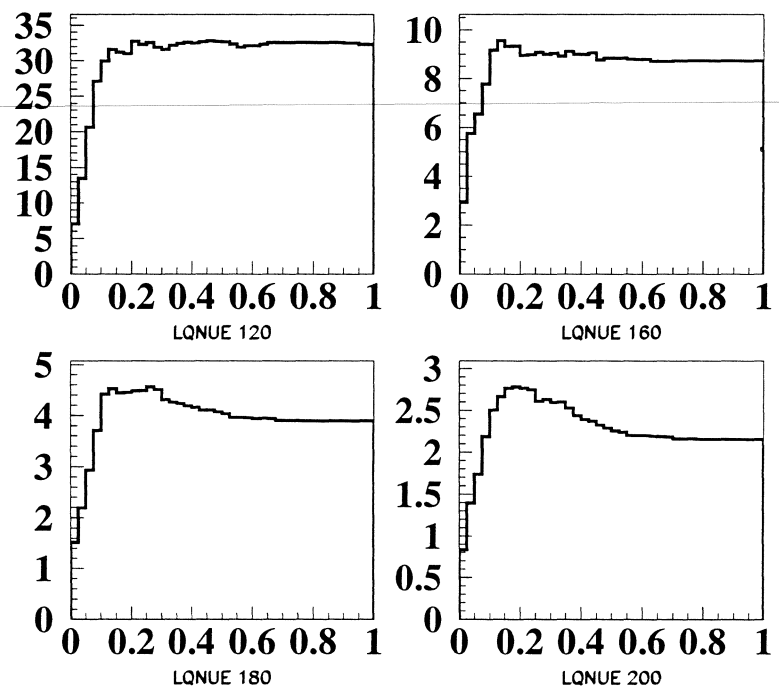

Figure 5.23: Significance distributions for the four masses shown above. The horizontal axis is δM and the vertical axis is the significance.

Table 5.19: The number of data and expected background events after each cuts. The errors in the table are statistical only.

Offline Cuts	No. of Run I Data	Expected No. of Backgrounds
1 e: $E_T > 25$ GeV 2 or more jets: $E_T > 25$ GeV $\not\!\!E_T > 40$ GeV	74	77.91 ± 2.76
2 or 3 jets: $E_T > 25$ GeV	70	67.83 ± 2.69
$H_T > 170$ GeV	33	30.92 ± 1.64
μ exclusion	32	29.65 ± 1.63
$M_T(e\nu) > 100$ GeV/c^2	1	2.48 ± 0.31

5.2.6 Background Estimation

The most important physics backgrounds are W + 2 jets events where the W boson decays into $e\nu_e$, and $t\bar{t}$ production with one of the two W bosons decaying into $e\nu_e$.

W + 2 jets. According to Reference [59], the $e\nu$ transverse mass distribution for the VECBOS generated W + 2 jets sample is narrower than that of the real data. If the jet E_T in the W + 2 jets MC sample is corrected as 1.04 E_T and the $\not\!\!E_T$ in the events is corrected accordingly, the shape of the $e\nu$ transverse mass distribution for the W + 2 jets MC sample agrees with that of the data very well. The VECBOS cross section 810.7 ± 162.1 pb was used to calculate the expected W + 2 jets background in the $e\nu$ transverse mass window 40 GeV/c^2 $< M_T(e\nu) <$ 100 GeV/c^2 and normalized the number of events inside the window to that of Run I

Table 5.20: Normalization of W + 2 jets MC events to collider data. To calculate the number of events, the following cuts were applied: one electron with $E_T^e > 25$ GeV and $|\eta_e| < 1.2$, two or more jets with $E_T^j > 25$ GeV and $|\eta_j| < 1.0$, $\not\!\!E_T > 25$ GeV, $\delta R(e,j) > 0.5$ and 40 GeV/c^2 $< M_T(e\nu) <$ 100 GeV/c^2.

Processes	Events in 103.7 ± 5.6 pb^{-1}
$t\bar{t} \to l$ + jets	16.36
$W(\to l\nu)$ + 2 jets	122.47
Mismeasurement	9.36
Run I data	112
λ_W	0.7045

data. The correction number for the VECBOS cross section is

$$\lambda_W = \frac{N_o - N_{t\bar{t}} - N_{QCD}}{N_W} = 0.7045 \tag{5.29}$$

where N_o is the number of Run I events, $N_{t\bar{t}}$ is the expected number of events from $t\bar{t}$ background, N_{QCD} is the number of events from QCD mismeasurement, and N_W is the expected number of events from the W + 2 jets background using the VECBOS cross section. Detailed information about the normalization is shown in Table 5.20. Then the W + 2 jets VECBOS cross section was scaled by λ_W to calculate the expected number of events. After the jet E_T and $\not\!\!E_T$ correction and normalization, the number of expected W + 2 jets events after the offline cuts (except the LQ mass window cut) is 0.52 ± 0.26 events corresponding to 103.7 pb^{-1} integrated luminosity.

$t\bar{t} \to l$ + jets. For the $t\bar{t}$ background, events are generated with event generator HERWIG v5.7, and with showerlibrary and trigger simulation. The top quark mass is assumed to be 170 GeV/c^2. The DØ measured $t\bar{t}$ pair production cross section 5.77 ± 1.76 pb for a top mass of 170 GeV/c^2 was used. The number of expected

$t\bar{t}$ events corresponding to 103.7 pb^{-1} integrated luminosity is 1.55 ± 0.08 events if the LQ mass window cut is not applied.

Mismeasurement background. As described in Section 5.1.6, the probability for one jet to be misidentified as an electron was first obtained. Second, the QCD sample was used again to estimate the mismeasurement background. This time, the JET_3_MON trigger was required and three jets with $E_T > 25$ GeV were required. In each event, after two jets satisfied the offline jets cuts, each remaining jet was looped and required to be in the CC region. Then the event had to satisfy all the basic offline cuts and tighter cuts. Otherwise the combination was rejected. The number of combinations times the probability of one jet to be misidentified as one electron is the mismeasurement background in 0.318 pb^{-1} of data. Finally, the mismeasurement background was scaled up to 103.7 pb^{-1} data. The mismeasurement background is 0.41 ± 0.14 events if the LQ mass window cut is not applied.

Summary. For all the background processes studied, estimates of the yields (without the LQ mass window cut) expected for an integrated luminosity of 103.7 pb^{-1} are shown in Table 5.21. The LQ mass 63, 93 and 140 GeV/c^2 are the boundary LQ masses obtained by solving Equation 5.28. The errors on the backgrounds are statistical only. Table 5.22 shows the number of background and Run I data events which pass all the cuts including the LQ mass window cut. The systematic errors come from the uncertainty of the integrated luminosity, physics background cross section uncertainties and the uncertainty in the jet energy scale. The uncertainty in the integrated luminosity is about 5.4%. The uncertainty of jet energy scale is determined using the method described in Section 4.5. The cross section uncertainty of $W + 2$ jets events is assigned as 20%. The cross section uncertainty of $t\bar{t}$ production is from Ref. [48]. The errors are shown in column two of Table 5.22.

Table 5.21: Summary of the yields of backgrounds for integrated luminosity of 103.7 pb^{-1} and the observed number of events without the δM cut. The errors on the backgrounds are statistical only.

Processes	Events expected for $103.7 \pm 5.6 pb^{-1}$
$t\bar{t} \rightarrow l$ + jets	1.55 ± 0.08
$W(\rightarrow l\nu)$ + 2 jets	0.52 ± 0.26
Mismeasurement	0.41 ± 0.14
Total	2.48 ± 0.31
Observed	1

5.2.7 Signal Efficiency

Using the method described in Section 5.1.7, the signal efficiency can be obtained. The differences are that when we calculate the kinematic acceptance for the signal MC events, we exclude the muons in the sample for $e\nu jj$ channel. For loose muons and MC events without musmearing, the multiplicative efficiency corrections are 0.851 (CF) and 0.337 (EF). For musmeared MC, the corrections are 0.937 (CF) and 0.400 (EFF). The factors include luminosity weighting for the periods without EF muons available [57]. The kinematic acceptance was calculated using the following method:

$$A(\mathrm{CC}) = \frac{N(\mathrm{CC}) - 0.851N(\mathrm{CF}) - 0.337N(\mathrm{EF})}{N_0} \tag{5.30}$$

where $A(\mathrm{CC})$ is the acceptance for the events which have a CC electron, N_0 is the total number of MC events, $N(\mathrm{CC})$ is the number of MC events passing the offline cuts, $N(\mathrm{CF})$ is the number of MC events which have CF muon and $N(\mathrm{EF})$ is the number of MC events which have an EF muon. The kinematic acceptance for the MC signal events is shown in Table 5.23.

Table 5.22: Total background resulting from the $e\nu jj$ LQ search. The column labelled "Run I Data" gives the number of events surviving in the Run I data sample after applying all selection requirements. The first, second, third and fourth errors on backgrounds are statistical, jet energy scale uncertainty (4% + 1 GeV), cross section uncertainty and luminosity uncertainty respectively.

M_{LQ} (GeV/c^2)	Total Background Events	Run I Data
60	$0.63 \pm 0.16 \pm 0.02 \pm 0.11 \pm 0.03$	1
63	$0.67 \pm 0.16 \pm 0.04 \pm 0.12 \pm 0.03$	1
63	$0.67 \pm 0.16 \pm 0.04 \pm 0.12 \pm 0.03$	0
80	$0.89 \pm 0.15 \pm 0.13 \pm 0.20 \pm 0.05$	0
93	$1.28 \pm 0.22 \pm 0.14 \pm 0.25 \pm 0.07$	0
93	$1.28 \pm 0.22 \pm 0.14 \pm 0.25 \pm 0.07$	1
100	$1.49 \pm 0.25 \pm 0.14 \pm 0.27 \pm 0.08$	1
120	$1.45 \pm 0.22 \pm 0.09 \pm 0.28 \pm 0.08$	1
140	$1.23 \pm 0.21 \pm 0.06 \pm 0.23 \pm 0.07$	1
140	$1.23 \pm 0.21 \pm 0.06 \pm 0.23 \pm 0.07$	0
160	$0.96 \pm 0.20 \pm 0.08 \pm 0.17 \pm 0.05$	0
180	$0.88 \pm 0.21 \pm 0.10 \pm 0.15 \pm 0.05$	0
200	$0.60 \pm 0.16 \pm 0.13 \pm 0.10 \pm 0.03$	0
220	$0.56 \pm 0.17 \pm 0.03 \pm 0.10 \pm 0.03$	0
240	$0.37 \pm 0.10 \pm 0.02 \pm 0.08 \pm 0.02$	0
260	$0.29 \pm 0.09 \pm 0.01 \pm 0.06 \pm 0.02$	0

The overall MC signal efficiency can be obtained by combining the trigger efficiency, one CC electron ID cut efficiency, electron tracking efficiency, and the kinematic acceptance:

$$\varepsilon_s = A(\mathrm{CC})\varepsilon_{e-\mathrm{ID}}(\mathrm{CC})\varepsilon_{trk}(\mathrm{CC})\varepsilon_{trig} \tag{5.31}$$

The efficiency of the kinematic cuts of the trigger is 100%. The L2 electron shape cut efficiency is described in Section 5.1.7 and is $(99.3\ ^{+0.7}_{-2.3})\%$. The CC electron ID cut efficiency and electron tracking efficiency are also described in Section 5.1.7.

The total signal efficiency is shown in Table 5.23. The errors on acceptance and total efficiency are statistical only. To calculate the lower band of the signal efficiency, the lower band of the jet energy scale 4.5 was used to calculate the jet energy. First, the jet E_Ts were replaced by $E_T - 4\% \cdot E_T - 1$ GeV. Then $\not\!\!E_T$ of the event was recalculated according to the E_T of the objects in this event. Based on the new E_Ts, the signal efficiency lower band is calculated. To calculate the upper band of the signal efficiency, the upper band of the jet energy scale was used to calculate the jet energy. First, the jet E_Ts were replaced by $E_T + 4\% \cdot E_T + 1$ GeV. Then $\not\!\!E_T$ of the event was recalculated according to the E_T of the objects in this event. Based on the new E_Ts, the signal efficiency upper band is calculated. The efficiencies of masses 63, 68, 86, 93 and 186 GeV/c^2 are from a linear interpolation using the efficiencies of the two nearest LQ mass.

5.2.8 Results

The number of candidate events is in agreement with the expected number of background events from SM. The 95% CL cross section limits can then be obtained from this channel. Figure 5.24 shows the leptoquark cross section upper limits at the 95% CL assuming that branching fraction of leptoquark decaying into electron and quark is 0.5. There is a step at $M_{LQ} = 140$ GeV/c^2 because there is a candidate event if $M_{LQ} \leq 140$ GeV/c^2. The theoretical cross sections are obtained by using

Table 5.23: The signal acceptance and total efficiency from the $e\nu jj$ LQ search. The errors on acceptance and total efficiency are statistical only. Detailed information is given in the text.

M_{LQ}	Acceptance	Total Signal Efficiency %		
(GeV/c^2)		Mean	Lower band	Upper band
60	0.20 ± 0.10	0.15 ± 0.08	0.00	0.15
63	-	0.24 ± 0.09	0.06	0.26
68	-	0.38 ± 0.12	0.17	0.44
80	0.95 ± 0.22	0.73 ± 0.17	0.42	0.88
86	-	1.35 ± 0.22	1.03	1.51
93	-	2.07 ± 0.28	1.73	2.25
100	3.65 ± 0.43	2.79 ± 0.34	2.44	2.98
120	6.45 ± 0.57	4.91 ± 0.46	3.95	5.40
140	9.15 ± 0.68	6.98 ± 0.56	5.88	7.40
160	11.30 ± 0.75	8.63 ± 0.64	7.75	9.05
180	12.15 ± 0.78	9.24 ± 0.66	8.59	9.24
186	-	9.81 ± 0.68	9.19	9.83
200	14.65 ± 0.86	11.13 ± 0.74	10.60	11.21
220	16.30 ± 0.57	12.37 ± 0.59	11.87	12.39
240	15.40 ± 0.55	11.70 ± 0.77	11.32	11.84
260	16.62 ± 0.58	12.69 ± 0.81	12.38	12.77

CTEQ4M (with five flavors and $\Lambda_{QCD} = 202$ MeV) parton distribution functions (pdf) [23] at different renormalization scales for $\beta = 0.5$. From the $e\nu jj$ channel, the translated mass limit for $\beta = 0.5$ is 158 GeV/c^2 if the lower theoretical cross section band (corresponding to $\mu = 2M_{LQ}$) is used.

5.3 The Combined Result from the $eejj$ and $e\nu jj$ Channels

Because the $eejj$ and $e\nu jj$ searches are independent, the result of these two channels can be combined to improve the leptoquark mass limits. Reference [60] describes an independent search for the scalar leptoquarks in the $\nu\nu jj$ channel using 7.4 pb^{-1} data. The 95% CL cross section upper limits is shown in Fig **??**. For $\beta = 0.0$, leptoquarks with mass less than 79 GeV/c^2 was excluded. Although the data set for $\nu\nu jj$ search is small, a certain area of the small β region will be excluded if all three channels are combined.

5.3.1 The 95% Cross Section Upper Limit Calculation

The basic idea of how to calculate the 95% CL cross section upper limit is described in detail in Section 5.1.8 for a single channel. Since the searches in the three channels are independent of each other, the same method can be used here.

$$\begin{aligned} P(k|\mu, I) &= P(k_{ee}, k_{e\nu}, k_{\nu\nu}|\mu_{ee}, \mu_{e\nu}, \mu_{\nu\nu}, I) \\ &= P(k_{ee}|\mu_{ee}, I)P(k_{e\nu}|\mu_{e\nu}, I)P(k_{\nu\nu}|\mu_{\nu\nu}, I) \end{aligned} \tag{5.32}$$

where $P(k|\mu, I)$ is the probability of observing k events, given the expected number of events μ and prior conditions I. Here k is the total number of candidate events in all three channels and μ is the total number of expected events in all three channels. k_{ee}, $k_{e\nu}$ and $k_{\nu\nu}$ are the numbers of candidate events in the $eejj$, $e\nu jj$ and $\nu\nu jj$ channels respectively. μ_{ee}, $\mu_{e\nu}$ and $\mu_{\nu\nu}$ are the number of expected events in the $eejj$, $e\nu jj$ and $\nu\nu jj$ channels respectively.

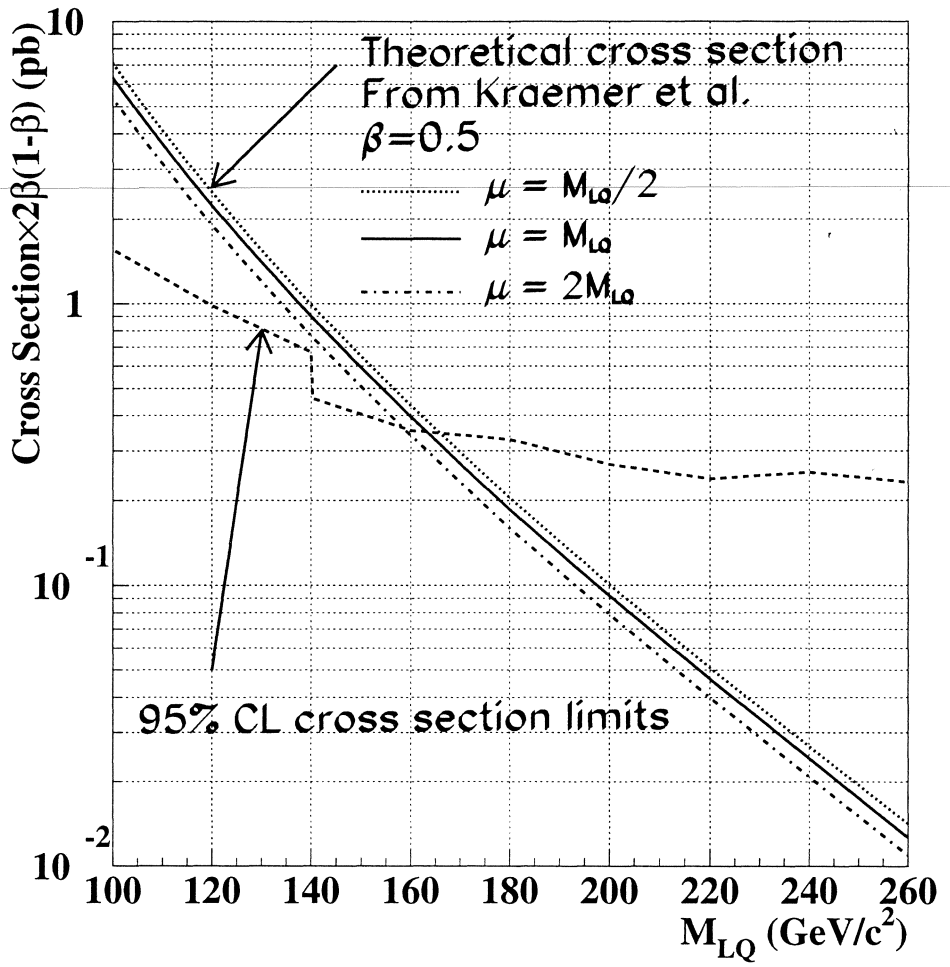

Figure 5.24: The 95% CL cross section upper limit from the $e\nu jj$ channel. Detailed information is given in the text.

μ_{ee}, $\mu_{e\nu}$ and $\mu_{\nu\nu}$ can be calculated as:

$$\begin{aligned}
\mu_{ee} &= \sigma_{ee} L_{ee} \epsilon_{ee} + b_{ee} \\
&= (L_{ee}\epsilon_{ee}\beta^2)\sigma + b_{ee} && (5.33) \\
\mu_{e\nu} &= \sigma_{e\nu} L_{e\nu} \epsilon_{e\nu} + b_{e\nu} \\
&= (L_{e\nu}\epsilon_{e\nu} \cdot 2\beta(1-\beta))\sigma + b_{e\nu} && (5.34) \\
\mu_{\nu\nu} &= \sigma_{\nu\nu} L_{\nu\nu} \epsilon_{\nu\nu} + b_{\nu\nu} \\
&= (L_{\nu\nu}\epsilon_{\nu\nu}(1-\beta)^2)\sigma + b_{\nu\nu} && (5.35)
\end{aligned}$$

where σ_x, L_x, ϵ_x and b_x are the cross section, integrated luminosity, total signal efficiency, and total background for the channel x. σ is the total cross section for leptoquark pair production. β is the branching fraction for a leptoquark to decay into an electron and a quark.

Then the same strategy is used (described in Section 5.1.8) to perform the Monte Carlo integration to solve the integrals and take into account correlations between the errors of different channels.

5.3.2 Results

The result is shown in Fig. 5.26. For the 95% CL cross section limits at $\beta = 1.0$, it is the same as that of Fig 5.12. For $\beta = 1.0$, the $e\nu jj$ and $\nu\nu jj$ channels have no contribution to the cross section limits. There is a step if $M_{LQ} \leq 86$ GeV/c^2 because one candidate event is observed. The explanation of the bump between $M_{LQ} = 160$ and 186 GeV/c^2 is due to one event in the eejj channel.

The 95% CL cross section limits at $\beta = 0.5$ in Fig. 5.26 is different from that in Fig 5.24. In Fig 5.24, only the $e\nu jj$ channel contribute to the cross section limits. In Figure 5.26, the $eejj$, $e\nu jj$ and $\nu\nu jj$ channels contribute to the 95% CL cross section limits although the $\nu\nu jj$ channel contributes little because of the much smaller luminosity. The bump between $M_{LQ} = 160$ and 186 GeV/c^2 is due to the

fact that one candidate event is observed in the $eejj$ channel. The bump between $M_{LQ} = 96$ and 140 GeV/c^2 is due to the fact that one candidate event is observed in the $e\nu jj$ channel inside the mass window. The bump between $M_{LQ} = 80$ and 83 GeV/c^2 is due to the fact that one candidate event is observed in the $eejj$ channel inside the mass window.

Comparing the 95% CL cross section limits at $\beta = 1.0$ (0.5) with the lower bond of the theoretical cross section, leptoquarks with mass less than 204 (168) GeV/c^2 corresponding to $\beta = 1.0$ (0.5) are excluded.

5.4 Summary

This analysis searched for first generation scalar leptoquark pair production at the Fermilab Tevatron in the $eejj$ and $e\nu jj$ channels. No excess in the data was seen in any channel. The 95% CL cross section upper limits were calculated by combining the three channel null search results. These 95% confidence cross section upper limits are independent of any particular model about the pair production of scalar leptoquarks since the gluon-leptoquark interactions are determined by the non-abelian $SU(3)_c$ gauge symmetry of scalar QCD. Scalar QCD implies that scalar leptoquark pair production at the Tevatron is parameter-free.

Comparing the 95% confidence cross section upper limits with the lower band of the next-to-leading order theoretical calculation ($\mu = 2M_{LQ}$), the 95% CL mass limits on leptoquarks can be obtained. The leptoquark mass limit vs. branching fraction β is shown in Figure 5.27. The contour is not smooth because one candidate event is observed in the $eejj$ search in the leptoquark mass windows $160 \leq M_{LQ} \leq 186$ GeV/c^2 and one candidate event is observed in the $e\nu jj$ search in the leptoquark mass windows $93 \leq M_{LQ} \leq 140$ GeV/c^2. The result is that in these two leptoquark mass windows, the branching fraction (for a leptoquark decaying into an electron and a quark) β is larger for the same leptoquark mass limit than that with no

candidate events observed. It also indicate that for the same β (corresponding to the above mass windows) the leptoquark mass limits are lower that that with no candidate events observed.

If we assume that the branching fraction for a leptoquark to decay into an electron and a quark β is 1.0, scalar leptoquarks with mass less than 204 GeV/c^2 are excluded. If $\beta = 0.5$, scalar leptoquarks with mass less than 168 GeV/c^2 are excluded.

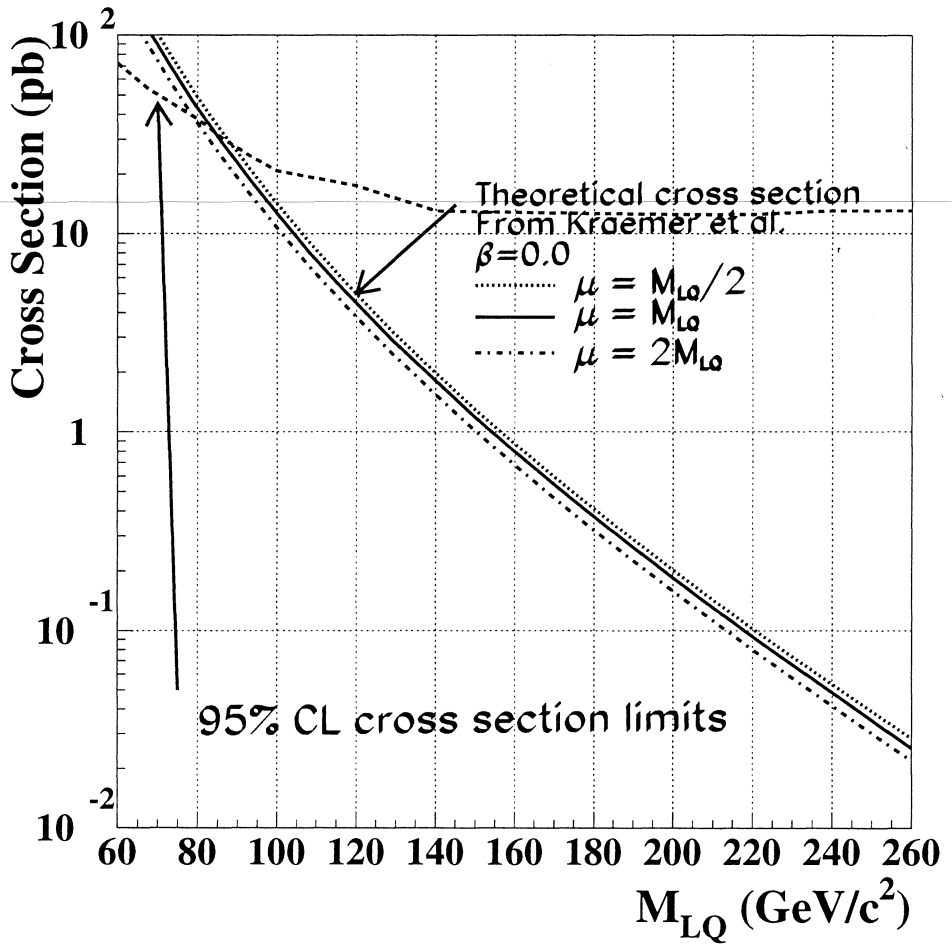

Figure 5.25: The 95% CL cross section limits from the independent Run Ia $\nu\nu jj$ search.

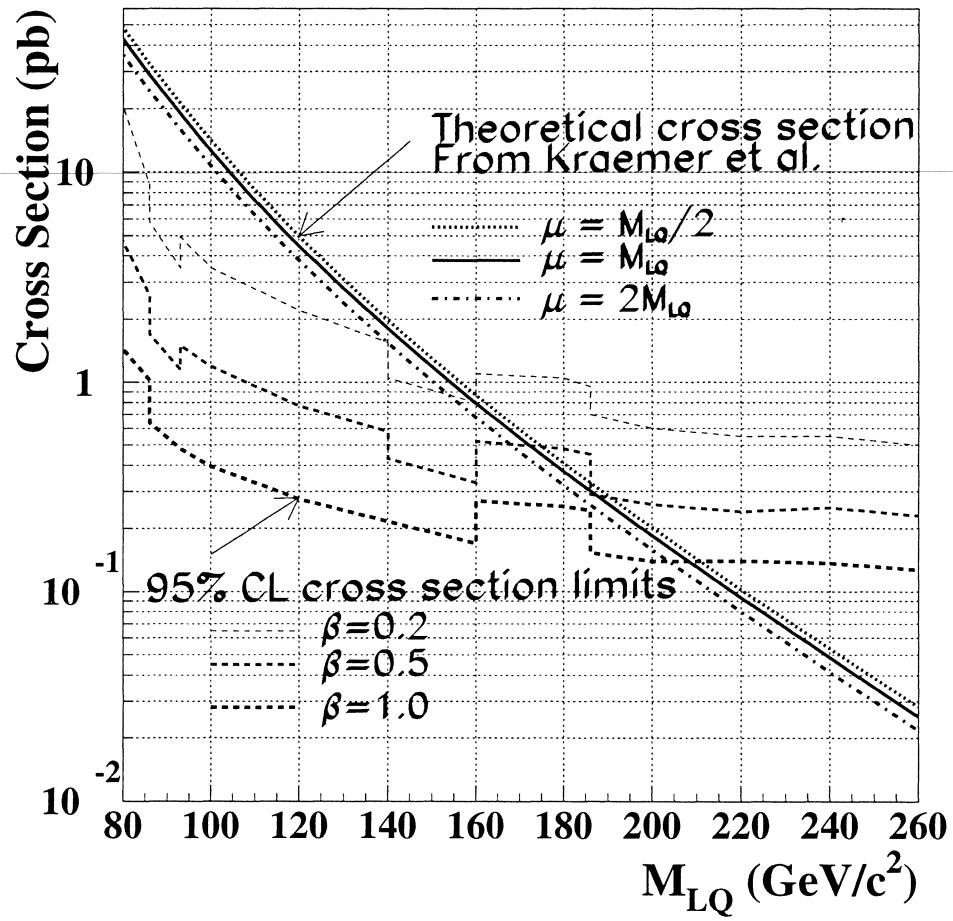

Figure 5.26: The 95% CL cross section limits from the combination. Detailed information is given in the text.

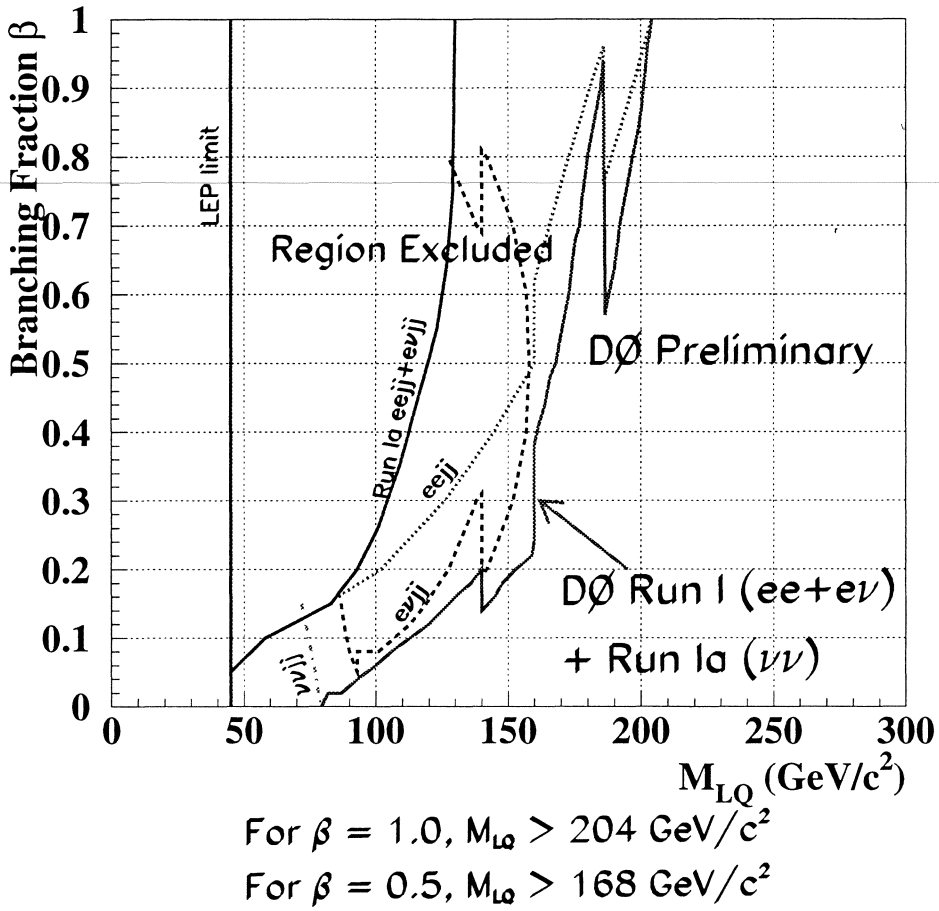

Figure 5.27: Excluded contour of scalar leptoquark branching fraction β vs. mass from the combination. More detailed information is given in the text.

CHAPTER 6

CONCLUSIONS

This dissertation has described a search for first generation scalar leptoquarks at the Tevatron in the $eejj$ and $e\nu jj$ channels. The search is based on the assumption that (i) there are three distinct leptoquarks, one for each generation; (ii) each leptoquark can only couple to the corresponding generation's leptons and quarks; (iii) the scalar leptoquarks have fractional charges $-\frac{1}{3}$ or $+\frac{2}{3}$. No data excess is found in either channels. The 95% CL cross section upper limits are calculated using Bayesian Statistics. The cross section upper limits are translated into leptoquark mass limits by comparing the 95% CL cross section upper limits with the next-to-leading order theoretical cross section. The contour β verse leptoquark mass limit is obtained. Leptoquarks with mass less than 204 (168) GeV/c^2 corresponding to $\beta = 1.0$ (0.5) are excluded. These results are based on the cuts optimized at $M_{LQ} = 160/120$ GeV/c^2 for $eejj/e\nu jj$ channel. If the offline cuts for each mass point are optimized separately and the corresponding signal efficiency is calculated, the leptoquark mass limit will be higher than the above results. This requires a lot of effort and computer cpu time.

If the search for leptoquarks in the $\nu\nu jj$ channel is finished using the full Run I data sample, much of the low β region (β around 0) can be constrained.

Searches for second and third generation leptoquarks based on the same assumptions described above are in progress at DØ. All of these searches will improve our understanding of the lepton and quark sector.

After the DØ upgrade and Main Ring Injector project at Fermilab are finished in the near future, searches for first generation leptoquarks could be much improved

since the luminosity will be much larger and the electron identification efficiency will be improved with the introduction of a central magnetic field in the DØ upgrade. If the signal efficiency is assumed to be the same as for this search, with a luminosity of 2 fb^{-1} for Run II, first generation scalar leptoquarks can be probed up to about 330 GeV/c^2.

BIBLIOGRAPHY

[1] For text book reviews of the SM, see *e.g.* F. Halzen and A. D. Martin, *Quarks and Leptons*, John Wiley (1984); D. H. Perkins, *Introduction to High Energy Physics*, Addison Wesley (1987).

[2] For a review, see G. Ross, *Grand Unified Theories*, Benjamin-Cummings Publishing Co. (1995); P. D. B. Collins, A. D. Martin and E. J. Squires, *Particle Physics and Cosmology*, John Wiley (1989).

[3] X. Tata, "An Introduction to Supersymmetry and Supersymmetry Phenomenology," UH-511-713-90 (unpublished).

[4] H. P. Nilles, Phys. Rep. **110**, 1 (1984).

[5] L. F. Abbott and E. Farhi, Phys. Lett. **B101**, 69 (1981).

[6] L. F. Abbott and E. Farhi, Nucl. Phys. **B189**, 547 (1981).

[7] J. C. Pati and A. Salam, Phys. Rev. D **10**, 275 (1974).

[8] H. S. Kambara, CDF Collaboration, FERMILAB-CONF-97/225-E. To be published Proceedings Hadron Collider Physics XII, State University of New York at Stony Brook, Stony Brook, NY, June 5–11, 1997.

[9] E. Eichten *et al.*, Phys. Rev. D **34**, 1547 (1986).

[10] W. Buchmüller and D. Wyler, Phys. Lett. **B177**, 377 (1986).

[11] E. Witten, Nucl. Phys. **B258** 75 (1985).

[12] J. L. Hewett and S. Pakvasa, Phys. Rev. D **37**, 3165 (1988).

[13] J. L. Hewett and T. G. Rizzo, Phys. Rev. D **36**, 3367 (1987).

[14] S. Dawson, E. Eichten and C. Quigg, Phys. Rev. D **31**, 1581 (1985).

[15] P. R. Harrison and C. H. Llewellyn Smith, Nucl. Phys. **B213**, 223 (1983) and Errata **B223**, 542 (1983).

[16] J. Blümlein, E. Boos and A. Kryukov, Z. Phys. **C76**, 137 (1997).

[17] V. Barger and R. J. N. Phillips, *Collider Physics*, Addison-Wesley (1987).

[18] H. L. Lai *et al.*, Phys. Rev. D **51**, 4763 (1995).

[19] A. D. Martin, R. G. Roberts and W. J. Stirling, Phys. Lett. **B356**, 4756 (1995).

[20] P. N. Harriman, A. D. Martin, R. G. Roberts and W. J. Stirling, Phys. Rev. D **42**, 798 (1990) and Phys. Lett. **B243**, 421 (1995).

[21] H. Plothow-Besch, Comput. Phy. Commun. **75**, 396 (1993); H. Plothow-Besch, Int. J. Mod. Phys. **A10**, 2901 (1995).

[22] H. L. Lai *et al.*, Phys. Rev. D **55**, 1280 (1997).

[23] M. Krämer, T. Plehn, M. Spira, and P. M. Zerwas, Phys. Rev. Lett., **79**, 341 (1997).

[24] H. Zhang for the Zeus Collaboration, to be published in Proceedings of DPF96, Minneapolis, Minnesota; H1 Collaboration, S. Aid *et al.*, Phys. Lett. **B369**, 173 (1995).

[25] L3 Collaboration, B. Adeva *et al.*, Phys. Lett. **B261**, 169 (1991); OPAL Collaboration, G. Alexander *et al.*, Phys. Lett. **B263**, 123 (1991); DELPHI Collaboration, P. Abreu *et al.*; Phys. Lett. **B316**, 620 (1992); ALEPH Collaboration, Phys. Rep. C **216**, 253 (1992).

[26] CDF Collaboration, F. Abe *et al.*, Phys. Rev. D **48**, 3939 (1993).

[27] DØ Collaboration, S. Abachi *et al.*, Phys. Rev. Lett. **72**, 965 (1994).

[28] D. Möhl, G. Petrucci, L. Thorndahl and S. van der Meer, Phys. Rep. C **73** (1980).

[29] DØ Collaboration, S. Abachi *et al.*, Nucl. Inst. and Meth. A **338**, 185 (1994).

[30] M. Abolins *et al.*, Nucl. Instr. and Meth. A **280**, 36 (1989).

[31] S. Abachi *et al.*, Nucl. Instr. and Meth. A **324**, 53 (1993).

[32] S. Abachi *et al.*, Nucl. Instr. and Meth., A **325**, 393 (1993).

[33] J. A. Guida, Proceedings of the 4th International Conference on Advanced Technology and Particle Physics, Como, Italy, Oct. 3-7, 1994, Nucl. Phys. **B44** (Proc. Suppl.), 158 (1995).

[34] R. Kehoe, Proceedings of the 6th International Conference on Calorimetry in High Energy Physics, Frascati, Italy, June 8-14, 1996, SIS – Ufficio Pubblicazioni, frascati physics series, volume VI, 349 (1996).

[35] M. Abolins *et al.*, IEEE Trans. Nucl. Sci. **36**(1), 384 (1989).

[36] M. Fortner *et al.*, IEEE Trans. Nucl. Sci. **38**(2), 480 (1991).

[37] U. Heintz and M. Narain, DØ Note 2355 (unpublished).

[38] U. Heintz and M. Narain, DØ Note 2386 (unpublished).

[39] I. Adam, DØ Note 2553 (unpublished).

[40] DØ Collaboration, S. Abachi *et al.*, Phys. Rev. D **52**, 4877 (1995).

[41] DØ CAFIX, D0 NOTE 3287 (unpublished).

[42] ALEPH Collaboration, Buskulik *et al.*, Z. Phys. **62**, 539 (1994); DELPHI Collaboration, Abreu *et al.*, Nucl. Phys. **B418**, 403 (1994); L3 Collaboration, Acciari *et al.*, Z. Phys. C **62**, 551 (1994); OPAL Collaboration, Akers *et al.*, Z. Phys. C **61**, 19 (1994).

[43] F. Hseih, R. Patridge, and S. Snyder, "Jet Energy Scale Uncertainty for Top Cross Section PRL," DØ internal note, in preparation.

[44] CDF Collaboration, F. Abe *et al.*, Phys. Rev. Lett. **69**, 2898 (1992).

[45] F. Paige and S. Protopopescu, BNL Report No. BNL38034, 1986 (unpublished).

[46] G. Manning *et al.*, "DØ Software Documentation," DØ internal note, in preparation. (URL: **http://www-d0.fnal.gov/software/offline_document.ps**)

[47] J. Bantly, D. Owen and R. Partridge, "DØ Luminosity Monitor Constant for the 1994–1996 Tevatron Run," DØ Note 3199 (unpublished).

[48] DØ Collaboration, S. Abachi *et al.*, "Measurement of the Top Quark Pair Production Cross Section in $p\bar{p}$ Collisions," Phys. Rev. Lett. 79, 1203 (1997).

[49] DØ Collaboration, S. Abachi *et al.*, "Direct Measurement of the Top Quark Mass," Phys. Rev. Lett. 79, 1197 (1997); DØ Collaboration, B. Abbott *et al.*, "Measurement of the Top Quark Mass Using Dilepton Events," hep-ex/9706014, submitted to Physical Review Letters.

[50] DØ Collaboration, S. Abachi *et al.*, "Measurement of the Transverse Momentum Distribution of W and Z Bosons Produced in $p\bar{p}$ Collisions at $\sqrt{s} = 1.8$ TeV," to be published.

[51] DØ Collaboration, S. Abachi *et al.*, "W and Z Bosons Production in $p\bar{p}$ Collision at $\sqrt{s} = 1.8$ TeV," Phys. Rev. Lett. **75**, 1456 (1995).

[52] J. Ohnemus, "Order-α_s calculation of hadronic W^-W^+ production," Phys. Rev. D **44**, 1403 (1991).

[53] U. Heintz and M. Narain, "A Study of Electron ID Efficiencies Using $Z \to ee$ Decays," DØ Note 1814 (unpublished).

[54] John Hobbs, private communication.

[55] I. Bertram, *et al*, "A Recipe for the Construction of Confidence Limits," DØ Note 2775A, (unpublished).

[56] Marc Paterno, private communication.

[57] J. Hobbs, private communication.

[58] E. Gallas, "The MTC Package (Muon Tracking in the DØ Calorimeter)," DØ Note 2066 (unpublished).

[59] K. Genser *et al*, "$e\nu$ Top Analysis at DØ," DØ Note 3067 (unpublished).

[60] D. Claes and E. Flattum, "Search for Leptoquarks in $\nu\nu jj$ Channel," DØ internal note, in preparation.

BIOGRAPHICAL SKETCH

Date of Birth	May 4, 1966
Marital Status	Married to Dan Xiao since 1991.
Education	1994-1997 Florida State University, Tallahassee, Florida, USA Ph.D., Physics
	1992-1994 Florida State University, Tallahassee, Florida, USA M.Sc., Physics
	1984-1989 Tsinghua (Qinghua) University, Beijing, China B.Engr., Electrical Engineering
	1981-1984 The 1st Middle School of Xichang, Sichuan, China
	1979-1981 The 3rd Middle School of Xichang, Sichuan, China
	1973-1979 Guihua Elementary School, Guangan, Sichuan, China
Research and Teaching Positions	1994-1997 Research Assistant in Particle Physics, Florida State University, Tallahassee, Florida, USA
	1992-1994 Teaching Assistant in Physics, Florida State University, Tallahassee, Florida, USA

PUBLICATIONS (AS AN AUTHOR OR CO-AUTHOR)

1. "Study of Radiation Damage of Tile/Fiber Scintillator Calorimeter," High Energy Phys. and Nucl. Phys., Vol. 16, No. 10, 876 (1992).

2. "Radiation Damage of Tile/Fiber Scintillator Modules for the SDC Calorimeter," Radiat. Phys. and Chem., Vol. 41, No. 1/2, 273 (1993).

3. "Transverse Energy Distributions within Jets in $p\bar{p}$ Collisions at 1.8 TeV," Phys. Lett. **B357** 500 (1995).

4. "A Study of the Strong Coupling Constant Using W - Jets Processes," Phys. Rev. Lett. **75** 3226 (1995).

5. "Second Generation Leptoquark Search in $p\bar{p}$ Collisions at 1.8 TeV," Phys. Rev. Lett. **75** 3618 (1995).

6. "Studies of Topological Distributions of Inclusive Three- and Four- Jet Events in $p\bar{p}$ Collisions at $\sqrt{s}$ = 1800 GeV with the DØ Detector," Phys. Rev. D **53**, 6000 (1996).

7. "Search for $\tilde{W}_1\tilde{Z}_2$ via Trilepton Final States in $p\bar{p}$ Collisions at $\sqrt{s}$ = 1.8 TeV," Phys. Rev. Lett. **76**, 2228 (1996).

8. "The Azimuthal Decorrelation of Jets Widely Separated in Rapidity," Phys. Rev. Lett. **77**, 595 (1996).

9. "Jet Production via Strongly-Interacting Color-Singlet Exchange in $p\bar{p}$ Collisions," Phys. Rev. Lett. **76**, 734 (1996).

10. "Search for Right-Handed W Bosons and Heavy W' in $p\bar{p}$ Collisions at $\sqrt{s}$ = 1.8 TeV," Phys. Rev. Lett. **76**, 3271 (1996).

11. "Search for Heavy W Bosons in 1.8 TeV $p\bar{p}$ Collisions," Phys. Lett. **B358**, 405 (1995).

12. "Search for Anomalous WW and WZ Production in $p\bar{p}$ Collisions at $\sqrt{s}$ =1.8 TeV," Phys. Rev. Lett. **77**, 3303 (1996).

13. "J/ψ Production in $p\bar{p}$ Collisions at $\sqrt{s} = 1.8$ TeV," Physics Lett. **B370**, 239 (1996).

14. "Search for Light Top Squarks in $p\bar{p}$ Collisions at 1.8 TeV," Phys. Rev. Lett. **76**, 2222 (1996).

15. "Measurement of the W Boson Mass," Phys. Rev. Lett. **77**, 3309 (1996).

16. "Search for Additional Neutral Gauge Bosons," Phys. Lett. **B385**, 471 (1996).

17. "The Isolated Photon Cross Section in the Central and Forward Rapidity Region in $p\bar{p}$ Collisions at $\sqrt{s} = 1.8$ TeV," Phys. Rev. Lett. **77**, 5011 (1996).

18. "Search for a Fourth Generation -1/3 Quark via Flavor Changing Neutral Current Decay," Phys. Rev. Lett. **78**, 3818 (1997).

19. "Search for Diphoton Events with Large Missing Transverse Energy in $p\bar{p}$ Collisions at $\sqrt{s} = 1.8$ TeV," Phys. Rev. Lett. **78**, 2070 (1997).

20. "Limits on Anomalous $WW\gamma$ Couplings from $p\bar{p} \rightarrow W\gamma + X$ Events at $\sqrt{s} =$ 1.8 TeV," Phys. Rev. Lett. **78**, 3634 (1997).

21. "Study of the ZZg and Zgg Couplings in $Z(\nu\nu)g$ Production," Phys. Rev. Lett. **78**, 3640 (1997).

22. "Direct Measurement of the Top Quark Mass," Phys. Rev. Lett. **79**, 1197 (1997).

23. "Measurement of the Top Quark Pair Production Cross Section in $p\bar{p}$ Collisions," Phys. Rev. Lett. **79**, 1203 (1997).

24. "Limits on WWZ and $WW\gamma$ couplings from $p\bar{p} \rightarrow e\nu jjX$ events at $\sqrt{s} = 1.8$ TeV," Phys. Rev. Lett. **79**, 1441 (1997).

25. "Search for Top Squark Pair Production in the Dielectron Channel," Accepted by Phys. Rev. D as a Brief Report, FERMILAB-PUB-96/449-E, hep-ex/9612009.

26. "Studies of Gauge Boson Pair Production and Trilinear Couplings," Accepted by Phys. Rev. D, Fermilab-Pub-97/088-E, hep-ex/9704004.

27. "Color Coherent Radiation in Multijet Events from $p\bar{p}$ Collisions at $\sqrt{s}$ = 1.8 TeV," Accepted by Phys. Lett. B, FERMILAB PUB-97/201-E, hep-ex/9706012.

28. "Search for Scalar Leptoquark Pairs Decaying to Electrons and Jets in $p\bar{p}$ Collisions," Accepted by Phys. Lett., FERMILAB PUB-97/252-E, hep-ex/9707033.

29. "Experimental Search for Chargino and Neutralino Production in Supersymmetry Models with a Light Gravitino," Accepted by Phys. Rev. Lett., FERMILAB PUB-97/273-E, hep-ex/9708005.

30. "Search for the Trilepton Signature from the Associated Production of SUSY $\tilde{\chi}_1^{\pm}\tilde{\chi}_2^0$ Gauginos," Submitted to Phys. Rev. Lett., FERMILAB PUB-97/153-E, hep-ex/9705015.

31. "Measurement of the Top Quark Mass Using Dilepton Events," Submitted to Phys. Rev. Lett., FERMILAB PUB-97/172-E, hep-ex/9706014.

32. "Measurement of Dijet Angular Distributions and Search for Quark Compositeness," Submitted to Phys. Rev. Lett., FERMILAB PUB-97/237-E, hep-ex/9707016.

33. "Determination of the Mass of the W Boson Using the DØ Detector at the Tevatron," Submitted to Phys. Rev. D, FERMILAB PUB-97/328-E, hep-ex/9710007.

34. "$Z\gamma$ Production in $p\bar{p}$ Collisions at $\sqrt{s}$ = 1.8 TeV and Limits on Anomalous $ZZ\gamma$ and $Z\gamma\gamma$ Couplings," Submitted to Phys. Rev. Lett., FERMILAB PUB-97/363-E, hep-ex/9710031.

35. "Search for First Generation Scalar Leptoquark Pairs in $p\bar{p}$ Collisions at $\sqrt{s}$ = 1.8 TeV," Submitted to Phys. Rev. Lett., FERMILAB PUB-97/344-E, hep-ex/9710032.

36. "Search for First Generation Scalar Leptoquarks at DØ," to be published in Proceedings of the 1996 American Physical Society Division of Particles and Fields Meeting (DPF96), Minneapolis, Minnesota, USA. FERMILAB-Conf-96/389-E.

37. "Leptoquark Searches at the Tevatron," to be published in Proceedings of the 5th International Workshop on Deep Inelastic Scattering and QCD, Chicago, Illinois, USA.

TALKS AT CONFERENCES

1. "Search for First Generation Scalar Leptoquarks at DØ," parallel session talk given at the 1996 American Physical Society Division of Particles and Fields Meeting (DPF96), Minneapolis, Minnesota, Aug. 10-15, 1996.

2. "Leptoquark Searches at the Tevatron," given at the 5th International Workshop on Deep Inelastic Scattering and QCD (DIS97), Chicago, Illinois, USA, April 14-18, 1997.

3. "Search for First Generation Leptoquarks at DØ," given at the annual American Physical Society Meeting (the Joint APS/AAPT Meeting), Washington, DC, USA, April 18-21, 1997.